Plasma-deposited aluminum-doped zinc oxide : controlling nucleation, growth and electrical properties

Citation for published version (APA):
Ponomarev, M. (2012). *Plasma-deposited aluminum-doped zinc oxide : controlling nucleation, growth and electrical properties*. [Phd Thesis 1 (Research TU/e / Graduation TU/e), Applied Physics and Science Education]. Technische Universiteit Eindhoven. https://doi.org/10.6100/IR740166

DOI:
10.6100/IR740166

Document status and date:
Published: 01/01/2012

Document Version:
Publisher's PDF, also known as Version of Record (includes final page, issue and volume numbers)

Please check the document version of this publication:

• A submitted manuscript is the version of the article upon submission and before peer-review. There can be important differences between the submitted version and the official published version of record. People interested in the research are advised to contact the author for the final version of the publication, or visit the DOI to the publisher's website.
• The final author version and the galley proof are versions of the publication after peer review.
• The final published version features the final layout of the paper including the volume, issue and page numbers.

Link to publication

General rights
Copyright and moral rights for the publications made accessible in the public portal are retained by the authors and/or other copyright owners and it is a condition of accessing publications that users recognise and abide by the legal requirements associated with these rights.

- Users may download and print one copy of any publication from the public portal for the purpose of private study or research.
- You may not further distribute the material or use it for any profit-making activity or commercial gain
- You may freely distribute the URL identifying the publication in the public portal.

If the publication is distributed under the terms of Article 25fa of the Dutch Copyright Act, indicated by the "Taverne" license above, please follow below link for the End User Agreement:

www.tue.nl/taverne

Take down policy
If you believe that this document breaches copyright please contact us at:

openaccess@tue.nl

providing details and we will investigate your claim.

Download date: 05. Oct. 2023

Plasma-deposited Aluminum-doped Zinc Oxide:

Controlling nucleation, growth and electrical properties

Mikhail V. Ponomarev

Plasma-deposited Aluminum-doped Zinc Oxide:

Controlling nucleation, growth and electrical properties

PROEFSCHRIFT

ter verkrijging van de graad van doctor aan de
Technische Universiteit Eindhoven, op gezag van de
rector magnificus, prof.dr.ir. C.J. van Duijn, voor een
commissie aangewezen door het College voor
Promoties in het openbaar te verdedigen
op donderdag 13 december 2012 om 16.00 uur

door
Mikhail Victorovich Ponomarev

geboren te Sjoemicha, Sovjet-Unie

Dit proefschrift is goedgekeurd door de promotor:

prof.dr.ir. M.C.M. van de Sanden

Copromotor:
dr. M. Creatore

This research was carried out under IRTES project and was financially supported by Agenschap NL (project number 10007870).

Printed and bound by: Printservice Technische Universiteit Eindhoven.
Cover design: Anna Ponomareva.

A catalogue record is available from the Eindhoven University of Technology Library

ISBN: 978-90-386-3297-1

Contents

Chapter 1

Introduction

1.1 Topicality of photovoltaics

1.1.1 World energy consumption

The continuous increase in world population reflects in the growing consumption of goods and therefore energy for production. The German Advisory Council on Global Change demonstrated in its report prognosis [1], that the global primary energy demand will be more than doubled by 2050, from approx. 470 exajoules (EJ)[1] in 2010 to around 1,100 EJ per year. The world energy consumption is at the center of climate change debate, since associated emissions of greenhouse gases are primarily resulting from combustion of fossil fuels. With a probability of around 99 %, the emissions that would be associated with the increased energy demand would lead to overcome the 2 °C guard rail. This designates the mean temperature limit above preindustrial levels, set by the United Nations Framework Convention on Climate Change to prevent extinction of species through Earth run-away climate changes. The average surface temperature of the Earth has increased by about 0.8 °C with about 0.6 °C increase over the last three decades [2], due to the increasing concentration of greenhouse gases (major ones are: carbon dioxide-CO_2, methane-CH_4, nitrous oxide-N_2O, ozone-O_3 and water vapor) in the atmosphere as a result of human activities and usually attributed to deforestation and burning of fossil fuels.

According to the estimates of the International Energy Agency (IEA), CO_2 emissions from fossil fuel combustion reached 31.6 Gigatonnes (Gt) in 2011 and will increase to 43.2 Gt by 2035 [3]. The share of coal accounted for 45 %, oil 35 % and natural gas 20 % in the total 2011 energy-related CO_2 emissions. Projected growth in CO_2 emissions is mainly attributed to developing countries that continue to rely heavily on fossil fuels to meet the increasingly growing energy demand [3]. The emissions of these countries are projected to account for total

---

[1] 1 EJ=10^{18} J=$278{\cdot}10^{9}$ kWh

28.9 Gt in 2035, or about 67 % of global emissions. Non-CO_2 greenhouse gases, such as CH_4 and N_2O also contribute to the global warming, accounting for one-third of CO_2 equivalent [4]. Global emissions trend must be reversed by 2020 at the latest (no more than 44 Gt CO_2 equivalent per year), to reduce global greenhouse gas emissions to a minimum by 2050 and thereby to maintain the possibility of avoiding dangerous climate change.

With all the growing demand for energy and consequent use of the traditional, nonrenewable fuels it is also important to know the limitations of the natural reserves of these fuels. In 2011, the proven world oil reserves were estimated at 1,471 billion barrels. These are the reserves which are already known to exist and are economically exploitable at current prices and technology. Regarding the ultimate geological resource, the various sources show different estimates, generally, between 2-3 trillion barrels. Thus the ultimate reserves of oil will be enough only up to 2100. The global natural gas reserves in 2011 were estimated at 6,675 trillion cubic feet. Worldwide, the reserves-to production ratio of natural gas is estimated at 60.2 years. Total recoverable reserves of coal around the world are estimated at 948 billion tons—reflecting a current reserves-to-production ratio of 126 years [3].

At the same time the number of people without access to electricity up to now remained unacceptably high at 1.3 billion, around 20 % of the world's population, and 2.7 billion people still rely on the traditional use of biomass for cooking [5]. The assumptions of a global population that increases by 1.7 billion people and 3.5 % annual average growth in the global economy generate ever-higher demand for energy services and mobility. Therefore the global transition to renewable energy is already underway. Thanks to the United Nations 2002 World Summit on Sustainable Development in Johannesburg, South Africa, the importance of access to clean and renewable energy was highlighted supporting sustainable development and poverty eradication .

1.1.2 Present time share of renewable energy

The renewable energy supplied in 2009 was estimated to be 16 % of global final energy consumption [6] (see Figure 1.1). Traditional biomass, which is used primarily for cooking and heating in rural areas of developing countries, accounted for approximately 10 % of the total renewable energy share. Hydropower represented 3.4 %, growing modestly. All other renewables accounted for approximately 2.8 % in 2009 and are growing very rapidly in many developed countries as well as in

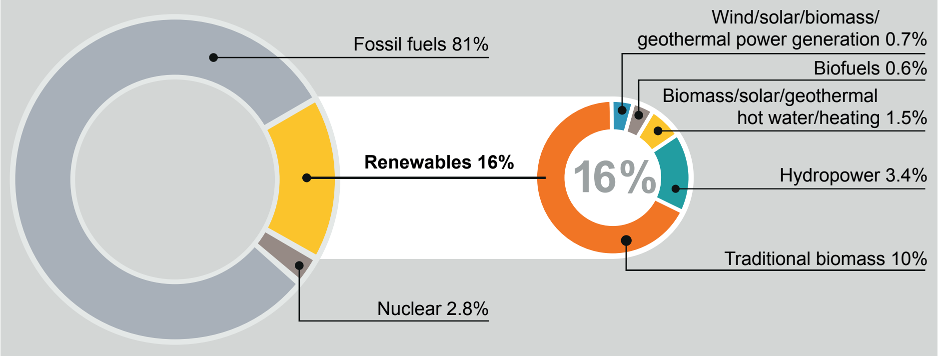

Figure 1.1. Renewable energy share in global final energy consumption, 2009 [6].

some developing countries.

During the period from the end of 2005 through 2010 the total global capacity of solar photovoltaics (PV) increased the fastest (nearly 50 % annually) amongst all renewable technologies during this period, followed by biodiesel and wind [6]. One of the drivers to cause that growth is a PV module price reduction, leading to a low electricity price of ∼0.1 Euro/kWh in EU countries, which is matching the utility electricity prices (so-called grid parity) [7]. Moreover, that strong growth of PV is also caused by the advantages of solar-generated electricity:

- Inexhaustible and free energy directly from the Sun ($3.8{\cdot}10^6$ EJ/year), more than enough to cover all human needs: amount of energy received in about an hour covers present world energy consumption during 1 year (energy demand in 2010 was 470 EJ and prognosis is 1100 EJ in 2050) and in 20 minutes the annual electricity consumption in 2010;

- Safety and reliability are proven. For example, PV modules based on crystalline silicon and cadmium telluride have output warranty of at least 25 years, which becomes a common standard. Systems can be recycled at the end of their life and the materials can be re-used. For example, First Solar (www.firstsolar.com) claims to reuse about 95 % of semiconductor materials of the old modules for production of the new ones;

- Easy installation, automatic operation (noise-, and pollutions-free) and very low maintenance requirements;

- The energy used for manufacturing can be recouped quickly (between six months and three years, often called energy payback-time) and that timeframe is constantly decreasing as technology improves with the shortest times for organic-based PV and cadmium telluride technologies [8];

- Energy generation in line with demand: small-scale installations in remote areas that are not connected to the grid; roof-top or building-integrated PV devices supplying energy to a growing community thus also saving space for installation.

1.1.3 Basic principle of PV

PV is a method to convert solar radiation into DC electricity by means of the photovoltaic effect in semiconductor absorber materials and PV devices are commonly known as solar cells (SCs). The general principle is shown in Figure 1.2.

The PV conversion starts with absorption of incident solar radiation in the absorber (active) layer of the SC. Most common absorber materials are: amorphous, micro-, poly- and monocrystalline silicon; cadmium telluride; copper-indium-gallium selenide; ruthenium dye and semiconductor polymers. Each of them has its own advantages and drawbacks, but the general challenge is to achieve high cell efficiency (fraction of solar energy which is converted into electrical energy) at low production costs. The photons with energy higher than the band gap of the semiconductor material used in this layer are getting absorbed and electron-hole pairs are generated. The separation of these charge carriers occurs via drift due to electric field established across the device and/or diffusion, depending on the adopted cell configuration. Further, the charge carriers are collected at the front and back contacts of the SC and transported to the external load. This function is commonly performed by either zinc oxide (ZnO) or tin-doped indium oxide (In_2O_3:Sn)-ITO, also called transparent conductive oxide (TCO) layers. Silver is commonly applied as metal bus bar transporting charge carriers generated in a solar cell to external load. The efficiency increase is achieved by addressing the cell in terms of electrical, optical and structural properties. The TCO-related optimization can be achieved by:

- Decrease of losses of generated charges when transported to the external load (i.e. decrease in the TCO resistivity);
- Decrease of absorption losses when the light travels towards the active layer using high band gap TCO materials. The two main examples are ITO (E_g=3.8-4.0 eV) and ZnO (E_g=3.3-3.4 eV);

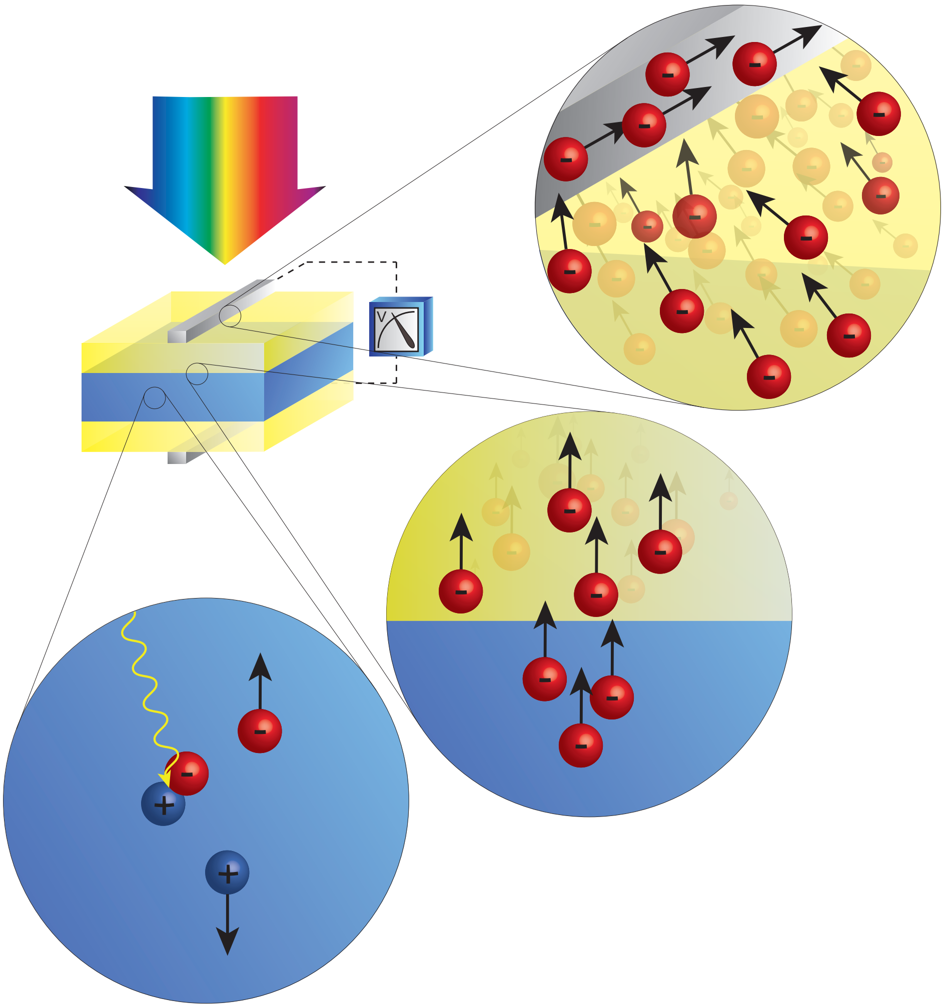

Figure 1.2. Basic principle of a solar cell. Upon absorption of the incident solar radiation the electron-hole pairs are generated. Further, they are collected and transported by TCO layers to the metal contacts with external load.

- Increase in absorption within the absorber layer by increasing the light optical path within the device. TCO scatters the light at the interface front TCO/absorber or back-reflects unabsorbed photons at the back contact;
- Increase in grain size and decrease of charge trapping centers can improve the mobility of the charge carriers.

This thesis addresses selected research lines all related to the role of transparent conductive oxides in PV, in particular ZnO. It should be mentioned, however, that PV is not the only application field for ZnO. Besides of the environmentally-friendly energy production, efficient energy utilization and energy saving solutions are parallel and equally important concerns for sustainable future. That is why the new concepts of energy-efficient cars, indoor and outdoor lighting [9–13], "green buildings" with "smart windows" and many others increasingly often appear nowadays [14–17].

Section 1.2 will further elaborate various PV applications, as being a target concept, where the subject of this thesis, zinc oxide, can readily contribute to.

1.2 ZnO in photovoltaic applications

ZnO production is approximately 10^5 tons/year and the large fraction of that is used in production of rubber (e.g. used to dissipate heat in car tires) and concrete (used to increase processing time and improves resistance of concrete against water) [18]. Also, ZnO is used in food and medical industries, in paints and anti-corrosive coatings for metals. Among the modern applications of ZnO gas sensors should also be mentioned, where a change in resistivity upon absorption of gas molecules is detected, optoelectronics and PV. The general properties of ZnO in PV are given in more detail in Table 1.1.

Below several examples are addressed to demonstrate diversity of modern ZnO applications.

Thin–film solar cells consist of thin (up to ∼1 µm) layers of semiconductor materials developed on inexpensive substrates such as glass, stainless steel and polymers. Thin films greatly reduce the amount of semiconductor material required for each cell, when compared to the silicon wafers (180-500 µm), thus lowering the production cost of PV cells [23]. The main examples of thin film solar cells are amorphous (*a*-Si:H), micro-crystalline (µc-Si:H) silicon-based, cadmium-telluride (CdTe) and Cu(In,Ga)Se_2 (CIGS)–based cells.

Table 1.1. ZnO properties relevant for PV applications

Function	Property
Optical transparency to the incident sunlight	Direct wide band gap of E_g=3.37 eV at 300 K [19]. Required transmittance $>$ 85 % for energy range above the band gap of the absorber.
Electrical charge transport	Addition of doping elements (commonly used are: Al, B, F, Ga, In [20]) changes the electrical resistivity from insulator through n-type semiconductor to metal-like (achieving resistivity of $\rho<10^{-4}$ Ω·cm for the best doped ZnO [21]).
Enhancement of the light scattering into absorber layer	High surface roughness of several tens of nanometers can be achieved either by natively grown ZnO, or after wet-etching procedure.
Suitability for device fabrication	Compatible with wet etching; resistant to hydrogen-rich plasma (e.g. during deposition of silicon layers on top) [22]. Competitor to ITO: partly due to the limited availability of indium and very high market price, partly due to the toxic nature and instability of ITO in the reducing environment.

Silicon-based thin film solar cells usually employ the multi-junction approach, where generally two absorbers characterized by different band gaps are stacked together in one single device (e.g. *a*-Si:H (0.1-0.2 µm-thick) and µc-Si:H (0.5-1.5 µm-thick) – "micromorph", tandem solar cells) [24]. In this way the entire solar spectrum can be efficiently used and the upper cell (E_g(*a*-Si:H)=1.7 eV), absorbing higher energy photons in the range 1.7-4.1 eV, act as a filter, allowing bottom cell (E_g(µc-Si:H)=1.1 eV) to absorb photons with lower energies 1.1-2.3 eV [24, 25]. In this case, ZnO can be used as a TCO – front and back electrode (Figure 1.3), transparent to the incident sunlight with ability to transport generated charge carriers to the contacts of solar cell.

Light absorption in the active layers of solar cell can further be enhanced by using textured ZnO, either natively grown by Chemical Vapor Deposition (CVD) [26, 27] or sputtering [28, 29], or by etching crater-like structures on the smooth surface of sputtered ZnO [30]. For example, CVD-deposited ZnO is currently being successfully applied as front and back contacts in industrial-scale 1.43 m^2 micromorph solar modules by Oerlikon Solar (www.oerlikon.com/solar) in the ThinFab™ production line with the record cell efficiency of 12.5 %. The tran-

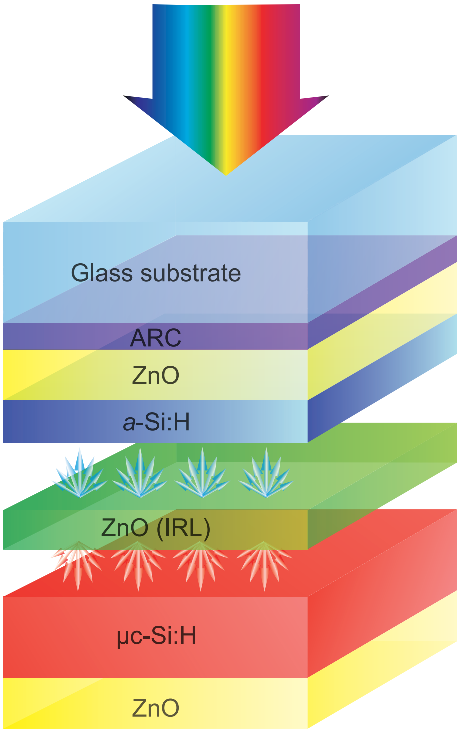

Figure 1.3. Basic design concept of silicon-based tandem solar cell with an intermediate reflective layer.

sition from flat as-deposited to textured etched aluminum-doped ZnO (ZnO:Al) was demonstrated to increase the short-circuit current in the µc-Si:H-based SC from 16.3 mA/cm^2 to 23.4 mA/cm^2 [30].

Also, ZnO can act as an intermediate reflective layer (IRL) in-between cells of the different band gaps, reflecting unabsorbed high-energy photons to the upper cell and transmitting low-energy photons to the lower one (Figure 1.3). The effect is achieved due to the refractive index contrast and intentional interface roughness between IRL and the top/bottom cells. In this way photocurrent in the top *a*-Si:H cell can be increased, which allows to make it thinner, thus reduce amount of recombination centers and make less prone to

ZnO functions in silicon-based thin-film solar cells are: optical transparency to the incident sunlight; transport of generated charges; enhancement of light scattering. If introduced as IRL, it allows for spectrally-selective reflection/transmission in-between sub-cells in a tandem configuration.

light-induced degradation, also known as Staebler-Wronski effect [31]. In the bottom cell IRL helps to reduce absorption loss by trapping the light within μc-Si:H layer, as demonstrated by Yamomoto *et al.* [32]. Also, the IRL should act as a tunnel junction for transport and recombination of generated charges between *a*-Si:H/IRL and IRL/μc-Si:H interfaces of the top and bottom cells, correspondingly.

Polycrystalline silicon thin film SCs on inexpensive glass substrates also use ZnO as a TCO layer [24, 33, 34]. CSG Solar achieved an efficiency of 10.4 % in this type of SCs applying ZnO for light trapping and transparent electrode functionalities [35].

ZnO also has TCO functionality in CdTe SCs (Figure 1.4), increasing absorption path in $\sim$5 μm-thick p-type CdTe absorber [36]. The best reported efficiency to date was announced in July 2011 by the US company First Solar (www.firstsolar.com) for a test cell to be 17.3 % and half a year later a record of 14.4 % for PV module.

In CdTe and CIGS thin-film solar cells ZnO has the following functions.
Doped ZnO: optical transparency to the incident sunlight; light trapping; transport of generated charges.
Undoped ZnO: providing local series resistance to eliminate electric shunts.
Zn-Sn-O layer is a valid alternative to the currently used CdS.

In CIGS cells (Figure 1.4) a 50 nm-thick intrinsic ZnO (i-ZnO) layer is deposited to provide a local series resistance and to prevent electrical inhomogeneities, e.g. short circuits [37]. Then, $\sim$1 μm-thick front TCO (Al-doped ZnO) layer is deposited on top [36]. The best CIGS SC efficiency reported to date is 20.3 % [38]. Thin Zn-Sn-O buffer layers can replace CdS with toxic Cd and positively contribute to one of the challenges in CIGS SCs - i.e. band alignment between TCO window layer and CIGS absorber [39–41]. Also, CdS deposition is the only wet step in the whole deposition process, which is not desirable for industrial-scale production.

In hybrid polymer-inorganic and dye sensitized SCs [42] ZnO is applied as an electron transport material and has become a favorable alternative to commonly used TiO$_2$ due to the possibility to be produced in a large range of nano-forms (nanorods, nanosheets, nanoribbons, etc.) by low-cost synthesis methods. The highest reported efficiencies appear in the range of 6.6-7.2 % for dye-sensitized cells, where ZnO nanoparticles and porous single-crystals are applied [43]. Important and challenging factors here are reproducibility of a ZnO nanostructure

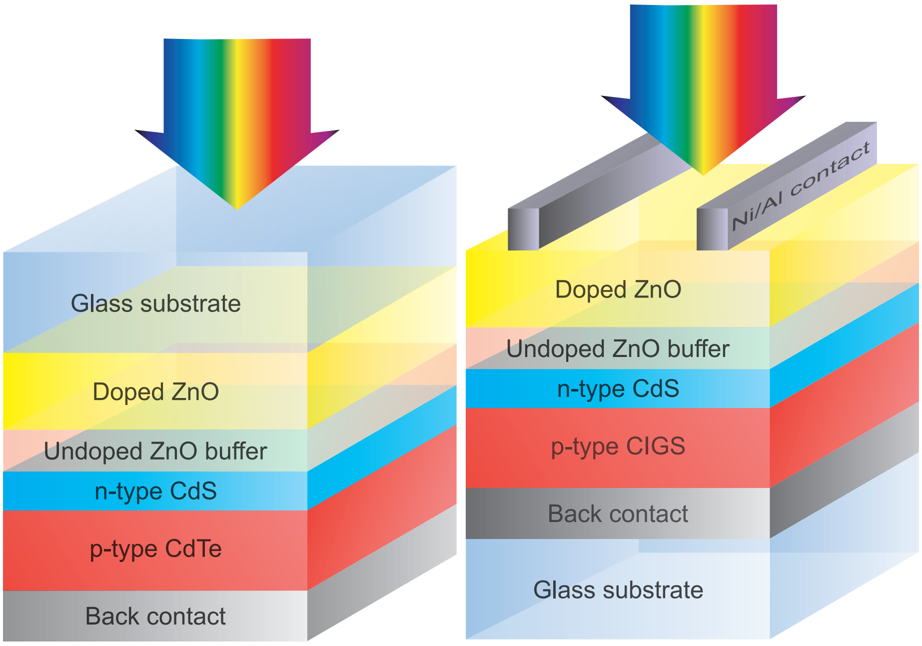

Figure 1.4. Basic design concept of: CdTe solar cell (left) and CIGS solar cell (right).

and control of its dimensions at large-scale production.

ZnO is used as a TCO and anti-reflection layer in heterojunction SCs with intrinsic thin layers (HIT), introduced by SANYO. The SANYO HIT cells show record open-circuit voltage (V_{oc}) of 0.739 V (typically ~0.6 V for conventional c-Si solar cells [36]) among all the PV devices based on bulk Si wafers. The best demonstrated cell efficiency up to now is 23 % [44] and module efficiency is 18.3 % (www.panasonic.net/energy/solar).

1.3 General properties of ZnO

From the vast field of ZnO properties presently known from both theoretical and experimental studies, the attention of this section is mainly devoted to the studies providing a background for the research developed in this thesis.

1.3.1 Structural properties

Undoped, doped ZnO and ZnO-based alloys crystallize under normal conditions in the hexagonal wurtzite-type structure [18], represented in Figure 1.5. It has a polar hexagonal threefold c-axis, parallel to z; the translation vectors a and b (a=b) include the angle of 120° and are situated in the base plane. The lattice constants mostly range from 3.2475 to 3.2501 Å for the *a* parameter and from 5.2042 to 5.2075 Å for the *c* parameter [19]. The ZnO crystal structure belongs to the space group $C_{6\nu}^4$ ($P6_3mc$) in the Schoenfiles (short standard) notation [45].

Since the wurtzite structure does not possess inversion symmetry, ZnO crystal exhibits crystallographic polarity, which indicates the direction of the bonds, i.e. (0001) planes differ from (000-1) ones. The convention is that the [0001] axis points from the face of the O plane to the Zn plane and is the positive z-direction. Zn-polarity means that the bonds along c direction are from cation (Zn) to anion (O). For the O-polarity it is vice versa. There are several material properties, which can also depend on polarity, such as growth, etching, generation of the defects, plasticity, spontaneous polarization and piezoelectricity [19]. Besides the primary polar plane (0001) and associated direction <0001>, which are the most common surface and direction for growth for wurtzite ZnO, there are many other secondary directions and planes in the crystal structure. The relation of this aspect with the electrical properties of ZnO will be extensively treated in Chapters 3, 4 and 5.

1.3.2 Electrical properties

Band structure

ZnO is a semiconductor with a direct band gap (E_g) of 3.44 eV at low temperatures and 3.37 eV at room temperature [46]. It is just above the visible light energy (1.65 eV < hν < 3.26 eV), which makes ZnO transparent in the visible range. A schematic representation of the ZnO band structure is given in Figure 1.6. Since ZnO is a direct band gap semiconductor, the minimum and maximum of the valence and conduction bands, respectively, are at the same point of Brillouin zone at k=0 (at the Γ-point) [18]. Undoped ZnO is an n-type semiconductor, however, the origin of that is still under debate. Some authors state that n-type conductivity is due to the point defects, such as Zn interstitials and O vacancies [47, 48]. Others suggest hydrogen, which forms a shallow donor in ZnO, to be a cause of n-type conductivity [49–52].

In n-type materials the Fermi level is closer to the conduction band. N-type doping introduces electron energy levels near the top of the band gap that can

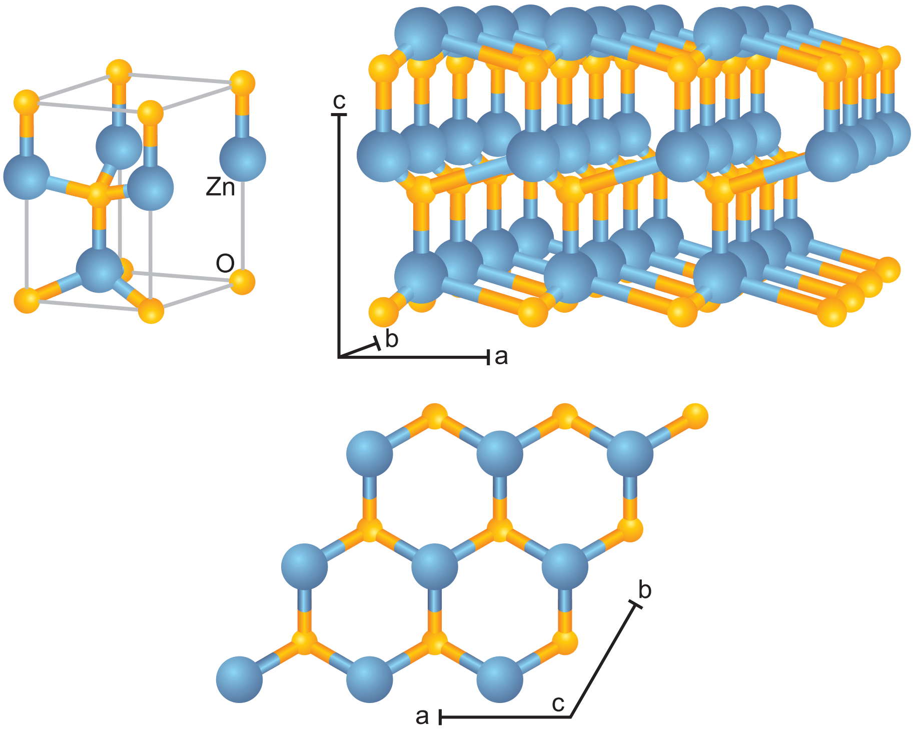

Figure 1.5. ZnO unit cell (left) and crystal structure (right-perspective view perpendicular to c-axis; bottom-view along c-axis on the Zn-terminated (0001) plane) (based on the figures published in the book of Ellmer *et al.* [45]).

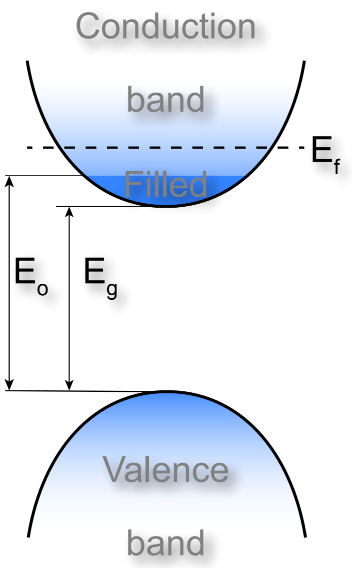

Figure 1.6. Schematic energy band diagram of doped ZnO as a degenerate semiconductor.

donate electrons into the conduction band via thermal or an optical excitation. The elements normally applied as intentional donor dopants are Al, B, Cr, F, Ga, In, Li and Na. Al, B, Ga, and In substitute Zn site in ZnO and act as shallow donors [20]. Fluorine can be easily incorporated in the oxygen site [53], donating one electron to conduction band. At high doping concentrations these individual impurity levels become close enough to merge into a band filled states, so such system tends to show conductor-like behavior and the Fermi level appears in the conduction band (Figure 1.6). However, there are still fewer charge carriers than in the conductor, therefore the behavior is intermediary between semiconductor and metal, so material is often referred as degenerate semiconductor. Figure 1.6 demonstrates band structure of degenerately doped ZnO, which leads to an unusual combination of high electrical conductivity and optical transparency in the visible range.

Due to the filled states in the proximity of conduction band minimum, the photons with the energy equal to E_g could not be absorbed, as it was noted by Burstein [54]. Rather, a little extra energy is needed to excite an electron into an empty state in the conduction band. The minimum energy needed for that to occur is E_O, as denoted in Figure 1.6. That is why the band gap has larger values as determined by optical measurements and the phenomenon is called Burstein-Moss shift.

Electrical transport

Degenerately doped ZnO exhibits a metal-like behavior, so the resistivity ρ is determined as following:

$$\rho = \frac{1}{\sigma} = \frac{1}{eN\mu} = \frac{m^*}{Ne^2\tau} \tag{1.1}$$

where σ is conductivity, e is the electron charge, N is the free carrier density, μ their mobility, m^* their effective mass[2], and τ is the average scattering time.

There are several events within a bulk ZnO crystal, which affect the mobility of the electrons:

- Optical phonon scattering, caused by interaction of the electrons with the electric field induced by lattice vibration polarization (polar longitudinal-optical phonons) at optical frequencies.

- Acoustic phonon scattering is a lattice deformations scattering because of a local energetic shift of the band edges.

- Piezoelectric scattering, caused by interaction of the electrons with the electric fields produced by the strain associated with acoustical phonons in the crystal. Among the polar optical, acoustic and piezoelectric scattering, the mobility at room temperature is limited by polar optical scattering.

- Neutral impurity scattering due to the interactions of the electrons with uncharged defects. Scattering at crystallographic defects, such as dislocations or stacking faults in single crystals can be neglected, since the concentration of such defects in single crystals is sufficiently low.

---

[2] Electron effective mass in solid state physics is a dynamical mass, which appears when electron moves in a periodic potential of the crystal. It can be shown that electrons and holes in a crystal respond to the electric field as if they were moving freely in a vacuum, but with some effective mass. It is usually defined in units of the rest mass of the electron ($9.11 \cdot 10^{-31}$ kg). Due to the non-parabolicity of the conduction band in degenerate semiconductors, electron effective mass increases with increase in carrier density. For undoped ZnO it is usually (0.25-0.28) m_e, for doped increases up to $0.5m_e$.

- Ionized impurity scattering is caused by screened Coulomb potential of charged impurities (dopants) or defects.

Besides the above mentioned scattering mechanisms in bulk single crystal ZnO material, one should consider additional scattering mechanisms, since ZnO films are usually polycrystalline when deposited by means of gas phase synthesis:

- Dislocation scattering, as a neutral impurity scattering, is a characteristic scattering process in polycrystalline materials, since they exhibit high concentration of crystallographic defects, compared to the bulk single crystals. However, this process is rarely used to explain experimental data on the carrier transport in TCOs, which is mainly due to the fact that in most works the density of defects was not determined [45]. The concentration of the dislocations is highly dependent on the actual deposition process.

- Grain boundary scattering caused by the charge accumulated at the interfaces between neighboring crystallites of ZnO. The grain boundary is a complex structure, usually consisting of a few atomic layers of disordered atoms, representing a transitional region between two neighboring crystallites. These defect zones are getting filled with electrons in n-type ZnO and a space charge region is formed on both sides of the grain boundary accompanied by a potential barrier for the electrons.

The transport of the charge carriers across a grain boundary was first described by Seto [55] for polycrystalline silicon. He distinguished two important contributions for that: thermionic emission for the carriers possessing high enough energy to overcome a potential barrier and tunneling (field emission) for the carriers with the energy less than the barrier height traveling through by quantum-mechanical tunneling. The former one characterizes lower doping levels, while for the very high carrier concentrations ($N>10^{20}$ cm^{-3}) in the grains, the width of depletion barrier reduces, enabling tunneling. The theory was also supported by works of Kamins [56] and Orton [57]. Detailed description of barrier height dependence from carrier concentration is given by Ellmer *et al.* [45]. For high carrier concentrations ($N>10^{20}$ cm^{-3}), which are necessary to achieve low resistivity, the barrier height is reduced in the presence of higher N. Because of the exponential dependence of resistivity from the barrier height, it will decrease faster than the resistivity of crystallites until the grain boundary region will no longer limit conductivity and the sample properties will correspond more closely to those of crystallites [56]. In this case ionized impurity scattering becomes dominant loss mechanism.

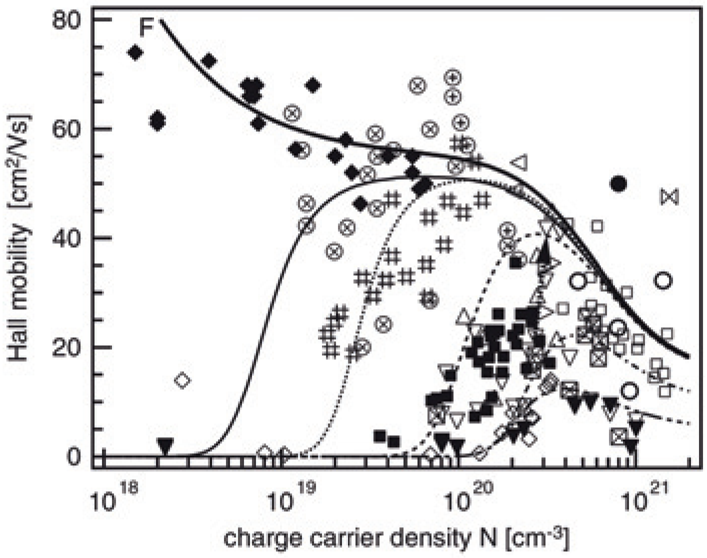

Figure 1.7. Hall mobilities of undoped and doped zinc oxide thin films as a function of the carrier concentration, from Ellmer and Mientus [58]. Symbols and fitting curves represent experimental data of several research groups.

By combining experimental data of several research groups for undoped and doped ZnO, Ellmer and Mientus [58] elaborated more on the electrical transport in ZnO. The results were summarized as a dependence of the Hall mobility from carrier concentration, shown in Figure 1.7. For carrier concentrations above 1-3·10^{20} cm^{-3} the single crystalline and polycrystalline films exhibit similar mobility, which means that the mobility is dominated by ionized impurity scattering in this carrier concentration regime. For a carrier concentration lower than 1-3·10^{20} cm^{-3} the mobility values of the polycrystalline and hetero-epitaxial films are considerably lower than that of single crystalline ZnO and steeply reducing with lower carrier concentration. This is caused by the limitation of the carrier transport by the grain boundary potential mentioned earlier. Large scattering of mobility as a factor 2-4 at the same carrier concentration in Figure 1.7 is attributed by the authors to point defects and/or dislocations at the grain boundaries leading to the higher grain boundary barriers for the lateral current transport. This points out on the importance of the control on the electrical properties in the ZnO layer

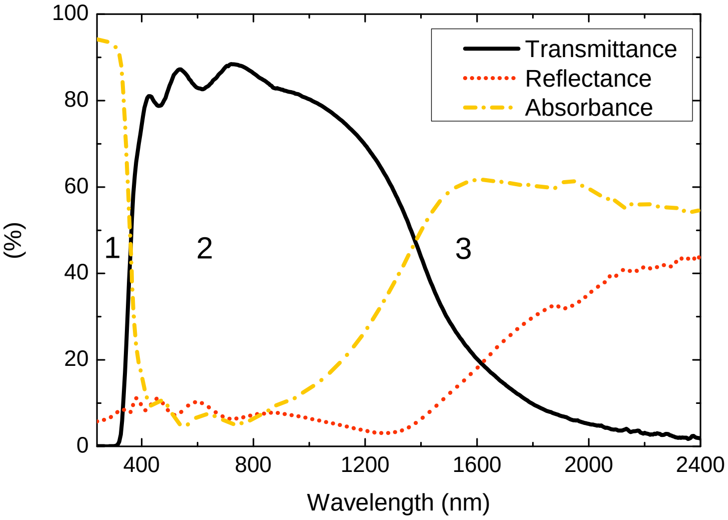

Figure 1.8. Transmittance, reflectance and absorbance spectra of a typical ZnO:Al film (thickness 515 nm) obtained in this work by expanding thermal plasma.

depending on the deposition technique. The lowest densities of grain boundary traps, and so the best mobility values, generally appear to be attributed to techniques with the lowest direct particle bombardment towards the growing film, i.e. pulsed laser deposition and magnetron sputtering.

1.3.3 Optical properties

Optical properties of materials are related to their electronic structure. High optical transparency of ZnO is a direct consequence of the wide band of 3.37 eV [46]. As for other semiconductors, optical properties of ZnO are related to both intrinsic and extrinsic effects. Intrinsic optical transitions are related to the transitions between valence and conduction bands, including excitonic effects (free and bound excitons) due to the Coulomb interaction. These latter are beyond the scope of this thesis and will not be discussed further, but the reader can refer to [45, 19]. Extrinsic properties are related to dopants or defects, which usually lead to discrete electronic states within the band gap, and therefore influence both optical-absorption and emission processes [19]. The transmittance, reflectance, and absorbance spectra of a typical Al-doped ZnO (ZnO:Al) are shown in Figure 1.8.

There are three characteristic regions in the spectra [59]:

- First, light with energy above the band gap is absorbed in band transitions. This occurs as an abrupt drop in transmission and increase in absorption at shorter wavelengths (<350 nm or 3.5 eV). This fundamental absorption edge shifts to shorter wavelengths with increasing carrier concentration. The shift is due to the filling of the states near the bottom of the conduction band and is well known as the Moss-Burstein shift [60].

- Second, a TCO ZnO:Al film must be transparent in the visible region of the spectrum, typically within $\lambda = 400–750$ nm ($h\nu = 3.1–1.7$ eV). There are several factors limiting transmission in this region: reflection losses at the optical interface; residual absorption due to free carriers and material defects; interference phenomena, depending on the film thickness.

- Third, another decrease in transmission and increase in reflection is observed at longer wavelengths $\lambda > 1000$ nm with a gradual long wavelength decrease in the transmission and the corresponding increase in the reflection. This transition, corresponding to a maximum in absorption, is referred to as the plasma wavelength (λ_p), where the frequency of the light is the same as the frequency of the collective oscillation of electrons in the material [60]:

$$\lambda_p = 2\pi c \sqrt{\frac{\varepsilon_0 m^*}{N e^2}} \tag{1.2}$$

where N is the carrier concentration, e the electron charge, ε_0 the permittivity of free space and m^* the electron effective mass. Oscillation of the electrons in phase with the electric field component of the incident light results in absorption. When $\lambda < \lambda_p$ the wave function is oscillatory and radiation can propagate, resulting in a transparent material. When $\lambda > \lambda_p$ the wave function decays and no radiation can propagate, resulting in the onset of the reflecting IR region. The carrier concentration is inversely related to the plasma wavelength, as λ_p is proportional to $1/\sqrt{N}$. Therefore, there is a trade-off between transmission and carrier concentration, so the range of near-IR transparency of the films is determined by the magnitude of λ_p, or, by carrier concentration N. At high N, which is necessary for good electrical properties, the control on the transmittance can be achieved by reducing the film thickness, keeping in mind the specific growth development of ZnO grains.

1.4 Deposition processes

Thin ZnO films are obtained by various fabrication processes yielding films with diverse structural, optical and electrical properties. The chosen deposition technique plays a significant role in determining the properties of the films. The most commonly used techniques for ZnO growth are:

1.4.1 Physical Vapor Deposition (PVD) techniques

Pulsed Laser Deposition (PLD) is quite new in the field of TCOs, very efficient technique and commonly used for epitaxial growth [61]. Nanosecond laser pulses with the energy density of more than 10^8 W/cm^2 are used to ablate the pellet of ZnO and ~1–3 wt. % Al_2O_3 placed in a vacuum chamber in front of the substrate [62, 63, 19]. The material gets vaporized from the pellet in a plasma plume, then transported in a plume with a possible interaction with a background gas and afterwards deposited on the substrate.

PLD ZnO:Al : excellent electrical ($8\cdot10^{-5}$ Ω·cm for 280 nm) and optical properties due to the pre-determined stoichiometry and low structural defects [21]. Mobility is approaching the values of single crystals. But, low volume deposition rate, energetically low efficiency process and with scalability issues [45].

The resistivity as low as $8.5\cdot10^{-5}$ Ω·cm and an average transmittance of more than 88 % in the visible range can be achieved for 280 nm - thick ZnO:Al films grown on Corning 7059 glass substrates [64]. The PLD ZnO films exhibit mobilities comparable to values reported for ZnO single crystals and very low trap density at the grain boundaries ($N_t=5\cdot10^{12}$ cm^{-2}) [58]. More detailed overview of PLD-deposited ZnO film properties, substrates, dopants and comparison with results of other techniques can be found in the references [45, 63].

Magnetron sputtering is one of the most extensively used techniques for deposition TCO films and ZnO in particular. The term "sputtering" designates the process in which highly energetic species, usually positive ions, eject atoms from solid target material. In magnetron configuration of the sputtering magnetically trapped electrons in the vicinity of the cathode raise the plasma density in front of the target. This gives rise to the deposition rate at the reduced thermal load on the substrate.

Sputtering generally provides smooth ZnO films with good electrical properties [65–67]. Highly conductive ZnO:Al films with resistivity (2-3)·10^{-4} Ω·cm could be obtained at 400-600 nm by sputtering [68–72], which is slightly higher than the values obtained by PLD [22]. This is attributed to the lower mobility due to the higher trap density at the grain boundaries [58]. In addition, a recent review of Ellmer and Welzel [73] drew special attention to the problem of ion bombardment towards the growing ZnO surface highlighting effects of induced film crystallization and crystallographic defects due to high energies of the impinging oxygen ions. To overcome this effect a variety of modified magnetron sputter processes can be used [74, 75, 45]. More extensive information about magnetron sputtering process could be found in literature [58, 76–81].

RF sputtered ZnO:Al : slightly higher than for PLD resistivity (2-3)·10^{-4} Ω·cm at 400-600 nm associated with reduced mobility values due to the higher trap density at the grain boundaries. High energy ion damage is especially detrimental in HIT and CIGS SCs, where ZnO is deposited on top of active layers underneath.

The thermal evaporation method is typically carried out in a furnace-tube system at high temperature up to ∼1100 °C [82, 83]. Despite of its simplicity, thermal oxidation deposition technique has found very little attention by research groups [84], mainly due to scalability limitations and has been mainly applied for growing various ZnO nanostructures at a lab-scale [82, 85, 86].

1.4.2 Solution-based techniques

Solution-based techniques are well suited for the deposition of ZnO on large areas without any vacuum process. The film preparation consists of three steps: (i) preparation of the precursor solution; (ii) deposition of the prepared solution on the substrate by the chosen technique; and (iii) heat treatment of the deposited film [87]. There is a vast variety of solution-based deposition configurations: chemical bath deposition [88]; spin-, dip-coating; slit, slot, die casting; spray pyrolysis, ink-jet printing and aerosol jet. Generally, solution-based techniques lead to the low film quality, with resistivity 5-10 times higher than for sputtered and PLD-deposited ZnO [59, 89]. One of the best resistivity results is achieved by dip-coating followed by annealing of deposited ZnO:Al films at 450 °C in vacuum, achieving resistivity of (0.7-1)·10^{-3} Ω·cm [59]. A more detailed overview of the variety of solution-based techniques is presented by Pasquarelli *et al.* [59] and the influence of the processing steps on the ZnO quality is reviewed by Znaidi [87].

1.4.3 Chemical Vapor Deposition (CVD) techniques

Chemical vapor deposition techniques are commonly used to deposit TCOs. They employ thermal decomposition of precursor gases and/or vapors in a vacuum reactor and further interaction with a hot substrate to form a thin film. CVD has the advantage of being a moderate temperature process (150 – 600 °C), with large scale production capability and growth rates higher than PVD. Another advantage of CVD is that as-deposited ZnO exhibits high surface roughness, which is beneficial for light scattering functionality in thin-film SCs.

CVD techniques can be divided into three categories: atmospheric pressure (APCVD), low pressure (LPCVD) and plasma enhanced (PECVD) chemical vapor deposition.

Atmospheric Pressure CVD (APCVD) of ZnO using different dopants has been thoroughly studied by Hu and Gordon [90–93]. APCVD is a diffusion-limited process, rather than kinetics-limited: the transport of the reactants to the growing surface is the limiting factor due to high process pressure. Lowering the pressure allows to increase deposition rate and reduce the deposition temperature below 400 °C [45]. Furthermore, deposition temperature can also be reduced when using plasma. Plasma-assisted APCVD of ZnO:Al at 225 °C showed clear advantages over thermal APCVD, achieving $2.2 \cdot 10^{-2}$ $\Omega \cdot$cm and no delamination from the substrate [94].

APCVD ZnO:Al: $3.3 \cdot 10^{-2}$ $\Omega \cdot$cm for 1350 nm-thick film at reduced deposition temperature. Transport of reactants to the growing surface is a main limitation, requires reduction of deposition pressure and quite high temperature.

Low-Pressure CVD (LPCVD) is very similar to the APCVD process. The main difference is associated with the lower pressure range from less than 1 mbar to about 30 mbar. LPCVD is characterized by the fast precursor transport to the growing surface and limited by the kinetics of reactions occurring at the surface [45]. The low pressure growth at <0.5 mbar is preferred to control chemical reactions in a gas phase during deposition [95–97]. Due to the limited increase in the grain size with thickness, achievement of resistivity $\sim 1 \cdot 10^{-3}$ $\Omega \cdot$cm is possible for

LPCVD-grown ZnO:B demonstrates limited increase in the grain size with thickness, therefore achievement of resistivity $\sim 1 \cdot 10^{-3}$ $\Omega \cdot$cm is possible for quite thick films: 1.4-5 µm.

quite thick films: 1.4-5 µm [98]. LPCVD-grown ZnO:Al has been demonstrated to be a valid replacement of ITO in a-Si:H thin film solar cells [99]. Establishment of the various surface texturing schemes for ZnO:B allowed to achieve 10 % relative efficiency gain in µc-Si:H solar cells [26], best a-Si:H cell efficiency of 10.9 % [100] and total current gain of 5 % in micromorph SC with efficiency of 13 % [27].

Atomic-Layer Deposition (ALD) can be carried out both at atmospheric pressure and in vacuum. The precursors - diethylzinc (DEZ, chemical formula $Zn(C_2H_5)_2$), trimethylaluminum (TMA, chemical formula $Al(CH_3)_3$) and H_2O are dosed into a chamber sequentially, separated in time by a purge step, which is typically used to remove excess precursors and reactants [101–103]. Oxygen plasma could also assist ALD process [104], replacing H_2O. Simultaneous dosing of DEZ+TMA provides more efficient intermix and homogeneous Al-doping, resulting in resistivity as low as $6 \cdot 10^{-4}$ $\Omega \cdot$cm at 105-140 nm thickness [105]. The growth rate during ALD process is strongly limited by the purge steps between the time-sequenced injection of the precursors. It has been overcome in spatially separated ALD configuration, where precursors dosing occurs in different zones of the reactor and a moving substrate is sequentially exposed to each of these zones [106].

ZnO:Al resistivity as low as $6 \cdot 10^{-4}$ $\Omega \cdot$cm is achieved in ALD process for the thickness 105-140 nm, but low growth rate might be the issue.

Plasma-Enhanced CVD (PECVD) is technically a LPCVD process, with a difference that precursor dissociation chemistry is initiated by plasma, changing overall reactivity to a more complex reaction routes in a gas phase. The addition of a plasma environment allows dissociation of precursors in the gas phase leading to reduction of substrate temperature (200 °C and below) [107–109]. Furthermore, the presence of ion bombardment can contribute to the specific growth development of the deposited film [110, 111]. This provides resistivity level of $\sim 8 \cdot 10^{-4}$ $\Omega \cdot$cm with a carrier concentration of $5 \cdot 10^{20}$ cm^{-3} and mobility of ~ 15 cm^2/V$\cdot$s, for the case of Ga doping at the substrate temperature of 350 °C and thickness 410 nm [112].

Resistivity of $8 \cdot 10^{-4}$ $\Omega \cdot$cm in PECVD ZnO:Ga achieved at the thickness of 410 nm.

Metal-Organic PECVD (MO-PECVD) is a special case of PECVD process, where metal-organic (chemical compounds containing metals and organic ligands) precursors are used as sources of growth species to be dissociated by plasma. Few examples of PECVD systems reveal a limited knowledge of the reactions occurring in the plasma and at the substrate [108, 110, 113–115], due to complexity related to the metal organic precursors used. At the same time, this approach allows for a large variety of growth modes and morphologies, each with specific structural, optical and electrical characteristics [116, 112, 117]. In this section a detailed description of MO-PECVD technique is given, in particular, the configuration used throughout this study.

ZnO:Al films in this study were deposited by means of a remote plasma - the Expanding Thermal Plasma (ETP) technique [118]. It has proven to be a viable deposition tool for silicon oxide [119, 120] and silicon nitride [121, 122]; hydrogenated amorphous silicon [123, 124] and carbon [125, 126]; and, zinc oxide [116, 117]. The best resistivity level achieved with ETP before this work was $8\cdot10^{-4}$ Ω·cm, as measured for 1100 nm ZnO:Al film deposited at a substrate temperature of 200ºC [116].

As shown on the schematic representation (Figure 1.9), the general operation principle of the ETP technique is based on the interaction of generated plasma jet with precursors injected downstream thus creating reactive species responsible for film deposition. The plasma source is a cascaded arc unit, where a DC discharge is generated between three cathodes and grounded anode plate, throughout 4 mm channel in the stack of circular copper plates with boron nitride insulation rings in-between. The cathodes, plates and anode are water-cooled to prevent melting of the cascaded arc components. The argon plasma is created at sub-atmospheric pressure (typically $0.3\text{-}0.4\cdot10^{5}$ Pa). Due to the pressure difference, the ionized argon expands through 4 mm opening in the nozzle of the cascaded arc into the low pressure deposition chamber (typically 30-200 Pa) and dissociates precursors injected through rings into the plasma jet: oxygen was injected at 6.5 cm downstream from the plasma source; evaporated and pre-mixed DEZ and TMA were injected further downstream at 30 cm from the plasma source. The growth precursors were convectively transported with the flow towards the substrate placed at 50 cm from the plasma source to deposit the ZnO:Al film.

ETP MO-CVD ZnO:Al resistivity: $8\cdot10^{-4}$ Ω·cm at the thickness of 1100 nm. This growth mode is characterized by the undesired gradient in resistivity.

Substrate temperature could be controlled within the range of 20-400 °C. Usu-

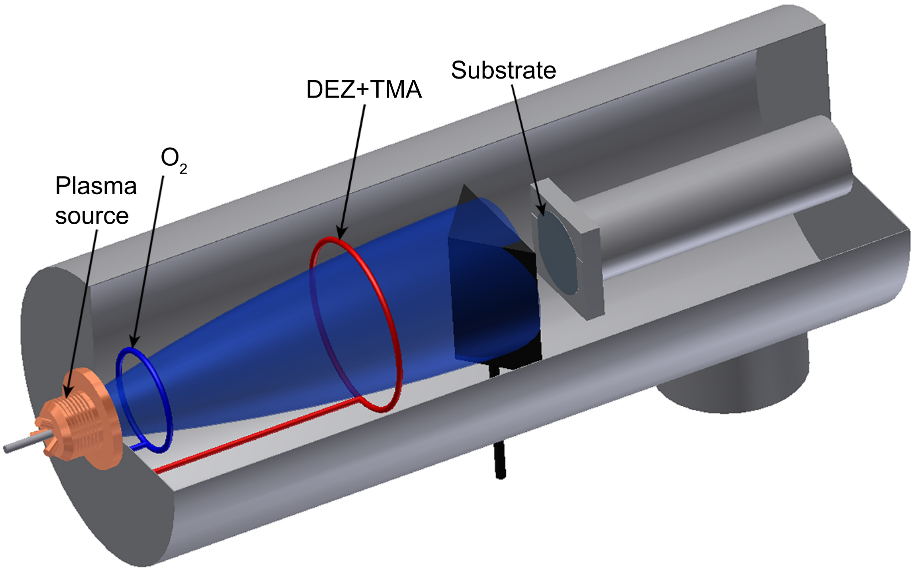

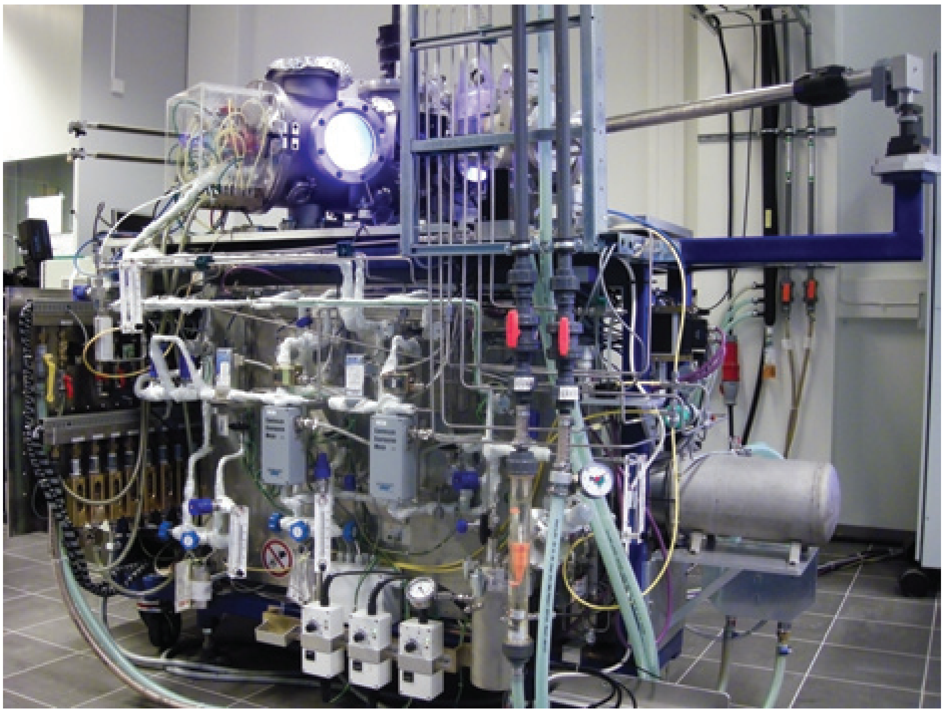

Figure 1.9. Schematic representation of ETP deposition geometry and the photograph of ZOPHIA (Zinc Oxide for PHotovoltaIc Applications) experimental setup.

ally, there were 3 substrates, all of 1 inch^2 size, placed in a row on the sample holder for each deposition and the sample holder was loaded on the heater chuck through adjoining load-lock chamber. Crystalline silicon <100> with native oxide, 400 nm-thick thermal SiO_2/c-silicon <100> and Corning 7059 glass were used as substrates. Helium gas was injected through the 3 holes in the sample holder to maintain a good thermal conductivity between the substrates and the sample holder. A Pfeiffer Vacuum Prisma QME 200 quadrupole mass-spectrometer was located on a side of the deposition chamber at the substrate level to monitor the background gas composition through 100 µm orifice. The deposition chamber is equipped with several ports used to attach Spectroscopic Ellipsometry equipment and Langmuir probe for diagnostics, sputtering source for deposition Ag nanoparticles and 3 viewing ports – 2 on the both sides at the level of 1st injection ring and one at the substrate level. Shutter in front of the sample holder was used to protect the substrates from deposition before all the flows are set and stabilized and after the experiment time is over. Inner walls of the deposition chamber were covered with Al foil, which was regularly replaced as a part of the reactor cleaning procedure.

The advantages of the ETP MOCVD process are:

- Remote plasma environment – plasma generation, precursor dissociation and film deposition are geometrically separated;
- Convective transport of reactive species – potential for high growth rates;
- Low energy of ions arriving at the substrate – favorable conditions for low defect formation (contrary to, e.g., sputtering).

The precursor dissociation is dominated by ions (T_e=0.1-0.3 eV) and the plasma processes are characterized by a combustion chemistry with negligible ion bombardment of the growing film, compared to, for example, magnetron sputtering. The ionization degree of the argon flowing through the cascaded arc is up to 10 % [127], which is controlled by the arc current and argon flow. The technique offers a multiple parameter control of the film properties (morphology, electrical and optical properties) via plasma properties (pressure, chemistry) and substrate temperature.

It was previously demonstrated that the control on the ZnO properties can be achieved by tuning the deposition pressure and temperature (to control film morphology); zinc to oxygen ratio (to control deposition rate and electrical properties) [117]. Presence of reactive species and corresponding processes in depositing plasma were reviewed and several suggestions regarding the growth mechanism were given [114]. Furthermore, it was shown that the control of the deposition pressure plays an important role in development of the electrical and structural properties of the film as function of the thickness [128]. It was observed that there is a correlation between thickness-dependent grain size and sheet resistance at "high" (1.5 mbar) and "low" (0.38 mbar) deposition pressure [116]. The "low" pressure conditions exhibit very limited lateral grain development, thus constant sheet resistance as a function of thickness, so called "pillar-like", or, columnar growth development. At "high" pressure there is a gradual increase in the lateral grain size and corresponding reduction of sheet resistance with increase in thickness, so called "pyramid-like" growth. The work presented in this thesis is focused on understanding the cause of the "pyramid-like" growth and providing the ways to control this type of growth. From the early works on "pyramid-like" ETP-grown ZnO:Al and the experimental data in this thesis, next section introduces and provides a detailed preknowledge for the following chapters, based on relationships between the growth and physical properties.

1.5 Relationships between the growth and physical properties of ETP "pyramid-like" ZnO:Al

A typical example of pyramid-like growth is demonstrated on the Scanning-Electron Microscopy image shown in the Figure 1.10. As it was earlier demonstrated [116], the ZnO lateral grain size is increasing with the film thickness. In that way, the initial growth stage is characterized by a high nucleation density and small crystallites, which develop in lateral, as well as in vertical directions as the growth proceeds. Some of them are being suppressed, in a favor of others to develop in lateral direction even further. Thus, the formed grains have pyramid-like profile, with the vertex of the pyramid pointing towards the substrate, where the grain nucleated. Also, the top part of the grain is not flat, but rather has a sharp vertex, which is advantageous for light scattering capability in SCs. This kind of structural development has a pronounced effect on the electrical properties, since the grain boundary traps, as addressed earlier in subsection 1.3.2, strongly affect electrical transport in the lateral direction. Since thinner films have a smaller grain size, they are more prone to electrical losses at the grain boundaries, compare to the thick ones with the large grain size. Another characteristic parameter is the native surface roughness, which is directly related to the lateral size of

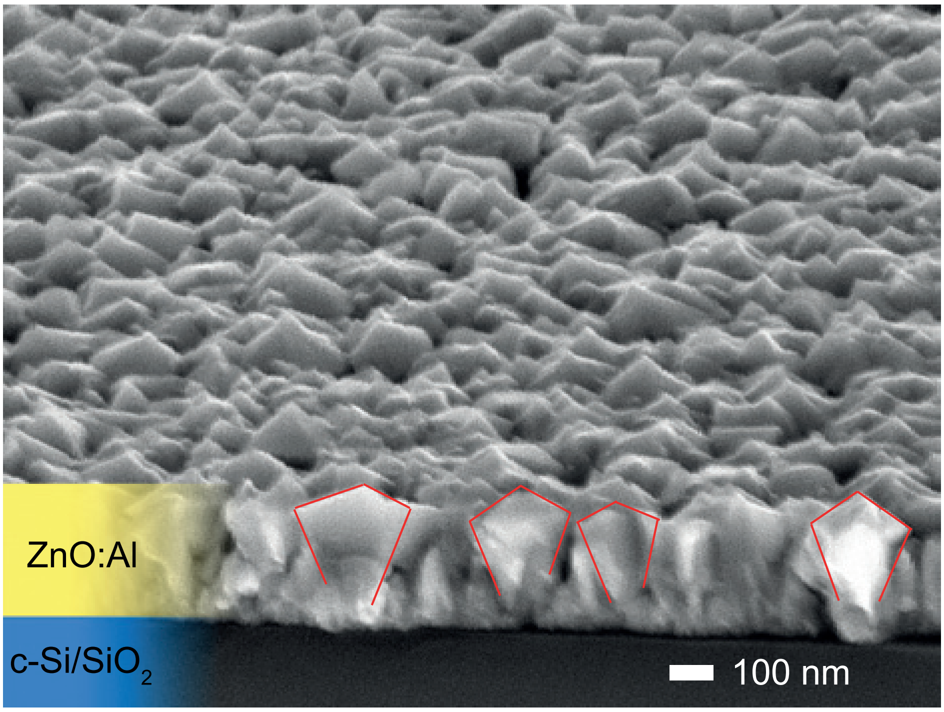

Figure 1.10. Cross-sectional view of pyramid-like growth (outlined red contours) development of ETP grown ZnO:Al grains.

pyramid-like grains and increasing linearly with increase in the grain size (here and further in the text the term grain size will designate lateral grain diameter of the largest top part of the developed crystallite). However, deposition pressure was observed to be a powerful tool to determine the ETP growth of ZnO [116], reducing the grain size and switching from pyramid-like to pillar-like mode just by reducing the pressure. The pillar-like mode is characterized by limited development of the grain size during the film growth such, that the crystallites look like densely packed parallel columns with domed tops and the surface roughness is low.

The optical characteristics of pyramid-like ZnO:Al can be deduced from its dielectric function $\varepsilon(\omega)$. This complex function is frequency dependent and related to material refractive index (n) and extinction coefficient (k) as following:

$$\sqrt{\varepsilon(\omega)} = n + ik \tag{1.3}$$

For free electrons in metals the complex dielectric function is given by the

Drude model and can be also applied for degenerately doped ZnO:Al [60]:

$$\varepsilon(\omega) = (n - ik)^2 = \varepsilon_\infty - \frac{Ne^2}{\varepsilon_0 m^* \left(\omega^2 - \frac{i\omega}{\tau}\right)} \tag{1.4}$$

where ε_∞ is the high frequency dielectric function, τ the scattering time. Since the Drude model is valid at hν $<<$ E_g, it has to be combined with another function, e.g. a Lorentz oscillator, to account for the inter-band transitions and to obtain the optical properties of the material in the broad range of the spectrum, from UV to near-IR. This function was applied to study electrical properties of ZnO:Al obtained in this work by accurate and non-destructive optical measurement technique-Spectroscopic Ellipsometry (SE).

The name "Ellipsometry" comes from the fact that the polarized incident light (on the left in the Figure 1.11) becomes "elliptical" upon reflection from the sample (on the right in the Figure 1.11). As shown in the Figure 1.11, SE measures amplitude ratio ψ and phase difference Δ between p- and s-polarized light waves as given by:

$$\rho = \tan\psi \exp(i\Delta) = \frac{r_p}{r_s} = \frac{\left(\frac{E_{rp}}{E_{ip}}\right)}{\left(\frac{E_{rs}}{E_{is}}\right)} \tag{1.5}$$

where indices p and s stand for p- and s-polarized components of light (p corresponds oscillations parallel to the plane of incidence; s to the oscillations perpendicular to the plane of incidence and parallel to the surface plane); i and r for incident and reflected light.

For the ZnO:Al samples obtained in this work, a combination of Drude and Tauc-Lorentz (TL) was used, similar to reported by Fujiwara and Kondo for Ga-doped ZnO [129]. Dielectric functions resulted in a quite good fit of the experimental data and in a strong match with other external measurements. The dielectric function of ZnO:Al $\varepsilon(E) = \varepsilon_1(E) - i\varepsilon_2(E)$ is expressed by:

$$\varepsilon(E) = \varepsilon_{TL}(E) + \varepsilon_D(E) \tag{1.6}$$

where $\varepsilon_{TL}(E)$ and $\varepsilon_D(E)$ stand for dielectric functions calculated by the TL and Drude models, respectively. In the TL model, the dielectric function is obtained from five parameters (A_{TL}, C, E_T, E_0 , $\varepsilon_1(\infty)$), which represent the amplitude, broadening parameter, Tauc optical gap, peak transition energy, and energy-independent contribution to ε_1(E), respectively [130]. ZnO:Al films de-

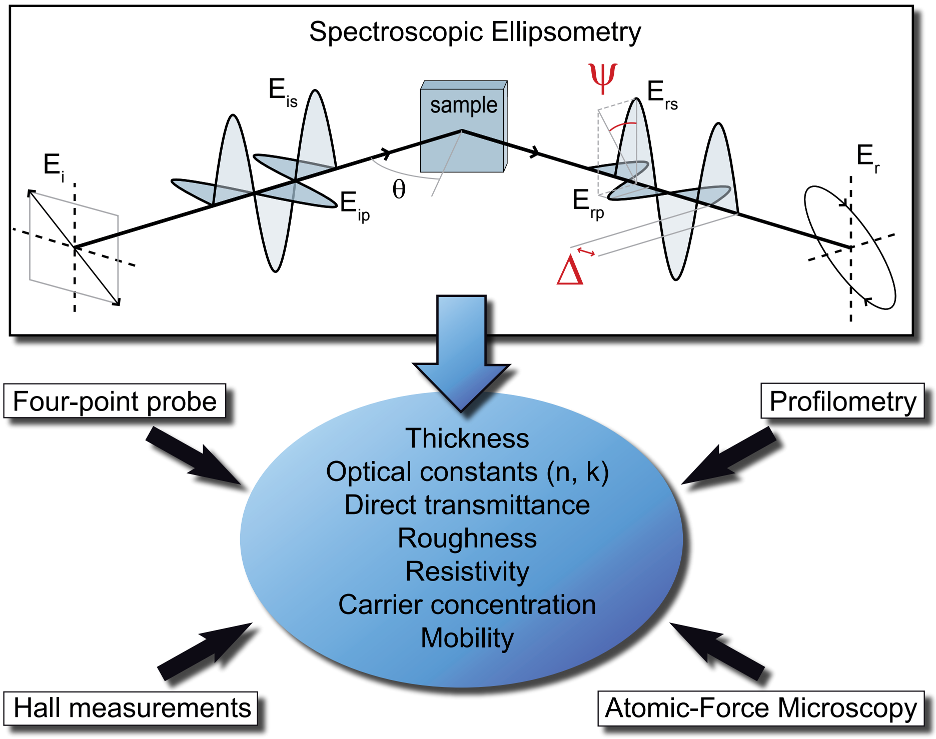

Figure 1.11. Measurement principle of spectroscopic ellipsometry and list of the main film properties which can be obtained for ZnO with this technique.

posited on c-Si wafers with ~400nm of SiO_2 were analyzed with SE using the model shown in the Figure 1.12.

It consists of substrate (c-Si with SiO_2 measured before ZnO:Al deposition, to provide a good base for fitting ZnO:Al layer on top), bulk ZnO:Al parametrized with dielectric function as in Formula (1.6) and a roughness layer on top (effective-medium approximation of 50 % ZnO:Al and 50 % voids). To overcome the challenges of film inhomogeneity with thickness and high surface roughness, the measurements were performed in a wide wavelength range (250 to 1700 nm) at several angles of incidence (50 to 80 degree with a step of 5). Results of this procedure are shown in the Figure 1.13, where mobility, carrier concentration and roughness are plotted as a function of effective thickness (taken as a sum of bulk layer thickness and $\frac{1}{2}$ of surface roughness layer).

Since Drude model consider independently moving free electrons, it is a Lorentz oscillator without restoring force and a main fitting parameter unscreened plasma

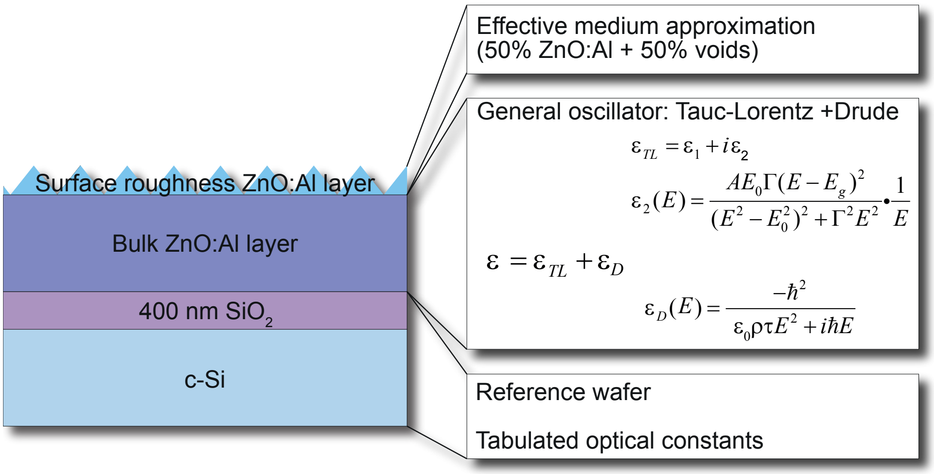

Figure 1.12. Optical model used in Spectroscopic Ellipsometry analysis of ZnO:Al.

frequency ω_p. From fitting the Drude term of dielectric function carrier concentration N_{opt} can be determined, when setting effective mass m*:

$$\omega_p^2 = \frac{e^2 N_{opt}}{\varepsilon_0 m^*} \tag{1.7}$$

The best fit was achieved at the m*=0.4me, which corresponds to degenerately doped ZnO:Al. The broadening from the Drude function gives optical electron mobility:

$$\mu_{opt} = \frac{e\tau}{m^*} \tag{1.8}$$

This optical mobility is fundamentally different from the one obtained from electrical measurements – Hall mobility. Contrary to the Hall measurements, optical electron displacement by SE is very limited, usually smaller than the grain size. Therefore, SE measurements are generally considered to account for intra-grain properties, but not for the grain boundary transport. However, it is important to determine in-grain electrical properties, since they can provide complimentary information about the effect of ionized impurity scattering on electrical properties. Also, if compared with electrical measurements, results of optical measurement can demonstrate how strong is the influence of grain boundary scattering on the effective resistivity of the ZnO:Al film.

For the thickness range above 400 nm both SE mobility and carrier concen-

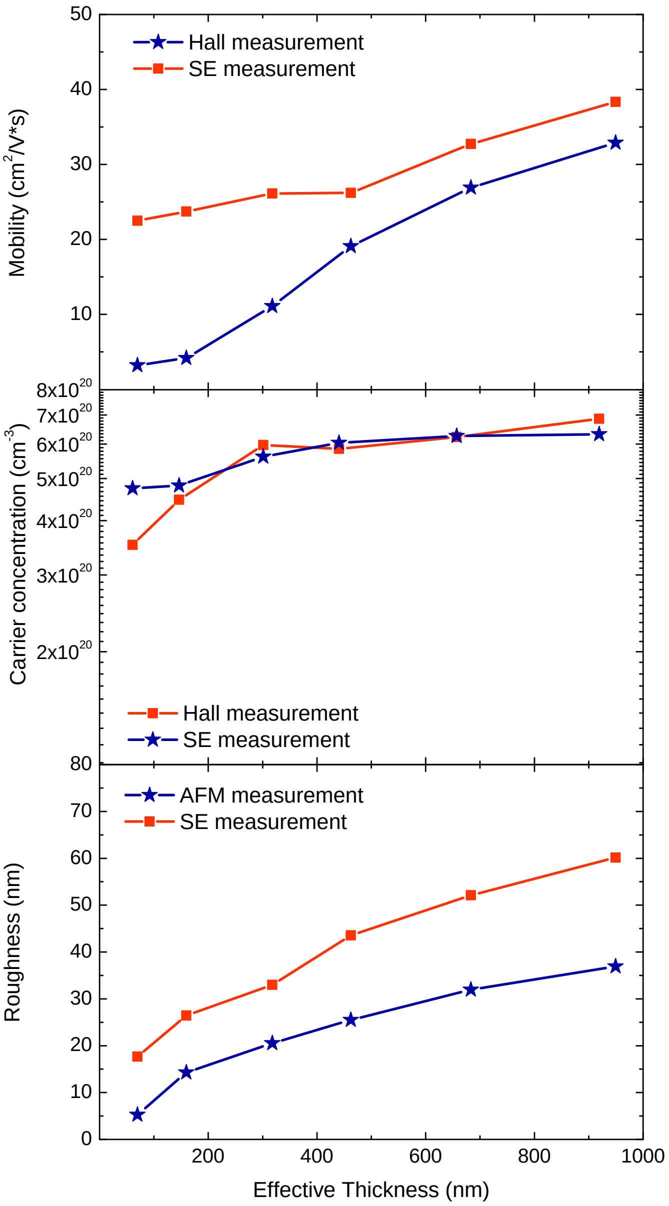

Figure 1.13. Comparison of the ellipsometry results with those obtained by Hall and AFM measurements for the same ZnO:Al samples. The effective film thickness (thickness of the bulk layer + 50 % of thickness of surface roughness layer) is indicated on the horizontal axis.

tration nicely correlate with the Hall results. As it was addressed earlier in subsection 1.3.2, one of the major loss mechanisms in polycrystalline material is the potential formed due to the high trap density at the grain boundaries of these layers. So, slightly lower Hall mobility is attributed to grain boundary losses.

For the thinner films ($<$400 nm) the Hall mobility is significantly lower, because, unlike SE measurements, it includes carrier transport across the grain boundaries, causing grain boundary scattering. Since the structural feature of these ZnO:Al films is a pyramid-like grain development, thinner layers have effectively larger volume fraction of the grain boundaries due to the small grain size. Therefore, the grain boundary barrier is especially detrimental for thinner layers, so the largest discrepancy between Hall and SE measurements is for the thinnest 90 nm film. The difference in carrier concentration between optical and electrical measurement of the thin films is caused by inaccuracy of Hall measurement due to the high film resistivity at this low thickness range. Correlation of the surface roughness with the Root-Mean-Square (RMS) values from AFM could be also considered as reasonably good, within a general empirical observation, that AFM roughness is about 30 % lower than the one from SE. The general trend towards increasing RMS roughness, as it was addressed in subsection 1.3.1, is related to increasing grain size and so the height of the vertexes of the grains.

As the resistivity ρ is inversely proportional to mobility μ (see Formula 1.1), the mobility trend at the constant N rationalizes the presence of the gradient in resistivity ρ, which is developed as function of the film thickness (Figure 1.14) and related to the pyramid-like growth development in Figure 1.10. This is a characteristic feature of CVD techniques in general and can be observed at a different extent (usually, more than factor of 10 resistivity reduction in the wide thickness range of several hundred nm). Small grains develop at low film thickness and characterized by charge carrier trapping phenomena occurring at the grain boundaries. As the grain further develops in lateral size as function of film thickness, scattering at the grain boundaries becomes progressively less dominant with respect to other mechanisms (e.g. scattering at ionized impurities) and lower resistivity values are achieved for large film thickness, as it has been addressed in Figure 1.13. As can be seen from the Figure 1.14, the ETP process has a potential to achieve even lower resistivity, than demonstrated before this work [116], close to the best values for magnetron sputtering (about (2-3)$\cdot 10^{-4}$ $\Omega\cdot$cm). This is an effective, or, averaged resistivity value, integrated over the whole film thickness. Obviously, due to the resistivity gradient in ETP ZnO:Al, the resistivity of the

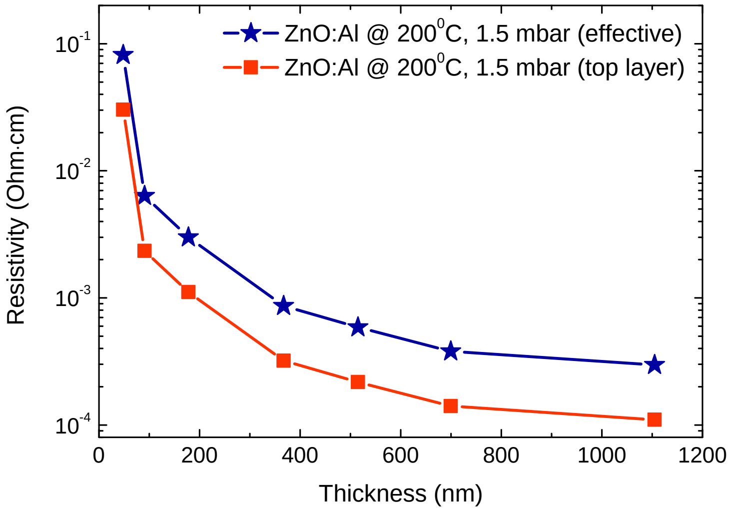

Figure 1.14. Characteristic resistivity gradient in ETP grown ZnO:Al at pyramid-like growth conditions in this work (effective resistivity and the values estimated for the top layer).

top part of the film is influenced by the more resistive underlying part. To account for that and demonstrate the quality of the top layer, Volintiru *et al.* [116] performed a correction, which takes into consideration the steepness of the resistivity gradient. With a similar correction procedure applied here, the effective resistivity of $3.0{\cdot}10^{-4}$ Ω·cm measured at 1100 nm would be equal to $1.1{\cdot}10^{-4}$ Ω·cm for the top part of the ZnO:Al layer at that thickness. Quantitative comparison of the top-layer resistivity with the effective resistivity at each film thickness in this deposition series can be seen in the Figure 1.14. Application-wise, achievement of low resistivity for large thickness will increase production costs of ZnO:Al layer and will undesirably raise the price of the device in which it is applied. The control on the growth of ZnO:Al layers is, therefore, essential to define the properties of a ZnO:Al layer, as transparent semiconductor.

The growth control requires control over nucleation and grain size development during the growth. Although several aspects to control ZnO growth were previously demonstrated, there are still some remaining challenges. The main one is to be able to control resistivity gradient, while maintaining good electrical properties and high optical transmittance. That implies a more detailed understanding of growth, where factors affecting grain size development and implications of that development are studied in detail. For example, as derived from the Figure 1.13, grain boundary scattering should be reduced significantly. One of the ways is to use hydrogen for passivation grain boundaries. Moreover, hydrogen is the strongest candidate for being unintentional, n-type "extrinsic dopant", since it is present in almost every growth and processing environment. However, H in interstitial state is very mobile and can easily diffuse out of the samples [131]. Recently it has been suggested, that H can also substitute for O in ZnO and act as a shallow donor. Substitutional H is much more stable than interstitial H, so can explain the stability of n-type conductivity [132] and be a good candidate to be incorporated in grains and at the grain boundaries. The concentration of hydrogen varies between 10^{15} cm^{-3} in single crystals and 10^{20} cm^{-3} in polycrystalline ZnO deposited by magnetron sputtering [133] and CVD. Understanding of the plasma processes, which determine the ZnO growth and properties, is also necessary to know the growth mechanism and its correlation with the electrical properties of the actual film.

1.6 Scope and outline of the thesis

The field of ZnO applications is quite large. In the photovoltaic area, it ranges from thin film solar cells, LEDs, up to large-area coatings for smart windows. All of these applications are especially important for sustainable energy-efficient future. The extensive range of applications requires an educated design and engineering of the ZnO layer in terms of structure and optoelectronic properties, amongst others.

The work presented in this thesis is focused on one particular application – thin film solar cells. However, this application also involves variety of possible structures and different functions, which ZnO can perform, as demonstrated earlier in section 1.2. Thus, the ability to achieve required properties for each specific application/function necessitates of a good control on the ZnO growth on the basis of the understanding of its growth mechanism. Additionally, each specific deposition technique has its own peculiarities and plays a significant role in determining the properties of the films. Particular challenges of the case of ETP process are the complex gas phase reactions related to the metal-organic precursors used and the strong dependence of electrical properties on the film thickness – the so called resistivity gradient (Figure 1.14). The latter is a characteristic of all CVD techniques, but the main focus of this thesis is on ETP. The resistivity gradient requires growing thick films to be able to achieve a reasonably low resistivity.

Certainly, this affects optical transmittance of the deposited layer and increases production cost, which can respectively result in reduced performance of a solar cell and higher market price. The understanding of the deposition process in terms of plasma-related and structural mechanisms, both at the nucleation stage and during the growth, is required to be able to control the resistivity gradient and formulate the routes towards achievement better optoelectronic properties of ETP ZnO:Al.

Hence, the study of the ETP ZnO growth development is a topic of much interest in this PhD project. In this respect the IRTES project was initiated between TUDelft, NUON Heliantos (now Hyet Solar) and TU/e to provide solutions towards higher efficiency thin film silicon based solar cells. The task of TU/e was to provide a process control over ZnO growth development to be able to deliver films with tailored structure, surface texture, conductivity and transmittance.

Therefore, the goal of this research can be summarized as:

- to provide understanding on ZnO:Al growth development in the ETP process with a focus on the gradient in ZnO:Al resistivity which develops as function of the film thickness;
- to find the routes for the improvement of the electrical and optical properties of ZnO:Al by controlling the growth process at the nucleation stage, during the development of the bulk and/or in a post-deposition treatment.

Generally, both the electron transport properties and the optical constants in the ultra thin films are thickness dependent [60]. This may be caused by: (a) the presence of oxygen-rich surface layers, such as grain boundaries; (b) increased mobility resulting from increased grain size and (c) change in the preferred orientation of crystallites with thickness and, consequently, variation in the refractive index.

These common mechanisms were also discussed throughout this work and addressed as follows:

- The presence of oxygen at the grain boundaries can be addressed when studying the evolution of the electrical properties and grain size development with the increase in thickness. The addition of hydrogen to the system can have a passivation effect followed by improved electrical properties, as demonstrated in Chapter 2.
- The improved mobility with an increase in grain size, as well as the evolution

of crystallographic orientations in ZnO:Al with thickness are extensively addressed in Chapters 3 and 5.

- Void development throughout the film bulk is quite common in CVD growth, due to the increasingly extending lateral grain size with increase in film thickness. The distribution of the voids within the layer determines the electrical, optical properties and is related to the specific deposition technique and experimental parameters. This is further addressed in Chapters 3, 4 and 5.

- The electrical conductivity, optical transparency in the visible region and IR reflectivity are interrelated and are markedly dependent on the deposition conditions, in particular on the oxidation processes that occur during or after deposition. Therefore the role of atomic and molecular oxygen was examined under the deposition conditions and correlated with the material properties in Chapter 4.

Thus, the outline of the remaining part of this manuscript is the following:

- Chapter 2 addresses the route to control the resistivity gradient by introducing hydrogen diffusing from silicon capping layers on top of ZnO:Al, i.e. a configuration adopted in poly-Si solar cells. After high temperature processing, the resistivity gradient was drastically reduced and the conductivity of ZnO:Al films improved by a factor of $\sim$50 (for $\sim$100 nm ZnO:Al). This was attributed to the improved quality of the grain boundaries due to the hydrogen passivation;

- Chapter 3 shows the correlation between structure, electrical and optical properties of ZnO:Al. It also demonstrates the way to control the resistivity gradient and to improve electrical properties of ZnO:Al by enabling a different growth mode. Also, it provides a detailed study of the layer development with increase in film thickness in terms of electrical, optical properties and structure. This gives a valuable insight for the growth development control and understanding of the ZnO:Al growth mechanism;

- Chapter 4 elaborates the processes in the plasma and at the substrate surface, associated to the different growth modes and reduced resistivity gradient, as investigated in Chapter 3. The role of atomic oxygen in the growth of ZnO:Al film is highlighted. A possible mechanism of ZnO:Al growth in ETP is proposed;

- Chapter 5 demonstrates the importance of the substrate effect on the nucleation, subsequent growth and resulting electrical properties of ZnO:Al, with the aid of Ag nanoparticles sputtered prior to the ZnO:Al deposition. This approach allows for the earlier onset of the dominant <002> orientation with effective suppression of other, competitive orientations. This leads to a reduced void fraction and a more compact structure, which is reflected in the improved electrical properties and optical transmittance of ZnO:Al.

Bibliography

[1] *World in transition: a social contract for sustainability. Flagship report*, German Advisory Council on Global Change (WBGU) (2011), ISBN 978-3-936191-37-0.

[2] *America's Climate Choices*, Committee on America's Climate Choices National Research Council (2011), ISBN 9780309145855.

[3] *International Energy Outlook 2011*, U.S. Energy Information Administration (2011), ISBN 2025869592.

[4] S. A. Montzka, E. J. Dlugokencky, and J. H. Butler, Nature **476**, 43 (2011).

[5] *World energy outlook 2011. Executive summary*, International Energy Agency (IEA) (2011).

[6] *Renewables 2011. Global status report*, REN21 Secretariat and Deutsche Gesellschaft für Internationale Zusammenarbeit (GIZ) GmbH (2011).

[7] *Solar generation 6. Solar photovoltaic electricity empowering the world*, European Photovoltaic Industry Association (EPIA); Greenpeace International (2011).

[8] N. Espinosa, M. Hösel, D. Angmo, and F. C. Krebs, Energy & Environmental Science **5**, 5117 (2012).

[9] J. J. Siddiqui, J. D. Phillips, K. Leedy, and B. Bayraktaroglu, IEEE Transactions on Electron Devices **59**, 1488 (2012).

[10] J.-S. Park, Journal of Electroceramics **28**, 74 (2012).

[11] S. Masuda, K. Kitamura, Y. Okumura, S. Miyatake, H. Tabata, and T. Kawai, Journal of Applied Physics **93**, 1624 (2003).

[12] W. E. Bowen, W. Wang, and J. D. Phillips, IEEE Electron Device Letters **30**, 1314 (2009).

[13] E. M. C. Fortunato, P. M. C. Barquinha, A. C. M. B. G. Pimentel, A. M. F. Goncalves, A. J. S. Marques, L. M. N. Pereira, and R. F. P. Martins, Advanced Materials **17**, 590 (2005).

[14] B. P. Jelle, A. Hynd, A. Gustavsen, D. Arasteh, H. Goudey, and R. Hart, Solar Energy Materials and Solar Cells **96**, 1 (2012).

[15] R. Baetens, B. P. Jelle, and A. Gustavsen, Solar Energy Materials and Solar Cells **94**, 87 (2010).

[16] C. Granqvist, A. Azens, A. Hjelm, L. Kullman, G. Niklasson, D. Rönnow, M. Strømme Mattsson, M. Veszelei, and G. Vaivars, Solar Energy **63**, 199 (1998).

[17] C. G. Granqvist, Solar Energy Materials and Solar Cells **99**, 1 (2012).

[18] C. Klingshirn, Chemphyschem : A European Journal of Chemical Physics and Physical Chemistry **8**, 782 (2007).

[19] U. Ozgur, Y. I. Alivov, C. Liu, A. Teke, M. A. Reshchikov, S. Dogan, V. Avrutin, S.-J. Cho, and H. Morkoc, Journal of Applied Physics **98**, 041301 (2005).

[20] A. Janotti and C. G. van de Walle, Reports on Progress in Physics **72**, 126501 (2009).

[21] A. Ohtomo and A. Tsukazaki, Semiconductor Science and Technology **20**, S1 (2005).

[22] T. Minami, Semiconductor Science and Technology **20**, S35 (2005).

[23] B. Parida, S. Iniyan, and R. Goic, Renewable and Sustainable Energy Reviews **15**, 1625 (2011).

[24] A. Shah, P. Torres, R. Tscharner, N. Wyrsch, and H. Keppner, Science **285**, 692 (1999).

[25] A. Luque, Journal of Applied Physics **110**, 031301 (2011).

[26] K. Söderström, G. Bugnon, F.-J. Haug, S. Nicolay, and C. Ballif, Solar Energy Materials and Solar Cells **101**, 193 (2012).

[27] J. Escarré, K. Söderström, M. Despeisse, S. Nicolay, C. Battaglia, G. Bugnon, L. Ding, F. Meillaud, F.-J. Haug, and C. Ballif, Solar Energy Materials and Solar Cells **98**, 185 (2012).

[28] Y. H. Hu, H. J. Xu, H. Gao, Y. C. Chen, L. F. Wang, and W. H. Jiang, Journal of Physics: Conference Series **276**, 012167 (2011).

[29] X.-L. Chen, F. Wang, X.-H. Geng, D.-K. Zhang, C.-C. Wei, X.-D. Zhang, and Y. Zhao, Applied Surface Science **258**, 4092 (2012).

[30] W. Beyer, J. Hüpkes, and H. Stiebig, Thin Solid Films **516**, 147 (2007).

[31] D. L. Staebler and C. R. Wronski, Applied Physics Letters **31**, 292 (1977).

[32] K. Yamamoto, A. Nakajima, M. Yoshimi, T. Sawada, S. Fukuda, T. Suezaki, M. Ichikawa, Y. Koi, M. Goto, T. Meguro, T. Matsuda, M. Kondo, T. Sasaki, and Y. Tawada, Solar Energy **77**, 939 (2004).

[33] T. Sontheimer, C. Becker, U. Bloeck, S. Gall, and B. Rech, Applied Physics Letters **95**, 101902 (2009).

[34] F. Ruske, M. Roczen, K. Lee, M. Wimmer, S. Gall, J. Hupkes, D. Hrunski, and B. Rech, Journal of Applied Physics **107**, 013708 (2010).

[35] M. A. Green, P. Basore, N. Chang, D. Clugston, R. Egan, R. Evans, D. Hogg, S. Jarnason, M. Keevers, P. Lasswell, J. O'Sullivan, U. Schubert, A. Turner, S. Wenham, and T. Young, Solar Energy **77**, 857 (2004).

[36] V. Avrutin, N. Izyumskaya, and H. Morkoc, Superlattices and Microstructures **49**, 337 (2011).

[37] U. Rau and M. Schmidt, Thin Solid Films **387**, 141 (2001).

[38] P. Jackson, D. Hariskos, E. Lotter, S. Paetel, R. Wuerz, R. Menner, W. Wischmann, and M. Powalla, Progress in Photovoltaics: Research and Applications **19**, 894 (2011).

[39] A. Niemegeers, M. Burgelman, and A. De Vos, Applied Physics Letters **67**, 843 (1995).

[40] A. Hultqvist, C. Platzer-Björkman, E. Coronel, and M. Edoff, Solar Energy Materials and Solar Cells **95**, 497 (2011).

[41] A. Hultqvist, C. Platzer-Björkman, U. Zimmermann, M. Edoff, and T. Törndahl, Progress in Photovoltaics: Research and Applications 1–9 (2011).

[42] A. B. Djurisić, A. M. C. Ng, and X. Y. Chen, Progress in Quantum Electronics **34**, 191 (2010).

[43] I. Gonzalez-Valls and M. Lira-Cantu, Energy & Environmental Science **2**, 19 (2009).

[44] S. Tohoda, D. Fujishima, A. Yano, A. Ogane, K. Matsuyama, Y. Nakamura, N. Tokuoka, H. Kanno, T. Kinoshita, H. Sakata, M. Taguchi, and E. Maruyama, Journal of Non-Crystalline Solids 4–7 (2012).

[45] K. Ellmer, A. Klein, and B. Rech, *Transparent Conductive Zinc Oxide*, Springer (2008), ISBN 978-3-540-73611-0.

[46] A. Mang, K. Reimann, and S. Rübenacke, Solid State Communications **94**, 251 (1995).

[47] P. Erhart, K. Albe, and A. Klein, Physical Review B **73**, 205203 (2006).

[48] P. Erhart and K. Albe, Physical Review B **73**, 115207 (2006).

[49] C. G. van de Walle, Physical Review Letters **85**, 1012 (2000).

[50] G. A. Shi, M. Saboktakin, M. Stavola, and S. J. Pearton, Applied Physics Letters **85**, 5601 (2004).

[51] S. Cox, E. Davis, S. Cottrell, P. King, J. Lord, J. Gil, H. Alberto, R. Vilão, J. Piroto Duarte, N. Ayres de Campos, A. Weidinger, R. Lichti, and S. Irvine, Physical Review Letters **86**, 2601 (2001).

[52] Y. B. Zhang, G. K. L. Goh, K. F. Ooi, and S. Tripathy, Journal of Applied Physics **108**, 083716 (2010).

[53] S. B. Zhang, S.-H. H. Wei, and A. Zunger, Physical Review B **63**, 075205 (2001).

[54] E. Burstein, Physical Review **93**, 632 (1954).

[55] J. Y. W. Seto, Journal of Applied Physics **46**, 5247 (1975).

[56] T. I. Kamins, Journal of Applied Physics **42**, 4357 (1971).

[57] J. W. Orton and M. J. Powell, Reports on Progress in Physics **43**, 1263 (1980).

[58] K. Ellmer and R. Mientus, Thin solid films **516**, 4620 (2008).

[59] R. M. Pasquarelli, D. S. Ginley, and R. O'Hayre, Chemical Society reviews **40**, 5406 (2011).

[60] K. Chopra, S. Major, and D. Pandya, Thin Solid Films **102**, 1 (1983).

[61] A. Banerjee and K. Chattopadhyay, Progress in Crystal Growth and Characterization of Materials **50**, 52 (2005).

[62] H. Tanaka, K. Ihara, T. Miyata, H. Sato, and T. Minami, Journal of Vacuum Science & Technology A: Vacuum, Surfaces, and Films **22**, 1757 (2004).

[63] M. Y. Zhang and G. J. Cheng, Applied Physics Letters **99**, 051904 (2011).

[64] H. Agura, A. Suzuki, T. Matsushita, T. Aoki, and M. Okuda, Thin Solid Films **445**, 263 (2003).

[65] J. Hüpkes, H. Zhu, J. Owen, G. Jost, and E. Bunte, Thin Solid Films **520**, 1913 (2012).

[66] J. Muller, B. Rech, J. Springer, and M. Vanecek, Solar Energy **77**, 917 (2004).

[67] T. Minami, H. Sato, H. Nanto, and S. Takata, Japanese Journal of Applied Physics **24**, L781 (1985).

[68] T. Minami, H. Nanto, and S. Takata, Japanese Journal of Applied Physics **23**, L280 (1984).

[69] G. J. Fang, D. J. Li, and B.-L. Yao, Physica Status Solidi (A) **193**, 139 (2002).

[70] K. Ellmer, F. Kudella, R. Mientus, R. Schieck, and S. Fiechter, Thin Solid Films **247**, 15 (1994).

[71] H. Ko, W.-P. Tai, K.-C. Kim, S.-H. Kim, S.-J. Suh, and Y.-S. Kim, Journal of Crystal Growth **277**, 352 (2005).

[72] M. Berginski, J. Hüpkes, W. Reetz, B. Rech, and M. Wuttig, Thin Solid Films **516**, 5836 (2008).

[73] K. Ellmer and T. Welzel, Journal of Materials Research **27**, 765 (2012).

[74] J. Hüpkes, B. Rech, O. Kluth, T. Repmann, B. Zwaygardt, J. Müller, R. Drese, and M. Wuttig, Solar Energy Materials and Solar Cells **90**, 3054 (2006).

[75] R. Cebulla, R. Wendt, and K. Ellmer, Journal of Applied Physics **83**, 1087 (1998).

[76] J. A. Thornton, Journal of Vacuum Science and Technology **11**, 666 (1974).

[77] J. A. Thornton, Journal of Vacuum Science & Technology A: Vacuum, Surfaces, and Films **4**, 3059 (1986).

[78] D. Song, A. G. Aberle, and J. Xia, Applied Surface Science **195**, 291 (2002).

[79] O. Kluth, G. Schöpe, J. Hüpkes, C. Agashe, J. Müller, and B. Rech, Thin Solid Films **442**, 80 (2003).

[80] P. Kelly and R. Arnell, Vacuum **56**, 159 (2000).

[81] A. Anders, Thin Solid Films **518**, 4087 (2010).

[82] B. D. Yao, Y. F. Chan, and N. Wang, Applied Physics Letters **81**, 757 (2002).

[83] H. Zhou, S. Chua, H. Pan, Y. Zhu, T. Osipowicz, W. Liu, K. Zang, Y. Feng, and C. Sow, Journal of Physical Chemistry C **111**, 6405 (2007).

[84] O. Fouad, A. Ismail, Z. Zaki, and R. Mohamed, Applied Catalysis B: Environmental **62**, 144 (2006).

[85] G. Shen, Y. Bando, and C.-J. Lee, The Journal of Physical Chemistry B **109**, 10779 (2005).

[86] H. Liu, S. Chua, and D. Chi, Materials Letters **72**, 71 (2012).

[87] L. Znaidi, Materials Science and Engineering: B **174**, 18 (2010).

[88] T. A. Vijayan, R. Chandramohan, S. Valanarasu, J. Thirumalai, and S. P. Subramanian, Journal of Materials Science **43**, 1776 (2008).

[89] G. J. Exarhos and X.-D. Zhou, Thin Solid Films **515**, 7025 (2007).

[90] J. Hu and R. G. Gordon, Solar Cells **30**, 437 (1991).

[91] J. Hu and R. G. Gordon, Journal of Applied Physics **71**, 880 (1992).

[92] J. Hu and R. G. Gordon, Journal of The Electrochemical Society **139**, 2014 (1992).

[93] J. Hu and R. G. Gordon, Journal of Applied Physics **72**, 5381 (1992).

[94] M. D. Barankin, E. Gonzalez II, A. M. Ladwig, and R. F. Hicks, Solar Energy Materials and Solar Cells **91**, 924 (2007).

[95] W. W. Wenas, A. Yamada, M. Konagai, and K. Takahashi, Japanese Journal of Applied Physics **30**, L441 (1991).

[96] W. W. Wenas, A. Yamada, K. Takahashi, M. Yoshino, and M. Konagai, Journal of Applied Physics **70**, 7119 (1991).

[97] S. Faÿ, U. Kroll, C. Bucher, E. Vallat-Sauvain, and A. Shah, Solar Energy Materials and Solar Cells **86**, 385 (2005).

[98] S. Faÿ, J. Steinhauser, S. Nicolay, and C. Ballif, Thin Solid Films **518**, 2961 (2010).

[99] D. Kim, H. Kim, K. Jang, S. Park, K. Pillai, and J. Yi, Journal of The Electrochemical Society **158**, D191 (2011).

[100] C. Battaglia, C.-M. Hsu, K. Söderström, J. Escarré, F.-J. Haug, M. Charrière, M. Boccard, M. Despeisse, D. T. L. Alexander, M. Cantoni, Y. Cui, and C. Ballif, ACS Nano **6**, 2790 (2012).

[101] S. M. George, Chemical Reviews **110**, 111 (2010).

[102] D.-J. Lee, H.-M. Kim, J.-Y. Kwon, H. Choi, S.-H. Kim, and K.-B. Kim, Advanced Functional Materials **21**, 448 (2011).

[103] J. W. Elam, D. Routkevitch, and S. M. George, Journal of The Electrochemical Society **150**, G339 (2003).

[104] D. Kim, H. Kang, J.-M. Kim, and H. Kim, Applied Surface Science **257**, 3776 (2011).

[105] H. Yuan, B. Luo, D. Yu, A.-j. Cheng, S. A. Campbell, and W. L. Gladfelter, Journal of Vacuum Science & Technology A: Vacuum, Surfaces, and Films **30**, 01A138 (2012).

[106] A. Illiberi, F. Roozeboom, and P. Poodt, ACS Applied Materials & Interfaces **4**, 268 (2012).

[107] A. Nishii, T. Uehara, T. Sakano, Y. Nabetani, T. Akitsu, T. Kato, T. Matsumoto, S. Hagihara, O. Abe, S. Hiraki, and Y. Fujikawa, Physica Status Solidi (A) **203**, 2887 (2006).

[108] T. Shiosaki, Applied Physics Letters **39**, 399 (1981).

[109] J. K. Young and J. K. Hyeong, Materials Letters **21**, 351 (1994).

[110] J. J. Robbins, J. Esteban, C. Fry, and C. A. Wolden, Journal of The Electrochemical Society **150**, C693 (2003).

[111] B. S. Li, Y. C. Liu, Z. Z. Zhi, D. Z. Shen, J. Y. Zhang, Y. M. Lu, X. W. Fan, and X. G. Kong, Journal of Vacuum Science & Technology A: Vacuum, Surfaces, and Films **20**, 1779 (2002).

[112] J. Robbins, J. Harvey, J. Leaf, C. Fry, and C. Wolden, Thin Solid Films **473**, 35 (2005).

[113] R. Groenen, J. Löffler, P. M. Sommeling, J. L. Linden, E. A. G. Hamers, R. E. I. Schropp, and M. C. M. van de Sanden, Thin Solid Films **392**, 226 (2001).

[114] R. Groenen, J. L. Linden, and M. C. M. van de Sanden, Plasma Processes and Polymers **2**, 618 (2005).

[115] B. Li, Y. Liu, D. Shen, J. Zhang, Y. Lu, and X. Fan, Journal of Crystal Growth **249**, 179 (2003).

[116] I. Volintiru, M. Creatore, B. J. Kniknie, C. I. M. A. Spee, and M. C. M. van de Sanden, Journal of Applied Physics **102**, 043709 (2007).

[117] R. Groenen, J. Löffler, J. L. Linden, R. E. I. Schropp, and M. C. M. van de Sanden, Thin Solid Films **492**, 298 (2005).

[118] M. C. M. van de Sanden, R. J. Severens, W. M. M. Kessels, R. F. G. Meulenbroeks, and D. C. Schram, Journal of Applied Physics **84**, 2426 (1998).

[119] M. Creatore, W. M. M. Kessels, Y. Barrell, J. Benedikt, and M. C. M. van de Sanden, Materials Science in Semiconductor Processing **7**, 283 (2004).

[120] B. Hoex, F. J. J. Peeters, M. Creatore, M. A. Blauw, W. M. M. Kessels, and M. C. M. van de Sanden, Journal of Vacuum Science & Technology A: Vacuum, Surfaces, and Films **24**, 1823 (2006).

[121] J. Hong, W. M. M. Kessels, F. J. H. van Assche, H. C. Rieffe, W. J. Soppe, A. W. Weeber, and M. C. M. van de Sanden, Progress in Photovoltaics: Research and Applications **11**, 125 (2003).

[122] B. Hoex, A. J. M. van Erven, R. C. M. Bosch, W. T. M. Stals, M. D. Bijker, P. J. van den Oever, W. M. M. Kessels, and M. C. M. van de Sanden, Progress in Photovoltaics: Research and Applications **13**, 705 (2005).

[123] W. M. M. Kessels, R. J. Severens, A. H. M. Smets, B. A. Korevaar, G. J. Adriaenssens, D. C. Schram, and M. C. M. van de Sanden, Journal of Applied Physics **89**, 2404 (2001).

[124] A. H. M. Smets, W. M. M. Kessels, and M. C. M. van de Sanden, Applied Physics Letters **82**, 1547 (2003).

[125] S. V. Singh, M. Creatore, R. Groenen, K. van Hege, and M. C. M. van de Sanden, Applied Physics Letters **92**, 221502 (2008).

[126] T. Zaharia, P. Kudlacek, M. Creatore, R. Groenen, P. Persoone, and M. C. M. van de Sanden, Diamond and Related Materials **20**, 1266 (2011).

[127] M. F. A. M. van Hest, B. Mitu, D. C. Schram, and M. C. M. van de Sanden, Thin Solid Films **449**, 52 (2004).

[128] I. Volintiru, M. Creatore, and M. C. M. van de Sanden, Journal of Applied Physics **103**, 033704 (2008).

[129] H. Fujiwara and M. Kondo, Physical Review B **71**, 075109 (2005).

[130] G. E. Jellison and F. A. Modine, Applied Physics Letters **69**, 371 (1996).

[131] G. Shi, M. Stavola, S. Pearton, M. Thieme, E. Lavrov, and J. Weber, Physical Review B **72**, 195211 (2005).

[132] J. Robertson, K. Xiong, and S. Clark, Thin Solid Films **496**, 1 (2006).

[133] N. Nickel, Physical Review B **73**, 1 (2006).

Chapter 2

Improved conductivity of aluminum-doped ZnO: the effect of hydrogen diffusion from a hydrogenated amorphous silicon capping layer*

Abstract

Plasma-deposited aluminum-doped ZnO (ZnO:Al) demonstrated a resistivity gradient as function of the film thickness, extending up to about 600 nm. This gradient decreased sharply when the ZnO:Al was capped by a hydrogenated amorphous silicon layer (*a*-Si:H) and subsequently treated according to the solid phase crystallization (SPC) procedure at 600 °C. The resistivity reduced from $1.2{\cdot}10^{-1}$ to $2.6{\cdot}10^{-3}$ $\Omega{\cdot}$cm for a film thickness of 130 nm, while for thicker films the decrease in resistivity was less pronounced, i.e. a factor of 2 for a film thickness of 810 nm. While the carrier concentration was not affected, the mobility significantly increased from 7 to 30 $\mathrm{cm}^2/\mathrm{V{\cdot}s}$ for the thick ZnO:Al layers. This increase was ascribed to the passivation of grain boundary defects by hydrogen, which diffused from the *a*-Si:H towards the ZnO:Al during the SPC procedure. The passivation effect was more pronounced in thinner ZnO:Al layers, characterized by a smaller grain size, due to the presence of large grain boundaries. For thicker films with grain sizes up to 200-300 nm the mobility became progressively less affected by the presence of grain boundaries. Therefore, the hydrogen-induced improvement in conductivity was less significant for the thick ZnO:Al films.

---

*Published as: M. V. Ponomarev, K. Sharma, M. A. Verheijen, M. C. M. van de Sanden, and M. Creatore, Journal of Applied Physics 111, 063715 (2012).

2.1 Introduction

Due to their wide band gap, transparent conductive oxides (TCOs) exhibit a high transparency in the solar spectral range. Therefore, they are used as transparent electrodes in many applications, e.g. in flat panel displays [1, 2], for architectural and automotive glazing [3], in solar thermal applications and in thin film solar cells (SC) [4–6], either silicon- [7, 8] or non-silicon based, such as cadmium telluride [9] and copper indium gallium diselenide [10]. Within the field of thin film silicon-based solar cells, poly-crystalline silicon (poly-Si) receives attention because it couples the potential for high conversion efficiency and lower production costs. One of the approaches towards poly-Si is plasma deposition of amorphous silicon followed by Solid-Phase Crystallization (SPC) [11, 12], which has delivered efficiencies up to 10 % [13, 14]: for example, CSG Solar [15] has achieved an efficiency of 10.4 % by developing a 2.5 μm-thick poly-Si on glass, which was also confirmed by studies reported by Green *et al.* [15]. In this case, the TCO can be applied as front contact and aluminum-doped zinc oxide (ZnO:Al) is often referred to as a valid alternative to e.g. indium tin oxide. The ZnO is considered appealing due to the relatively low cost, high abundance, non-toxicity [16, 17], resistance to H_2 etching [18, 19] and, under specific conditions, surface texturing for light management/trapping.

This manuscript addresses the changes in the electrical properties which the ZnO:Al film undergoes upon SPC treatment of the hydrogenated amorphous silicon (a-Si:H) film deposited on top of the ZnO:Al. As already demonstrated by Lee *et al.* [20], due to the application of a 300 nm - thick a-Si capping layer on top of 700 nm sputtered ZnO:Al, a decrease in resistivity of the TCO layer was measured, i.e. from $(4.3\pm0.1)\cdot10^{-4}$ to $(2.2\pm0.1)\cdot10^{-4}$ $\Omega\cdot$cm after an SPC procedure up to 600. The authors attributed this improvement to the increase in mobility of the charge carriers, which reached a value of 53 $\mathrm{cm}^2/\mathrm{V}\cdot\mathrm{s}$. No further details were reported on the modification of the ZnO:Al layers upon annealing.

The higher mobility was attributed to an improved crystallinity of the ZnO:Al layer, not further supported by any experimental evidence. Later, Ruske *et al.* [21] presented a more extended analysis of the above-mentioned results and reported an increase in mobility as well as in carrier concentration, reaching a value above 10^{20} cm^{-3}, upon annealing. The excellent results in terms of improved conductivity of the ZnO:Al layer upon annealing were attributed to hydrogen diffusion (i.e., as source of additional charge carriers) and to a decrease of defects at grain boundaries. Recently, the same research group improved the electrical properties of thermally degraded ZnO:Al films by means of a capping/annealing procedure [22]. They concluded that a transition from grain boundary scattering to ionized impurity scattering had occurred upon reduction of the defect density at the grain boundaries, after annealing of the films capped with *a*-Si:H.

In the present contribution, a 1 μm-thick *a*-Si:H layer, as typically used in poly-Si based solar cells, was deposited on ZnO:Al layers with a thickness in the range of 100-800 nm. Both layers were synthesized by the expanding thermal plasma (ETP) technique [11, 23]. In particular, following our previous studies [23] on highly conductive ($7 \cdot 10^{-4}$ $\Omega \cdot$cm at a film thickness of 1300 nm) plasma-deposited ZnO:Al layers characterized by a strong gradient in resistivity as a function of the thickness, the present study focuses on the impact of the capping layer and the annealing on the gradient in resistivity of the ZnO:Al thickness series. Therefore, the electrical properties of the pristine ZnO:Al layer prior, as well as after the SPC treatment in the absence/presence of the *a*-Si:H layer, were determined. Moreover, the evaluation of the electrical properties is discussed as a function of the hydrogen diffusion profiles in the poly-Si/ZnO:Al stacks.

This chapter is organized as follows: in Section 2.2 experimental details about sample preparation, post-deposition treatment and analysis techniques are provided. In Section 2.3 the experimental results on the correlation between the electrical and structural properties of the ZnO:Al films are presented and discussed. The gradient in resistivity of the as-deposited films, reduction of the gradient of capped, as well as a deterioration of the uncapped ZnO:Al films upon annealing are reported. Next to the changes in electrical properties, the hydrogen profile in the studied stacks was quantitatively followed by means of ToF-SIMS analysis. The obtained results, i.e. a massive reduction of the resistivity gradient of the capped ZnO:Al layer upon annealing and crystallization of the *a*-Si:H layer into poly-Si, was interpreted also in view of the ZnO:Al morphology development with thickness.

2.2 Experimental details

A remote plasma - enhanced chemical vapor deposition process, i.e. the ETP, was used for both depositions of ZnO:Al films on Corning 7059 glass and *a*-Si:H layers on top of ZnO:Al films. The plasma source was a cascaded arc, which generates a DC discharge between three cathodes and an anode plate at sub-atmospheric pressure (typically P_{arc}=0.3-0.5·10^5 Pa). Due to the pressure difference, the ionized argon expands into the low pressure deposition chamber (typically P_{dep}=30-200 Pa) and dissociates the precursors injected through rings in the plasma jet: at 6.5 cm downstream from the plasma source oxygen was injected; further downstream at 30 cm from the plasma source pre-mixed diethylzinc (DEZ) and trimethylaluminum (TMA) were injected. ZnO:Al films have simultaneously been deposited on two glass (Corning 7059) and one mono-crystalline silicon substrates (<100> n-type Si), placed on a preheated substrate holder located at 50 cm from the plasma source.

In the present work the experimental conditions were chosen to achieve highly conductive ZnO:Al with large surface roughness. In general these conditions are appropriate for applications in solar cells, as earlier described [18, 23]. As shown in Table 2.1, the experimental parameters were kept constant, but the ZnO:Al thickness was in the range of 100 to 800 nm at the deposition rate of 1 nm/s.

On top of the glass substrates covered by ZnO:Al, 1000 nm - thick *a*-Si:H films were grown at 400 °C. In this case the expanding thermal plasma was generated in an argon/hydrogen mixture. As a precursor for *a*-Si:H growth, silane (SiH_4) was used. It was fed into the plasma via an injection ring placed at 5 cm from the plasma source. More details were reported elsewhere [24, 25].

As a next step, an SPC process for 10 hours at 600 °C in vacuum (P=10^{-4} Pa) was performed to fully crystallize *a*-Si:H. The heating rate was programmed as follows: 10 degree/min from room temperature to 400 °C followed by 1 degree/min in the range of 400-600 °C and 10 hours at 600 °C. Afterwards, the power of the heater was switched off to let the samples cool down to room temperature.

The electrical properties were measured using a Jandel universal four-point probe with a cylindrical 25mm probe head, following the approach of Ruske *et al.* [21] A VEECO Dektak 8 step-profiler was used to determine the thickness of the deposited films. Hall measurements were performed by means of a Phystech RH 2010 to determine the carrier concentration and mobility. A small preparation procedure was carried out to make good contacts with the capped ZnO:Al layer. On each corner of a 10x10 mm^2 poly-Si/ZnO:Al/glass samples ion beam etching of poly-Si layer was performed with a spot size of 2x1 mm^2. An argon-ion gun at 3000 eV and 3.85 μA was used for that, leading to an etch rate of ~0.13 nm/s.

Surface morphology characterization was performed on an NT-MDT Solver P47 Atomic Force Microscope (AFM) in a semi-contact mode with a scan size of 2x2 μm^2. In addition, cross-sectional Transmission Electron Microscopy (TEM)

Table 2.1. Summary of the experimental settings. Type of film and varied experimental conditions are indicated.

Experimental parameter	Type of film	
	ZnO:Al	*a*-Si:H
G_{Ar}, sccm	1000	3300
G_{H_2}, sccm	-	600
I_{Arc}, A	50	45
$P_{Arc} \cdot 10^5$, Pa	0.41	0.32
P_{Dep}, Pa	170	15
G_{DEZ}, g/h	3.5	-
G_{TMA}, g/h	0.2	-
G_{O_2}, sccm	100	-
G_{SiH_4}, sccm	-	600
$T_{sub.}$, ^{0}C	200	400
Thickness, nm	100-800	1000

(FEI Tecnai F30ST Transmission electron microscope operated at 300 kV) and Scanning Electron Microscopy (SEM) (Jeol JSM-7500 FA) analyses were used to visualize the ZnO:Al grain development.

Rutherford Backscattering Spectroscopy (RBS) was employed to obtain quantitative information about the composition of the ZnO:Al films. In particular, RBS was used to measure zinc, oxygen and aluminum content in the ZnO:Al films, needed for the calibration of data provided by the Time-of-Flight Secondary Ion Mass Spectrometry (ToF-SIMS) measurements. Hydrogen content was measured by means of Elastic Recoil Detection analysis (ERD). Both RBS and ERD measurements were performed using 2 MeV He^+ ions produced by an HVE 3.5 MV singletron. In addition, the hydrogen concentration in *a*-Si:H films on c-Si substrate was calculated from the 640 cm^{-1} wagging mode in the spectra obtained by the Fourier Transform Infrared (FTIR) technique (Bruker Tensor 27), as described elsewhere[26, 27].

The ToF-SIMS analysis on the ZnO:Al capped with SPC *a*-Si:H was performed to determine the elemental composition as a function of depth by means of a IONTOF ToF-SIMS IV instrument, using 25 keV Bi^+ ions from a 3-lens in both positive and negative modes. By calibrating these measurements with results determined from the ERD measurements, the hydrogen concentration in poly-Si on ZnO:Al was determined.

X-Ray Diffraction (XRD) measurements combined with *in situ* annealing at 600 °C were performed on a Philips MPD Control PW3710 X-Ray diffractometer to study the crystallization behavior of *a*-Si:H in more detail.

2.3 Results

The resistivity trends as a function of the thickness for the as-deposited and annealed ZnO:Al films in the absence/presence of a capping layer are shown in Figure 2.1a. In agreement with the previous work [23], a gradient in resistivity as function of the thickness was observed for the as-deposited ZnO:Al layers (Figure 2.1a, square symbol). This result was attributed to structural changes occurring during the growth of the poly-crystalline ZnO:Al layer, namely, a pyramid-like growth development of the ZnO:Al grains [23]. This type of growth is characterized by an increase in grain size and, consequently, a reduction in the density of grain boundaries and charge trapping centers, leading to an enhanced mobility [23]. At the same time, the ZnO:Al, which was capped with *a*-Si:H and had received an SPC treatment (Figure 2.1a, circle symbol), exhibited a decrease in resistivity. In particular, the effect had a major impact on the thinner films, leading to a significant decrease of resistivity and a suppression of the resistivity gradient. On the contrary, annealing the uncapped ZnO:Al at SPC conditions in vacuum deteriorated its electrical properties (Figure 2.1a, triangle symbol), in agreement with Minami *et al.*[28], and the effect was more pronounced for larger ZnO:Al thickness values.

The deterioration of the electrical properties of the uncapped ZnO:Al can be related to the oxygen present at the grain boundaries. One possible explanation is the formation of Al_2O_3 at the grain boundaries, based on the presence of residual oxygen during vacuum annealing. This oxidation is thermodynamically favored due to its high formation enthalpy4. The increase in resistivity clearly correlates with measurements of the VIS-NIR (650-1700 nm) transmittance of the uncapped ZnO:Al films, which significantly increased after annealing under SPC conditions, as shown in the inset of Figure 2.1b for the 810 nm - thick ZnO:Al sample. The effect is in agreement with observations of Lee *et al.* [20] and suggests that the absorption by free charge carriers in the near-infrared is considerably reduced.

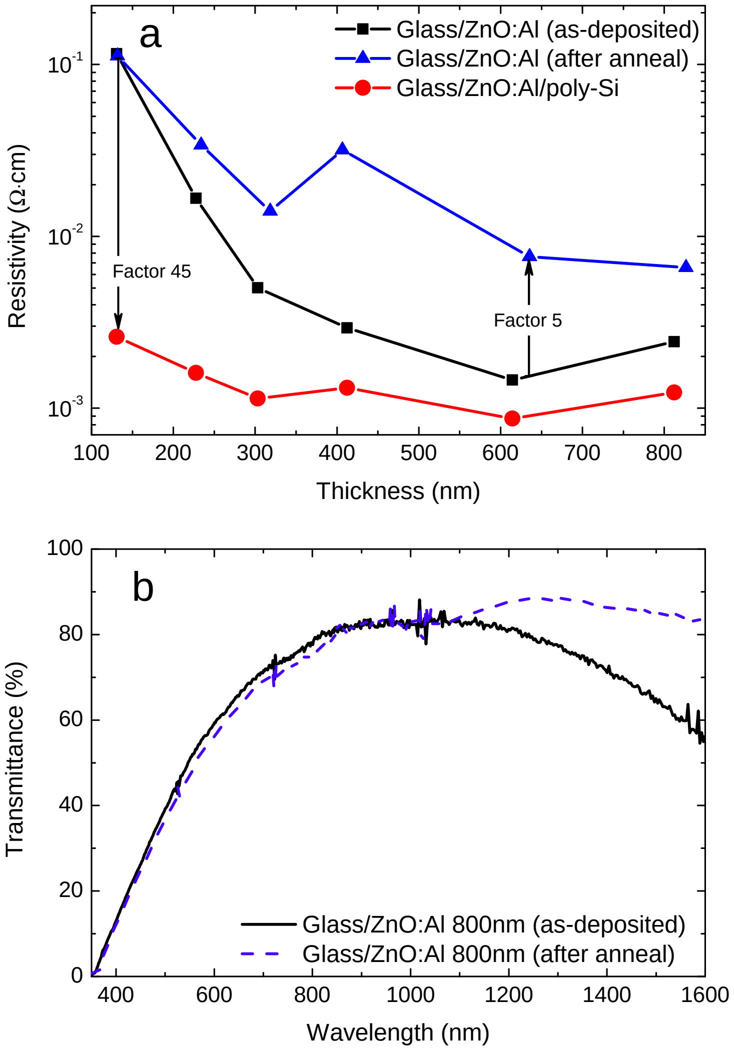

Figure 2.1. *a* - Changes in resistivity of the ZnO:Al layer as function of the thickness upon anneal in the absence/presence of a capping a-Si:H layer; *b* - Changes in the straight-through transmittance for the 810 nm - thick ZnO:Al film before and after SPC treatment.

Therefore, it can be concluded that a decrease in doping efficiency can be caused by the formation of Al_2O_3, which acts as neutral impurity scattering center.

Another reason for the deterioration effect observed in Figure 2.1a is based on the considerations reported by Minami *et al.* [28]: oxygen chemisorbed at the grain boundaries can capture free electrons from the bulk of the grain, creating extrinsic interface states. There are several factors related to the grain boundaries that can reduce the mobility, namely, fairly high densities of interface states which trap free carriers from the bulk of the grains, scattering of free carriers induced by the inherent disorder and the presence of trapped charges [29]. According to the grain boundary carrier-trapping model [30–32], oxygen adsorbed at the grain boundaries results in an additional interface charge, which gives rise to band-bending (the energy difference between the conduction band edge at the grain boundary and in the bulk of the grain) in the bulk of the grain and to the creation of potential energy barriers [29]. These grain boundary barriers hinder the motion of free carriers from one grain to another by scattering them back to the bulk of the grain, thereby their inter-grain mobility is reduced and overall the film resistivity increases.

Next to the study of the uncapped layers, the properties of ZnO:Al layers capped with *a*-Si:H were evaluated. As pointed out by Ruske *et al.* [21], the improvement of the electrical properties of capped ZnO:Al was caused by the hydrogen available in the *a*-Si:H capping layer before the SPC procedure, although an additional source of hydrogen was present in their sample, i.e. a SiN_x:H layer between the glass substrate and the ZnO:Al layer.

On the basis of the FTIR analysis of the present experiments, the hydrogen concentration in the as-deposited *a*-Si:H was equal to $(3.6 \pm 0.3) \cdot 10^{21}$ at/cm^3. The ERD-measured hydrogen concentration in the as-deposited ZnO:Al layer was $(2.7 \pm 0.3) \cdot 10^{20}$ at/cm^3, which is one order of magnitude lower than in *a*-Si:H. Therefore, during the SPC process of *a*-Si:H, it is expected that hydrogen diffuses into the ZnO:Al layer, as well escapes towards the ambient [33] (i.e., the oven). Within the ZnO:Al layer, hydrogen can reduce the grain boundary defects that limit the film conductivity. It also forms a strong bond with oxygen, providing a powerful driving force for its incorporation in the ZnO crystal [34]. According to Van de Walle [34], hydrogen in ZnO appears exclusively in the positive charge state, i.e. it always acts as a donor causing an increase in carrier concentration. Therefore, it tends to reduce the energy barriers at the grain boundaries, thus being the main reason for the improved electrical properties [35], in agreement with Ruske *et al.* [21] Other mechanisms, such as reduction of point defects and activation of the Al from Al-oxide phase [36, 37] are also possible and should not be disregarded. For example, Kim *et al.* [37] showed activation of Al dopants through deoxidation of Al-oxides, after annealing ZnO:Al films at 900 °C for 3 minutes.

However, as shown in Figure 2.1a, the hydrogen impact on the electrical properties is dependent on the thickness of the ZnO:Al film. For the 130 nm-thick ZnO:Al film, the resistivity improved by a factor 45 (to $2.6 \cdot 10^{-3}$ Ω·cm), while for the 810 nm - thick layer the improvement was only a factor of 2 (to $1.2 \cdot 10^{-3}$ Ω·cm). This is because of the large influence of the grain boundary states on the lateral film resistivity/mobility, as already concluded by Volintiru *et al.* [38] A similar effect was observed by Wimmer *et al.* [22] for 900 nm-thick ZnO:Al: capping and annealing of as-deposited film resulted in a factor of 2 improvement in resistivity ($\sim 2.4 \cdot 10^{-4}$ Ω·cm), while this latter was increasing by more than a factor of 100 for the thermally degraded films with the lowest carrier concentration and mobility.

The carrier concentration measured in the capped ZnO:Al was about $3 \cdot 10^{20}$ cm^{-3} and the mobility was around 30 cm^2/V·s for the 600 nm - thick ZnO:Al layer and about the same value for the 200 nm - thick film. The carrier concentration is in agreement with the value associated to the pristine ZnO:Al ($2 \cdot 10^{20}$ cm^{-3}) and the mobility significantly increased from the as-deposited state (7 cm^2/V·s at 600 nm). This result also points out that the grain boundaries are passivated by hydrogen. Moreover, it agrees well with the observations of Ruske *et al.* [21], who reported a significant increase of the mobility. The same research group also showed a faster poly-crystalline silicon nuclei development on ZnO:Al films, as compared to SiN$_x$:H films [39], in agreement with *in situ* crystallization study of this work (data not shown here). As inferred from *in situ* XRD measurements [40], the formation of nuclei in the *a*-Si:H capping layer occurred already after 60 minutes of annealing at 600 °C in the case of 810 nm– thick ZnO:Al, while, in the case of *a*-Si:H deposited on glass, the nucleation started after 180 minutes.

To understand the effect of annealing in more detail, the in-depth hydrogen distribution was studied in the poly-Si/ZnO:Al stacks. In Figure 2.2 ToF-SIMS depth profiles are presented for the ZnO:Al capped with SPC *a*-Si:H samples with 810 nm - thick (Figure 2.2a) and 130 nm - thick (Figure 2.2b) ZnO:Al. For simplicity, only the hydrogen, silicon, zinc oxide and silicon dioxide profiles are shown. The Si signal intensity was constant and equal in both samples, pointing out similar properties of the poly-Si capping layer in both cases. The poly-Si/ZnO:Al and ZnO:Al/glass interfaces for both samples are for sake of simplicity defined by means of two vertical lines in Figure 2.2. Due to the larger roughness of the 800 nm-thick ZnO:Al layer as compared to the 130 nm layer (r.m.s. values obtained from AFM measurements: 40 vs. 15 nm, respectively), the poly-Si/ZnO:Al interface region is found to be broader for the thicker ZnO:Al layer. Therefore, it appeared earlier on the timescale of the ToF-SIMS analysis (Figure 2.2a) as compared to the sample with a thinner ZnO:Al layer (Figure 2.2b). At the same time, the hydrogen profiles are significantly different. In order to extract quantitative information, the hydrogen depth profiles were calibrated by means of the ERD analysis, and the results are shown on the right axis in Figure 2.2. The hydrogen in the poly-Si on 130 nm - thick ZnO:Al is below the detection limit (i.e. 1-2$\cdot 10^{19}$ at/cm^3) almost through the whole poly-Si layer and abruptly rises just at the interface with the ZnO:Al film to 10^{21} at/cm^3. For the sample with 810 nm - thick ZnO:Al the hydrogen concentration increases gradually from the poly-Si layer to 10^{21} at/cm^3 at the interface with the ZnO:Al layer and up to $3\cdot 10^{21}$ at/cm^3 half way the ZnO:Al layer thickness. The conclusion is that for both ZnO:Al films the hydrogen concentration is significantly higher when compared to the one in the pristine ZnO:Al film (also shown in Figure 2.2). This implies that hydrogen diffused from the *a*-Si:H layer into the ZnO:Al and was effectively stored after the SPC process.

The reason why the hydrogen concentration is higher for the thicker ZnO:Al film may be related to the layer structure providing a larger grain-boundary surface available for atomic hydrogen to be trapped and stored. This hypothesis is supported by the fact that the ZnO:Al layers were grown under the same experimental conditions and presented the same doping concentration (0.37 % Al in 130 nm ZnO:Al and 0.36 % Al in 810 nm ZnO:Al, as measured by ToF-SIMS and calibrated by means of the RBS results). Therefore, cross-sectional TEM analyses were carried out to get an insight into the ZnO:Al growth development (Figure 2.3, cross-sectional High Angle Annular Dark Field - Scanning Transmission Electron Microscopy (HAADF-STEM)).

At early growth stages, below 100 nm of film thickness, there was a layer of very densely packed crystallites extending over few tens of nm. During film growth, some grain orientations were suppressed, while others continued to develop either vertically and/or laterally. As observed in Figure 2.3, this growth was accompanied by the inclusion of large voids extending up to few hundred nanometers in height developing at 100-600 nm from the substrate surface. Then, the developed

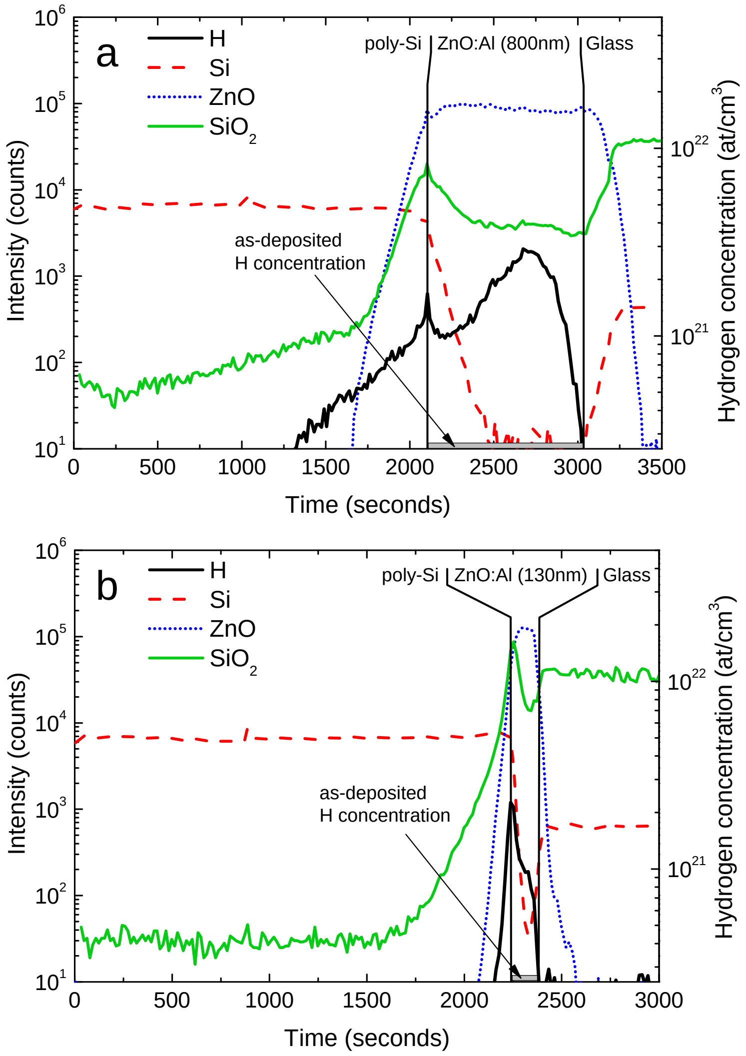

Figure 2.2. ToF-SIMS profiles of poly-Si/ZnO:Al/glass samples: *a* - $d_{ZnO:Al}$=810 nm, *b* - $d_{ZnO:Al}$=130 nm. The local maximum in the hydrogen profile at the poly-Si/ZnO:Al interface is accompanied by an enhancement in count rate for several other signals, i.e. F-, S- (both are not shown here) and SiO$_2$. This result could be morphology-related (i.e. the surface roughness of the ZnO:Al layer can induce an artifact in the ToF-SIMS profile, especially in the case of the thickest sample) and possibly dependent from an intermixing effect during the ToF-SIMS analysis.

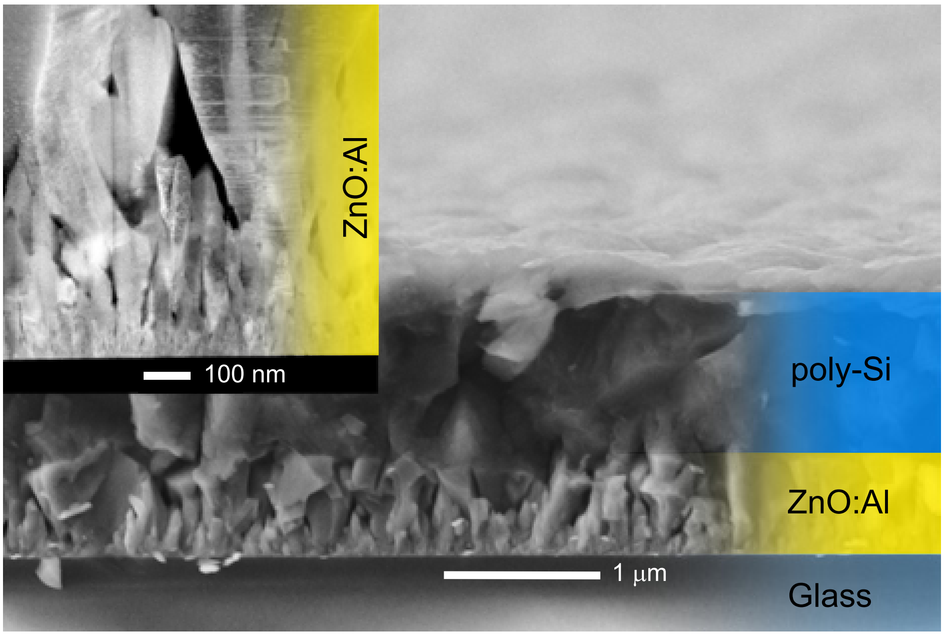

Figure 2.3. Scanning Electron Microscopy image of poly-Si (1000nm) on ZnO:Al (810nm)/glass. Inset: Cross-sectional HAADF-STEM image of ZnO:Al film on glass. Dark areas represent voids in the layer.

grains coalesced at 600-700 nm height and formed a dense matrix with no further inclusion of voids. This is important for the lateral current propagation, especially within thinner layers of ZnO:Al, where the total area of the grain boundaries is higher due to the smaller crystal size. If defects at the grain boundaries are not passivated, the grain boundary scattering together with the presence of voids can significantly limit the lateral conductivity. For the ZnO:Al films grown under these conditions, the carrier concentration was about $2{\cdot}10^{20}$ cm^{-3}, which is considered to be a rather high doping level. According to the grain boundary carrier-trapping model [29–31], the charge carriers can be trapped at the grain boundaries, producing a charged grain boundary surrounded by a space-charge region. The resistivity of this space-charge region can limit the conductivity of the sample. With an increase in doping concentration the barrier height decreases and the space-charge region gets narrower. Because there is an exponential dependence of the grain boundary resistivity on the barrier height [30],this resistivity will decrease faster than the one of the grains. Therefore, at heavy doping levels, grain boundaries do not limit the conductivity anymore [41], so the mobility becomes independent from the grain size. However, from Figure 2.1a the resistivity of the as-deposited samples is thickness-dependent, or, since the grain size is increasing with thickness, grain size - dependent. Thus, the potential at the grain boundaries has to be considered, as influencing the mobility of the charge carriers.

As extensively discussed in our previously published work [23], the lateral conductivity is effectively limited by the relatively high grain boundary density at the early stages of ZnO:Al growth. With an increase in film thickness, the lateral conductivity becomes gradually less affected by the grain boundary scattering and more by the ionized impurity scattering phenomena, as the grains develop in size. At intermediate thicknesses, i.e. where large voids develop, the percolation path for the charge carriers becomes longer and the scattering mechanisms in the bulk ZnO:Al become relevant. In agreement with Wimmer *et al.* [22], the impact of hydrogen in improving the ZnO:Al conductivity is attributed to the reduction of the defect density at the grain boundaries of the ZnO:Al layer. This effect is larger in the case of low ZnO:Al film thickness, because the mobility is limited here by the small grain size and, thus, by the grain boundaries. In case of 700-800 nm-thick ZnO:Al films the passivation of grain boundaries still occurs, under the reasonable assumption that the grain boundary defect density is independent from the layer thickness. However, due to the developed larger grain size (200-300 nm), the passivation has a less pronounced effect on the resistivity, as shown in Figure 2.1a. It can be expected that the limited improvement in conductivity for large ZnO:Al thickness values observed in Figure 2.1a is also caused by hydrogen diffusing in the grains, providing additional doping [33, 34, 42, 43] and, thereby, promoting a stronger contribution of the ionized impurity scattering. It has been recently demonstrated [22] that upon annealing of the capped ZnO:Al films the scattering mechanism shifts from grain boundary scattering to ionized impurity scattering.

Furthermore, the local maximum observed in the hydrogen profile in Figure 2.2a at 2700 seconds of the ToF-SIMS analysis can be attributed to the presence of the voids as indicated by the HAADF STEM image in Figure 2.3. The maximum corresponds to a height of about 300 nm of ZnO:Al, where the large pores start to appear allowing atomic hydrogen to readily distribute within the network of voids and be trapped at the large grain boundary surface available.

The structural development of ZnO:Al can also explain the behavior of the uncapped films, where annealing mostly affected films from intermediate to larger thicknesses (Figure 2.1a, triangles). As shown in the HAADF STEM image inset in Figure 2.3, the grain size is quite large at the intermediate thickness (300-600 nm), but there are also large voids at that thickness which allow for easier oxygen diffusion within the ZnO:Al film, adsorbing at the grain boundaries. There, it increases the grain boundary potential for the charge carriers and, in combination with the presence of voids, it induces a longer percolation path for the charge carriers. Therefore, the resistivity at intermediate thicknesses is more affected by annealing. With the further increase in film thickness (600-800 nm), when there are no voids and the grain boundary surface area is reduced, the degradation effect on electrical properties is limited.

2.4 Conclusions

The application of a capping layer of *a*-Si:H on ZnO:Al layers followed by SPC treatment allows for a strong reduction of the gradient in resistivity as function of the thickness of the ZnO:Al layer underneath. A major improvement of the electrical properties was observed in the thinner films: for the 130 nm - thick film, the resistivity is reduced by a factor 45 down to $2.6 \cdot 10^{-3}$ Ω·cm. For the thicker films the effect was less pronounced and mainly caused by the increased mobility of the charge carriers, e.g. from 7 $cm^2/V \cdot s$ to 30 $cm^2/V \cdot s$ for the 600 nm-thick ZnO:Al.

The improvement of the electrical properties was attributed to the passivation of the grain boundaries by hydrogen diffused from the *a*-Si:H capping layer. Although a higher concentration of hydrogen was measured in the stack poly-Si/ZnO:Al layers in the case of the thick ZnO:Al film, the passivation of grain boundaries was found to have a larger impact in the case of thin ZnO:Al films. In this case, charge carrier mobility is strongly limited by the rather small grain size and, therefore, grain boundary effects. On the contrary, at large ZnO:Al thickness values, characterized by a larger grain size and compact structure, the mobility of the charge carriers was less affected by the grain boundaries. Therefore, the passivation had a significantly smaller effect on the resistivity of the thick films. In the case of uncapped ZnO:Al films the annealing mainly deteriorated the areas with the developed network of voids.

In conclusion, highly conductive and thinner front contacts for thin film poly-Si based PV can be obtained upon SPC processing of the *a*-Si:H layer. Hydrogen provides efficient passivation of the trapping states at the grain boundaries, which improves the electrical properties significantly and, if stable in time, provides a novel approach to improve the electrical properties of thin ZnO:Al films.

Acknowledgments The authors would like to thank J.A. Treur, R.H.J. Vervuurt, B.W.H. van de Loo for their assistance in samples preparation and analysis. Also, the authors acknowledge Dr. T. Fernandez Landaluce (TU Eindhoven) for sputtering the poly-Si capping layers during preparation for Hall measurements, ir. J.H.M. Snijders (Philips Innovation Services) for ToF-SIMS measurements, and M.J.F. van de Sande and J.J.A. Zeebregts, M.Sc. (TU Eindhoven) for the extensive technical assistance. This work has been supported within the IRTES project (project number 10007870) by Agentschap NL.

Bibliography

[1] Y. Li, G. Tompa, S. Liang, C. Gorla, Y. Lu, and J. Doyle, Journal of Vacuum Science & Technology A: Vacuum, Surfaces, and Films **15**, 1063 (1997).

[2] C. Agashe, O. Kluth, G. Schöpe, H. Siekmann, J. Hüpkes, and B. Rech, Thin Solid Films **442**, 167 (2003).

[3] C. G. Granqvist, Solar Energy Materials and Solar Cells **91**, 1529 (2007).

[4] S. Jäger, B. Szyszka, J. Szczyrbowski, and G. Bräuer, Surface and Coatings Technology **98**, 1304 (1998).

[5] B. Rech and H. Wagner, Applied Physics A: Materials Science & Processing **69**, 155 (1999).

[6] A. Nemeth, C. Major, M. Fried, Z. Labadi, and I. Barsony, Thin Solid Films **516**, 7016 (2008).

[7] W. M. M. Kessels, M. C. M. van de Sanden, and D. C. Schram, Journal of Vacuum Science & Technology A: Vacuum, Surfaces, and Films **18**, 2153 (2000).

[8] O. Kluth, G. Schöpe, J. Hüpkes, C. Agashe, J. Müller, and B. Rech, Thin Solid Films **442**, 80 (2003).

[9] M. Hädrich, C. Kraft, C. Löffler, H. Metzner, U. Reislöhner, W. Witthuhn, M. Hadrich, C. Loffler, and U. Reislohner, Thin Solid Films **517**, 2282 (2009).

[10] N. Naghavi, D. Abou-Ras, N. Allsop, N. Barreau, S. Bücheler, A. Ennaoui, C.-H. Fischer, C. Guillen, D. Hariskos, J. Herrero, R. Klenk, K. Kushiya, D. Lincot, R. Menner, T. Nakada, C. Platzer-Björkman, S. Spiering, A. Tiwari, and T. Törndahl, Progress in Photovoltaics: Research and Applications **18**, 411 (2010).

[11] A. Illiberi, K. Sharma, M. Creatore, and M. C. M. van de Sanden, Materials Letters **63**, 1817 (2009).

[12] K. Sharma, A. Branca, A. Illiberi, F. D. Tichelaar, M. Creatore, and M. C. M. van de Sanden, Advanced Energy Materials **1**, 401 (2011).

[13] T. Matsuyama, K. Wakisaka, M. Kameda, M. Tanaka, T. Matsuoka, S. Tsuda, S. Nakano, Y. Kishi, and Y. Kuwano, Japanese Journal of Applied Physics **29**, 2327 (1990).

[14] T. Matsuyama, N. Terada, T. Baba, T. Sawada, S. Tsuge, K. Wakisaka, and S. Tsuda, Journal of Non-Crystalline Solids **198-200**, 940 (1996).

[15] M. A. Green, P. Basore, N. Chang, D. Clugston, R. Egan, R. Evans, D. Hogg, S. Jarnason, M. Keevers, P. Lasswell, J. O'Sullivan, U. Schubert, A. Turner, S. Wenham, and T. Young, Solar Energy **77**, 857 (2004).

[16] K. Ellmer, F. Kudella, R. Mientus, R. Schieck, and S. Fiechter, Thin Solid Films **247**, 15 (1994).

[17] J. Muller, B. Rech, J. Springer, and M. Vanecek, Solar Energy **77**, 917 (2004).

[18] J. Löffler, R. Groenen, J. L. Linden, M. C. M. van de Sanden, and R. E. I. Schropp, Thin Solid Films **392**, 315 (2001).

[19] R. Groenen, M. Creatore, and M. C. M. van de Sanden, Applied Surface Science **241**, 321 (2005).

[20] K. Y. Lee, C. Becker, M. Muske, F. Ruske, S. Gall, B. Rech, M. Berginski, and J. Hüpkes, Applied Physics Letters **91**, 241911 (2007).

[21] F. Ruske, M. Roczen, K. Lee, M. Wimmer, S. Gall, J. Hupkes, D. Hrunski, and B. Rech, Journal of Applied Physics **107**, 013708 (2010).

[22] M. Wimmer, F. Ruske, S. Scherf, and B. Rech, Thin Solid Films **520**, 4203 (2011).

[23] I. Volintiru, M. Creatore, B. J. Kniknie, C. I. M. A. Spee, and M. C. M. van de Sanden, Journal of Applied Physics **102**, 043709 (2007).

[24] M. C. M. van de Sanden, R. J. Severens, W. M. M. Kessels, R. F. G. Meulenbroeks, and D. C. Schram, Journal of Applied Physics **84**, 2426 (1998).

[25] W. M. M. Kessels, R. J. Severens, A. H. M. Smets, B. A. Korevaar, G. J. Adriaenssens, D. C. Schram, and M. C. M. van de Sanden, Journal of Applied Physics **89**, 2404 (2001).

[26] R. J. Severens, G. J. H. Brussaard, M. C. M. van de Sanden, and D. C. Schram, Applied Physics Letters **67**, 491 (1995).

[27] A. H. M. Smets, W. M. M. Kessels, and M. C. M. van de Sanden, Applied Physics Letters **82**, 1547 (2003).

[28] T. Minami, Journal of Vacuum Science & Technology A: Vacuum, Surfaces, and Films **17**, 1765 (1999).

[29] J. W. Orton and M. J. Powell, Reports on Progress in Physics **43**, 1263 (1980).

[30] T. I. Kamins, Journal of Applied Physics **42**, 4357 (1971).

[31] J. Y. W. Seto, Journal of Applied Physics **46**, 5247 (1975).

[32] G. Baccarani, B. Ricco, and G. Spadini, Journal of Applied Physics **49**, 5565 (1978).

[33] N. Nickel, Physical Review B **73**, 1 (2006).

[34] C. G. van de Walle, Physical Review Letters **85**, 1012 (2000).

[35] B.-Y. Oh, M.-C. Jeong, D.-S. Kim, W. Lee, and J.-M. Myoung, Journal of Crystal Growth **281**, 475 (2005).

[36] N. Ohta, D. Ohba, S. Sato, Z. Tang, H. Shimizu, and H. Shirai, Thin Solid Films **519**, 6920 (2011).

[37] K.-K. Kim, H. Tampo, J.-O. Song, T.-Y. Seong, S.-J. Park, J.-M. Lee, S.-W. Kim, S. Fujita, and S. Niki, Japanese Journal of Applied Physics **44**, 4776 (2005).

[38] I. Volintiru, M. Creatore, and M. C. M. van de Sanden, Journal of Applied Physics **103**, 033704 (2008).

[39] T. Sontheimer, C. Becker, U. Bloeck, S. Gall, and B. Rech, Applied Physics Letters **95**, 101902 (2009).

[40] K. Sharma, M. A. Verheijen, M. C. M. van de Sanden, and M. Creatore, Journal of Applied Physics **111**, 033508 (2012).

[41] J. Steinhauser, S. Fay, N. Oliveira, E. Vallat-Sauvain, and C. Ballif, Applied Physics Letters **90**, 142107 (2007).

[42] J.-H. Lee, Current Applied Physics **10**, S515 (2010).

[43] B. Oh, M. Jeong, and J. Myoung, Applied Surface Science **253**, 7157 (2007).

Chapter 3

Controlling the resistivity gradient in aluminum-doped zinc oxide grown by plasma-enhanced chemical vapor deposition [*]

Abstract

Aluminum-doped ZnO (ZnO:Al) grown by Chemical Vapor Deposition (CVD) generally exhibit a major drawback, i.e. a gradient in resistivity extending over a large range of film thickness. The present contribution addresses the plasma-enhanced CVD deposition of ZnO:Al layers by focusing on the control of the resistivity gradient and providing the solution towards thin ($\leq$ 300 nm) ZnO:Al layers, exhibiting a resistivity value as low as $4{\cdot}10^{-4}$ $\Omega{\cdot}$cm. The approach chosen in this work is to enable the development of several ZnO:Al crystal orientations at the initial stages of the CVD-growth, which allow the formation of a densely packed structure exhibiting a grain size of 60-80 nm for a film thickness of 95 nm. By providing an insight into the growth of ZnO:Al layers, the present study allows exploring their application into several solar cell technologies.
Controlling the resistivity gradient in aluminum-doped zinc oxide grown by plasma-enhanced chemical vapor deposition

---

[*] Published as: M. V. Ponomarev, M. A. Verheijen, W. Keuning, M. C. M. van de Sanden, and M. Creatore, Journal of Applied Physics 112, 043708 (2012).

3.1 Introduction

Highly conducting (doped) ZnO thin films are being used in diverse applications, such as light-emitting [1] and laser diodes [2], architectural and automotive glazing [3], thin-film transistors [4, 5] and high efficiency thin-film solar cells [6]. This latter makes use of ZnO as transparent conducting oxide (TCO), where a high electrical conductivity in combination with a high optical transmittance and surface texture for an enhanced optical path length [7] are required. N-type doped (Al, Ga, B) ZnO strongly competes in these applications with indium tin oxide (ITO), although ITO shows lower resistivity ($\sim 10^{-4}$ Ω·cm) and higher transmittance [8] than ZnO. Also, ZnO is non-toxic, inexpensive and abundant, which becomes a very important factor, considering the limited supply of indium and the growing demand for ITO large-scale production [9]. Moreover, ZnO is chemically and thermally stable in hydrogen-containing plasmas, which are employed, in the presence of SiH_4 gas, for the deposition of silicon-based thin film p-i-n junctions [10–13]. Therefore, impurity-doped ZnO, e.g. ZnO:Al, is considered to be an attractive candidate to replace ITO [8].

There are several deposition techniques applied to synthesize ZnO, such as sol-gel [14], spray pyrolysis [15], magnetron sputtering [16–18], pulsed laser deposition [19, 20], atomic layer deposition [21, 22] and metal-organic chemical vapor deposition (MO-CVD) [23]. Gas phase-based techniques, as MO-CVD, have also shown potential to grow high quality aluminum-doped ZnO (ZnO:Al) layers [24, 25] at deposition rates as high as $\sim$ 14 nm/s [26] on a large surface area ($>$ 10 cm^2) [25, 26]. In the plasma CVD techniques the overall heat load of the process is lowered, as the substrate temperature is reduced down to the range of 100-200 °C. For example, in the past years, we have shown that the expanding thermal plasma (ETP) leads to good quality ZnO:Al layers deposited up to 1 nm/s with a resistivity of $8{\cdot}10^{-4}$ Ω·cm for 1100 nm film thickness, at a substrate temperature of 200 °C, as reported by Volintiru *et al.* [27]. One of the drawbacks of the CVD processes [27–29], unlike the sputtering approach, is the development of a gradient in resistivity as function of the film thickness, usually present over a large thickness range. In the case of ZnO:Al sputtering, the gradient is typically limited and confined within a small thickness range, i.e. below 200 nm [30]. In the case of the ETP-grown layers, this effect resulted in a factor 50 decrease in resistivity within a thickness range of 70-1300 nm and was related to the development of pyramid-like ZnO:Al grains. As inferred by means of near-IR Spectroscopic Ellipsometry [31], the relatively high in-grain quality was affected by the scattering losses at the grain boundaries present in the case of thin films, characterized by a small grain size (50-75 nm).

In general, the development of high quality doped ZnO CVD layers appears to be intrinsically related to the competition between the nucleation phase (i.e. density and initial grain size) at the early stages of growth and the grain size and crystal orientation/morphology development during the bulk growth. Earlier, an attempt has been performed by Volintiru *et al.* [31] to study the impact of the process parameters (e.g. the process pressure in the deposition chamber) in the ETP with the aim of reducing the gradient in resistivity, described above. The gradient in resistivity was effectively reduced by reducing the process pressure, however the overall resistivity increased up to $\sim 10^{-2}$ Ω·cm in the whole thickness range, because the growth mode shifted from pyramid- to pillar-like, leading to a limited grain size extending through the whole film bulk.

The present contribution introduces and describes a new experimental approach towards the decrease of resistivity gradient in ZnO:Al without compromising the conductivity of the deposited layers. Under specific experimental conditions we enable the development of several ZnO:Al crystal orientations, which allow formation of a rather dense nucleation layer in the early stages of growth. These densely packed crystallites allow for a resistivity as low as $4{\cdot}10^{-4}$ Ω·cm at $\sim$ 300 nm film thickness exhibiting no gradient up to 1100 nm. Using an extensive analytical approach, a full characterization of the deposited ZnO:Al layers was obtained, providing insights into the parameters influencing the ZnO:Al resistivity. The control on the resistivity gradient can definitely allow a more versatile application of the CVD-ZnO layers for the several solar cell technologies, i.e. as transparent conductive oxide in thin film silicon and CIGS solar cells, as well as novel emitter in silicon heterojunction solar cells.

The chapter is organized as follows: section 3.2 describes the experimental details of the deposition technique and the analysis tools. Section 3.3 presents and discusses the resistivity studies on two thickness series obtained at different deposition conditions, under which the resistivity gradient exhibits a different behavior. Subsequently, the differences in resistivity in the two series of ETP-grown ZnO:Al films are directly correlated with: (1) mobility and carrier concentration; and (2) morphological and crystallographic properties. A special emphasis is given to the presence of voids within a certain range of the film thickness, which appeared to be a key parameter controlling occurrence of the resistivity gradient in the ZnO:Al and electrical properties of the bulk layer.

3.2 Experimental details

ZnO:Al films were deposited by means of a remote plasma - enhanced chemical vapor deposition process, i.e. the Expanding Thermal Plasma (ETP) [24, 27, 32]. The technique is based on generating a plasma jet, which expands into a vacuum chamber, dissociates precursors injected downstream and generates reactive species, responsible for film deposition. The plasma source is a cascaded arc unit, where a DC discharge is generated between three cathodes and an anode plate at sub-atmospheric pressure (typically 0.3-0.4$\cdot 10^5$ Pa) in argon. Due to the pressure difference, the ionized argon expands into the low pressure deposition chamber (typically 30-200 Pa) and dissociates precursors injected through rings into the plasma jet: oxygen was injected at 6.5 cm downstream from the plasma source; evaporated and pre-mixed diethylzinc (DEZ) and trimethylaluminum (TMA) were injected further downstream at 30 cm from the plasma source. The growth precursors convectively flow towards the substrate placed at 50 cm to deposit the ZnO:Al film. A 400 nm-thick thermal SiO_2/c-silicon <100> and Corning 7059 glass both of 1 inch^2 size were used as substrates. As shown in Table 3.1, all the experimental parameters were kept constant, but the DEZ flow rate, ranging from 3.2 to 9 g/h.

Table 3.1. Summary of experimental settings.

Type of film	ZnO:Al
G_{Ar}, sccm	1000
I_{Arc}, A	50
$P_{Arc}\cdot 10^5$, Pa	0.41
$P_{Dep.}$, Pa	200
G_{DEZ}, g/h	3.2-9.0
G_{TMA}, g/h	0.2
G_{O_2}, sccm	100
T_{sub}, °C	200
Thickness, nm	50-1100

The electrical properties were measured using a Jandel universal four-point probe with cylindrical 25mm probe head. Additionally, Hall measurements were performed on a Phystech RH 2010 to determine the carrier concentration and mobility.

A VEECO Dektak 8 step-profiler was used to determine the thickness of the deposited films. Cross-sectional Transmission Electron Microscopy (TEM) FEI Tecnai F30ST Transmission electron microscope operated at 300 kV was used to visualize the ZnO:Al grain development at different stages of the growth. Surface morphology imaging was performed on Scanning Electron Microscopy (SEM) Jeol JSM-7500 FA. Additionally, the Root-Mean Square (RMS) surface roughness of the deposited films was calculated from the scans performed on an NT-MDT Solver P47 Atomic Force Microscope (AFM) in a semi-contact mode with a scan size of 2x2 μm^2.

Rutherford Backscattering Spectrometry (RBS) was employed to obtain quantitative information about the composition of ZnO:Al films and to determine the zinc-to-oxygen ratio. RBS measurements were performed using 2 MeV He^+ ions produced by a HVE 3.5 MV singletron. X-ray Photoelectron Spectroscopy (XPS) depth profiling using a Thermo Scientific K-Alpha was performed to independently validate the results of the RBS measurements.

The X-Ray Diffraction (XRD) measurements were performed on a Philips PanAlytical X'pert PRO Material Research Diffractometer to study the texture development of the both ZnO:Al thickness series in more detail. All scans in each of the configurations (Θ-2Θ and Psi-scans) were performed using the same acquisition parameters in order to be able to compare absolute intensities. The optical transmittance of ZnO:Al deposited on glass was measured on Shimadzu UV-3600 spectrophotometer in the wavelength range of 280-2500 nm.

3.3 Results

3.3.1 Evaluation of the electrical properties

In Figure 3.1a the ZnO:Al resistivity is shown as a function of DEZ flow rate. Because the resistivity is a thickness-dependent property as discussed above, the resistivity values are reported for films deposited in the same thickness range, with a limited spread between 260 and 300 nm. It can be concluded that an increase in DEZ flow rate from 3.8 to 9 g/h induces an improvement in the layer conductivity. This improvement may find origin either in a different growth mode of the ZnO:Al layers leading to larger grains and/or in an improved doping efficiency. Therefore, the investigation was limited to two experimental conditions, i.e. G_{DEZ}=5.5 g/h and G_{DEZ}=9 g/h, where the growth and characterization of the ZnO:Al layers is followed as a function of film thickness in the range of 50-1100 nm. For simplicity, designations "*low DEZ*" corresponding to the series deposited at G_{DEZ}=5.5 g/h conditions and "*high DEZ*" corresponding to the one at G_{DEZ}=9 g/h are used throughout the text of this chapter.

In Figure 3.1b the dependence of ZnO:Al resistivity as a function of film thickness is shown. A resistivity gradient is present at *low DEZ* conditions, similarly to what previously reported by Volintiru *et al.* [27]. Because of further process optimization, mainly due to a change in the oxygen/DEZ/TMA flow rates, the layers in Figure 3.1b have a higher quality, than those previously reported by Volintiru *et al.* [27], i.e. lower resistivity at the same thickness ($(3.0\pm0.15)\cdot10^{-4}$ Ω·cm vs. $8.3\cdot10^{-4}$ Ω·cm of Volintiru *et al.* [27], measured for 1100 nm - thick film) and a less steep gradient. One should note here, that resistivity and mobility data were not corrected for the gradient, compared to the previously published work of Volintiru *et al.* [27], where a correction procedure was carried out to quantify the electrical properties of the top ZnO:Al layer. The effective (measured) resistivity of $8.3\cdot10^{-4}$ Ω·cm at 1100 nm achieved by Volintiru *et al.* [27], resulted in a resistivity value of $2.5\cdot10^{-4}$ Ω·cm for the top layer. Similarly, effective resistivity of $3.0\cdot10^{-4}$ Ω·cm measured at 1100 nm for *low DEZ* conditions in this work would be equal to $1.1\cdot10^{-4}$ Ω·cm for the top ZnO:Al layer. The exact correction procedure is reported in more detail by Volintiru *et al.* [27]. At *high DEZ* conditions the resistivity gradient is significantly reduced, and present up to ∼300 nm film thickness (Figure 3.1b). Therefore, the procedure to correct for resistivity gradient is not applicable for *high DEZ* at the thickness above 300 nm, so resistivity of top layer at 1100 nm remains $4.0\cdot10^{-4}$ Ω·cm. Also, at the thickness below 300 nm the resistivity at *high DEZ* is 3-6 times lower than at *low DEZ* conditions reaching the level of $3.9\cdot10^{-4}$ Ω·cm at 300 nm, while for the *low DEZ* series it is achieved only at ∼700 nm. This remarkable difference in the resistivity is further discussed in terms of mobility and carrier concentration of the two series.

In Figure 3.2 the development of mobility and carrier concentration as a function of the film thickness is shown for both *low DEZ* and *high DEZ* conditions. At thickness values below 300 nm the mobility is higher for the *high DEZ* flow. For thicker films its mobility saturates at the level of 20 cm^2/V·s at ∼300 nm and the one associated to *low DEZ* conditions becomes larger up to 33 cm^2/V·s at 1100 nm (Figure 3.2). This difference may point out to a larger grain size when increasing the DEZ flow rate. The carrier concentration at *high DEZ* is larger (7-9) $\cdot10^{20}$ cm^{-3} than the one at *low DEZ* (3-6) $\cdot10^{20}$ cm^{-3} (Figure 3.2).

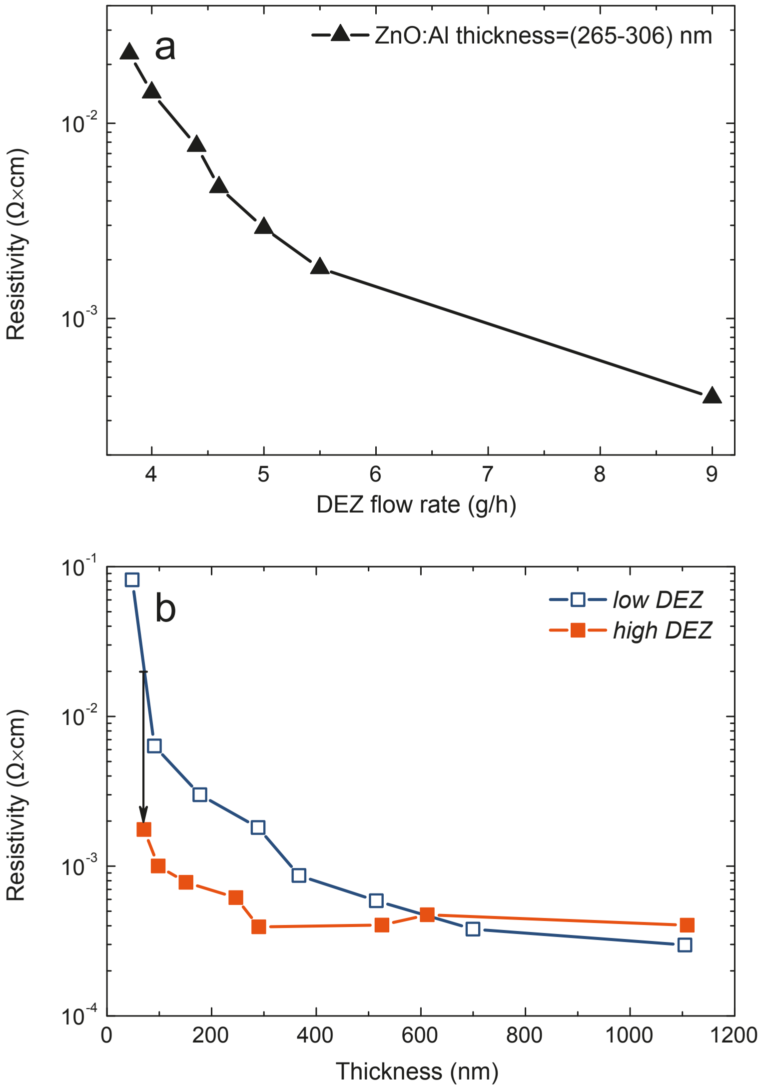

Figure 3.1. a) ZnO:Al resistivity as function of the DEZ flow rate; b) Resistivity development as function of the thickness for two ZnO:Al growth conditions, "*low DEZ*" = 5.5 g/h and "*high DEZ*"= 9.0 g/h.

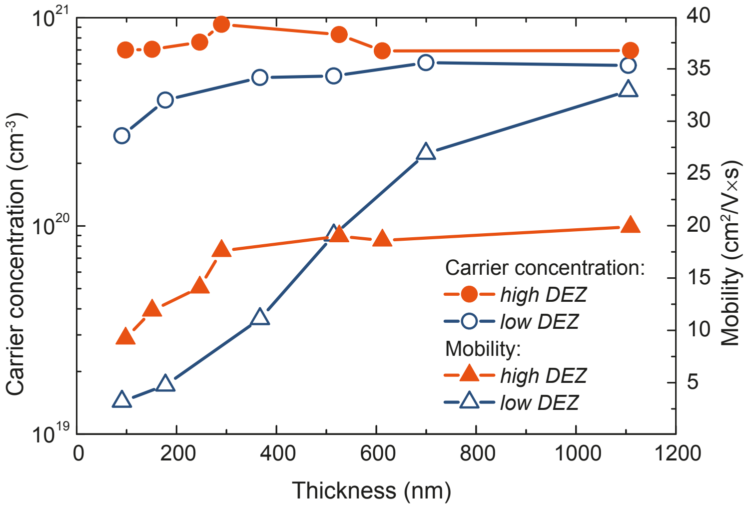

Figure 3.2. Mobility and carrier concentration as a function of layer thickness at *low* and *high DEZ* flow rate.

The error bar associated to this measurement is 10 %, therefore, the difference in carrier concentration between two conditions is considered accurate. This latter is directly related to the atomic concentration of Al in ZnO, measured by RBS: at *low DEZ* conditions the Al concentration is 0.87±0.09 at. %, while at *high DEZ* it is 1.43±0.14 at. %. At *high DEZ* conditions growth flux of $1.9{\cdot}10^{15}$ at/cm^2·s is significantly lower, than the one of *low DEZ*, $5.5{\cdot}10^{15}$ at/cm^2·s, respectively: this comparison suggests an easier incorporation of Al in the ZnO lattice, developed under the lower growth rate, *high DEZ* conditions. Furthermore, the less oxidative environment developed under *high DEZ* conditions (i.e. lower O_2-to-DEZ flow rate ratio) agrees with a higher Al activation efficiency, i.e. 60 % at *high DEZ* vs. 53 % for *low DEZ*. Hydrogen can also act as a dopant [33], however, as inferred from ERD measurements, the hydrogen concentration was $1.5{\cdot}10^{21}$ at/cm^3 in the *high DEZ* sample in comparison to $1.8{\cdot}10^{21}$ at/cm^3 in the *low DEZ* sample, both measured at 1100 nm film thickness. The difference in hydrogen concentrations is quite small and so the effect of hydrogen on ZnO doping can be here neglected. The less oxidative plasma environment in the case of *high DEZ* does not lead to carbon contamination in the deposited layer as RBS measurements point out to stoichiometric ZnO having the same density of $7.5{\cdot}10^{20}$ at/cm^3.

The difference in carrier concentration (Figure 3.2) is also confirmed by the transmittance data shown in Figure 3.3: the *high DEZ* sample exhibited a lower

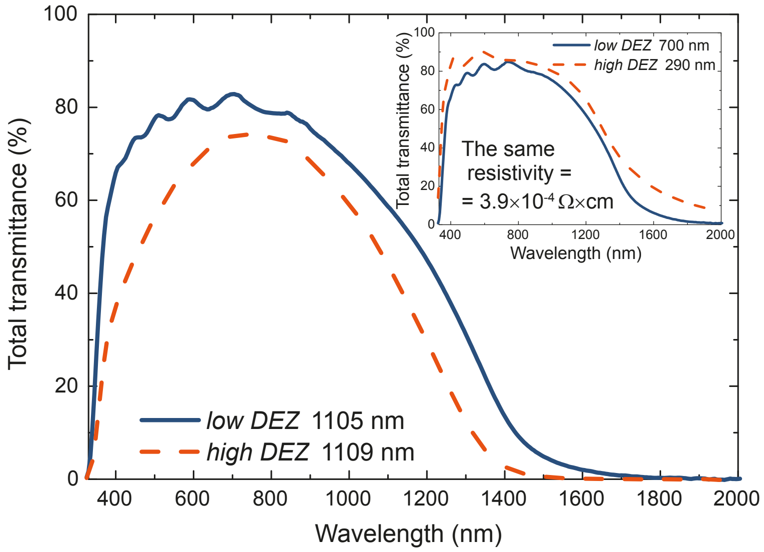

Figure 3.3. Total transmittance of the samples deposited at *low* (solid blue) and *high* (dashed red) *DEZ* flow rates. Inset: total transmittance for two samples with the same resistivity: 700 nm-thick *low DEZ* and 290 nm-thick *high DEZ*.

transmittance the NIR regions, which is attributed to a higher absorbance by free carriers in the film. In agreement with carrier concentration trends in Figure 3.2, the lower NIR transmittance of *high DEZ* samples was observed in the whole range of deposited thicknesses (data not shown here). However, when the thicknesses of 300 nm at *high DEZ* and 700 nm at *low DEZ* are compared, the transmittance of the former is higher (inset of Figure 3.3), which is more favorable for solar cell applications. At *high DEZ*, thicker films exhibit a lower transmittance in the visible range, which is usually attributed to light scattering properties as promoted by surface roughness development. However, the RMS data reported in Figure 3.4 clearly show that the surface roughness of *high DEZ* conditions is generally lower than the one of *low DEZ*, within an error bar of 5 %. The difference in transmittance is further investigated by studying the morphology of the layers.

3.3.2 Structural properties

In Figure 3.5 cross-sectional High Angle Annular Dark Field (HAADF) Scanning TEM (STEM) images of the two 1100 nm - thick ZnO:Al films deposited at low (Figure 3.5a) and high (Figure 3.5b) DEZ conditions are shown. Darker areas

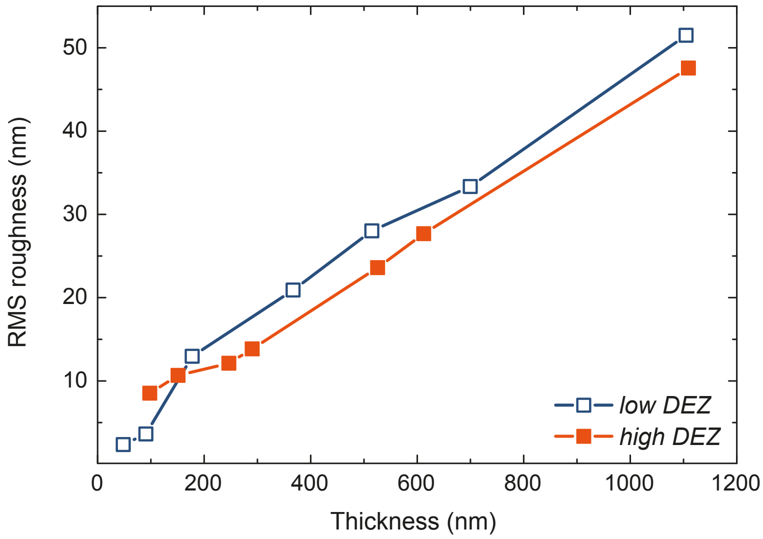

Figure 3.4. Root-mean-square roughness of the samples deposited at *low* (open squares) and *high* (filled squares) *DEZ* flow rates as function of the film thickness.

represent voids in the ZnO:Al layer. The ZnO:Al layer deposited at *low DEZ* conditions exhibits voids in-between grains in the first 500 nm. As the grains develop in size, the voids further extend, but at around 500 nm the grains merge together and larger grain sizes are developed. Thus, from 500 nm film thickness a rather dense structure developed characterized by a grain size above 150 nm (in lateral dimensions). On the contrary, at the *high DEZ* flow conditions the structure shown in Figure 3.5b consists of a rather dense voids-free initial phase, and only from 300-400 nm upwards the voids start to appear in the ZnO:Al layer and propagate up to the top (at 1100 nm). It is therefore argued that these large voids induce multiple scattering and result in light trapping within the ZnO:Al film, causing a reduction in layer VIS transmittance, as shown in Figure 3.2.

Furthermore, the morphology studies allow commenting further on the resistivity trends earlier presented in Figure 3.1b. The presence of voids within the lower thickness range for the *low DEZ* condition appears to correlate with the strong gradient in ZnO:Al resistivity (Figure 3.1b): the voids can, in fact, induce a longer percolation path for electrons to diffuse in the lateral direction. While the grain size is increasing and the layer becomes more compact, the resistivity decreases. At about 400nm the grains coalesce and the layer becomes denser; as the grain size gradually develops, the resistivity further decreases till a plateau is

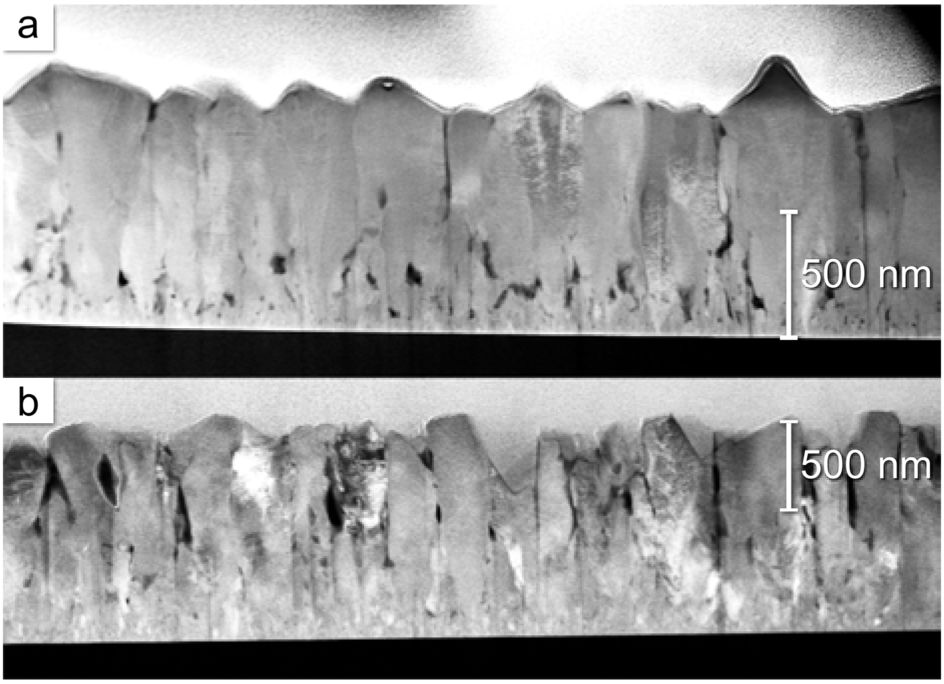

Figure 3.5. Cross-sectional HAADF STEM images : a) *low DEZ* flow conditions, b) *high DEZ* flow conditions. Darker areas represent voids in the material. Note: the images were recorded at different magnification, therefore, scale bars differ from each other.

reached. This correlation between structural development and resistivity at *low DEZ* conditions also agrees with the mobility trend in Figure 3.2, where the mobility of the *low DEZ* series increases in the whole thickness range up to 33 $\mathrm{cm}^2/\mathrm{V{\cdot}s}$ for 1100 nm - thick ZnO:Al. This indicates that the grain boundary scattering becomes less influential on resistivity, while ionized impurity scattering becomes also relevant. The latter factor, according to the grain boundary carrier-trapping model [34, 35], develops with an increase in carrier concentration.

At *high DEZ* conditions there is a small gradient in resistivity at thickness values below 300nm (Figure 3.1b), which agrees with the thickness range necessary to develop a compact ZnO:Al layer with larger grains, according to the TEM image in Figure 3.5b, the strong increase in mobility up to 20 $\mathrm{cm}^2/\mathrm{V{\cdot}s}$ in Figure 3.2. Due to the void-free structure, the mobility of the charge carriers is 2-3 times higher at *high DEZ* conditions causing the resistivity gradient to be strongly reduced and the resistivity values to be lower than the *low DEZ* condition. For thicker films

(> 300 nm) the voids develop in the bulk of the film, therefore the mobility trend saturates, and the resistivity is constant.

In Figure 3.6 top-view SEM images of the samples grown at *low DEZ* (left column) and *high DEZ* (right column) conditions are shown. In agreement with the TEM results, the grain size is larger for the 95 nm - thick ZnO:Al grown at *high DEZ* conditions (right-top image), in comparison with the *low DEZ* conditions (left-top image). This is in agreement with the higher RMS roughness observed in Figure 3.4 for thinner films and supports also the higher mobility and lower resistivity of the ZnO:Al films below 500 nm grown at *high DEZ*. The 1100 nm-thick ZnO:Al deposited at *high DEZ* exhibits voids in-between grains, supporting the previously discussed TEM results in Figure 3.5b.

A larger grain size developed at *high DEZ* conditions in the early stages of growth suggests a preferred growth/development of the grains in the lateral direction. This result can be further investigated by carrying out a crystal growth characterization study with XRD. The absolute peak intensities of XRD spectra obtained in Θ-2Θ geometry are plotted in Figure 3.7 for different DEZ flow rates at constant ZnO:Al thickness (∼300 nm). As mentioned in the experimental part, all Θ-2Θ scans were performed using the same acquisition parameters in order to be able to compare these absolute intensities. As can be seen, already at 300 nm thickness the *low DEZ* flow rates of 4 and 5 g/h are characterized by a strongly developed <002> texture , i.e. a large fraction of the crystals growing with their c-axis aligned to the surface normal. The highest intensity of the <002> peak was observed for the sample deposited at the flow of 5 g/h (Figure 3.7). The diffraction pattern of ZnO:Al grown at *high DEZ* conditions also displays a significant <002> peak. However, an additional set of peaks is present: <101>, <102> and <103>, as shown in the insets in Figure 3.7, implying the co-existence of several crystal growth directions. This observation nicely correlates with the densely packed structure observed by TEM for the low thickness films at *high DEZ* conditions in Figure 3.5b. The difference in absolute height of the <002> peak can either be attributed to differences in the number density of crystals having <002> orientation, or to a difference in the angular spread of this preferential texture. Psi-scans were therefore performed.

The angular distribution of the <002> reflection intensity, most pronounced in the Θ-2Θ scans in Figure 3.7, is displayed in Figure 3.8 for the same set of films. The samples deposited at lower DEZ flow rates (4 and 5 g/h) are characterized by a single peak centered at the surface normal, suggesting a <002>

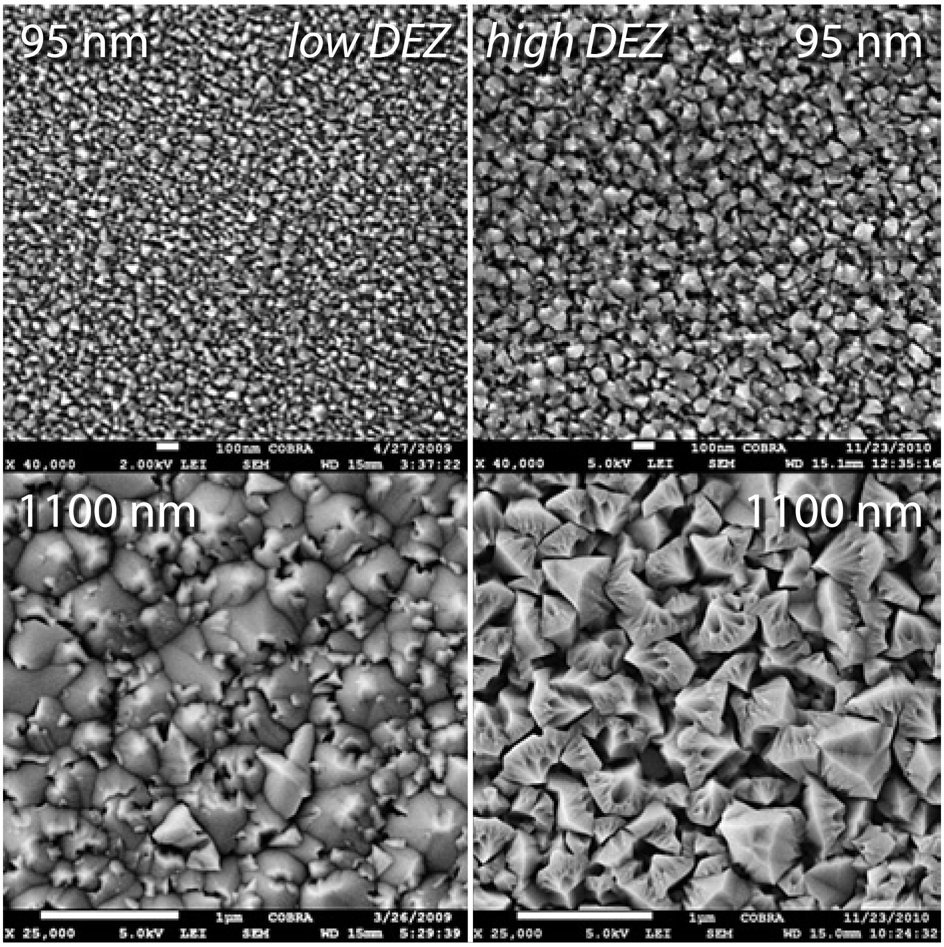

Figure 3.6. Top-view SEM images of the two conditions (left column – *low DEZ* flow, right column – *high DEZ* flow) at different thickness: top row - 95 nm (scale bar is 100 nm), bottom row – 1100 nm (scale bar is 1 μm).

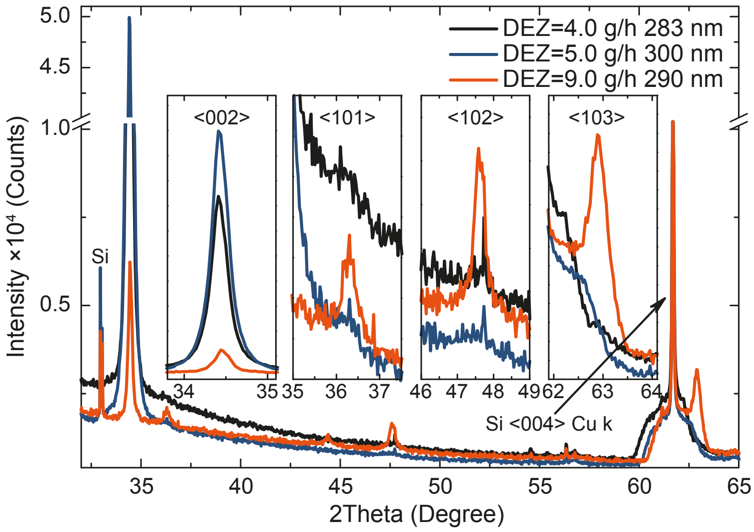

Figure 3.7. XRD signal intensities in 2Θ scan of ZnO:Al films. Development of different texture components with a change of DEZ flow rate at the same film thickness.

preferred growth direction normal to the surface. A 20 % smaller peak width (FWHM=22.7) of the sample deposited at DEZ=5 g/h, compared to the sample deposited at DEZ=4 g/h (FWHM=28.5) indicates that the ZnO:Al deposited at DEZ=5 g/h is more ordered in the vertical direction. However, the *high DEZ* (9 g/h) sample displays a totally different angular distribution: a superposition of several texture contributions can be recognized. Here, an <uvw>texture implies a large fraction of crystals that have a <uvw> zone axis parallel to the surface normal: the *high DEZ* distribution consists of a superposition of peaks around 0°, 30° and 42°, reflecting <002>, <103> and <102> texture contributions, respectively. Here, the peaks at 30° and 42° reflect the off-normal orientation of the <002> lattice planes for crystals that have <103> and <102> crystal orientations running vertically. In addition, all the analyzed samples did not show any preferred in-plane orientation, exhibiting fiber texture in the pole figures (not shown here).

Further development of the texture components at the final thickness of 1100 nm at low and *high DEZ* conditions is shown in the Figure 3.9a. Growing 1100 nm-thick ZnO:Al at *high DEZ* does not lead to the perfect <002> texture: the intensity of <002> peak is lower with additional <101>, <102> and <103> orientations appearing in the spectrum. In the ZnO powder spectrum [36] shown in the Figure 3.9b <002> and <103> contributions occupy only third and fifth

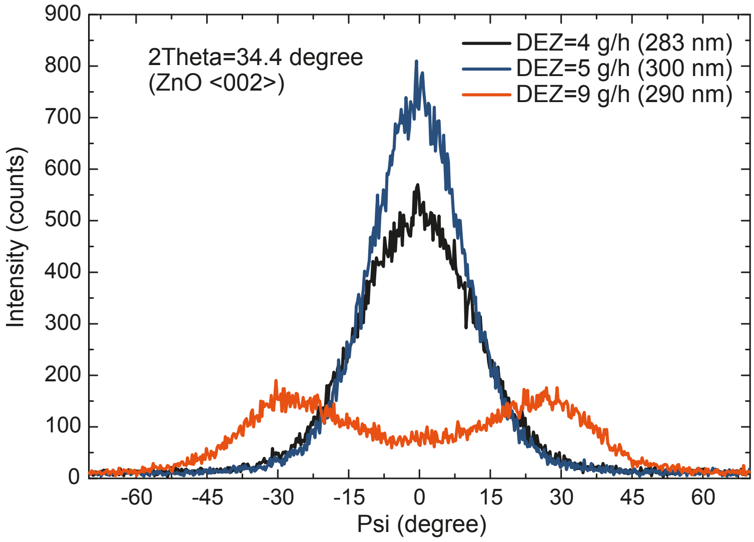

Figure 3.8. XRD angular distribution of <002> reflection intensity in ∼300 nm - thick ZnO:Al deposited at different DEZ conditions. The surface normal is at psi = 0°.

places on the intensity scale with 44 and 28 % of the strongest <101> peak intensity, respectively. In a relative comparison with the powder spectrum *high DEZ* sample still exhibits dominant <002> and <103> components, although being less <002>-textured (factor of 10 lower intensity of <002> peak).

The development of texture can be now related to the presence of voids in the ZnO:Al layer and, eventually, to the electrical properties of ZnO:Al obtained at each of the two discussed conditions. The initial growth (i.e. within 100-150 nm of film thickness) of all investigated conditions starts with the development of several growth directions, which leads to a “mixed texture”, i.e. a dense, voids-free layer. The onset of pronounced growth of the <002> oriented grains in the *low DEZ* samples is accompanied by diagonally expanding side-facets, allowing for voids inclusion in the layer at intermediate thicknesses (150-500 nm). As the <002> texture develops more rapidly at *low DEZ* conditions, voids develop earlier in this layer. A top layer with only <002> grains will yield grains with parallel, vertical grain boundaries, forming a dense layer, as shown by TEM (Figure 3.5). These developed grains lead to the lower resistivity with respect to the thinner films, which are rich of voids, and this morphology development support the presence of the gradient in resistivity with film thickness earlier addressed in Figure 3.1b.

At 9 g/h DEZ, the initial phase of the growth is characterized by several com-

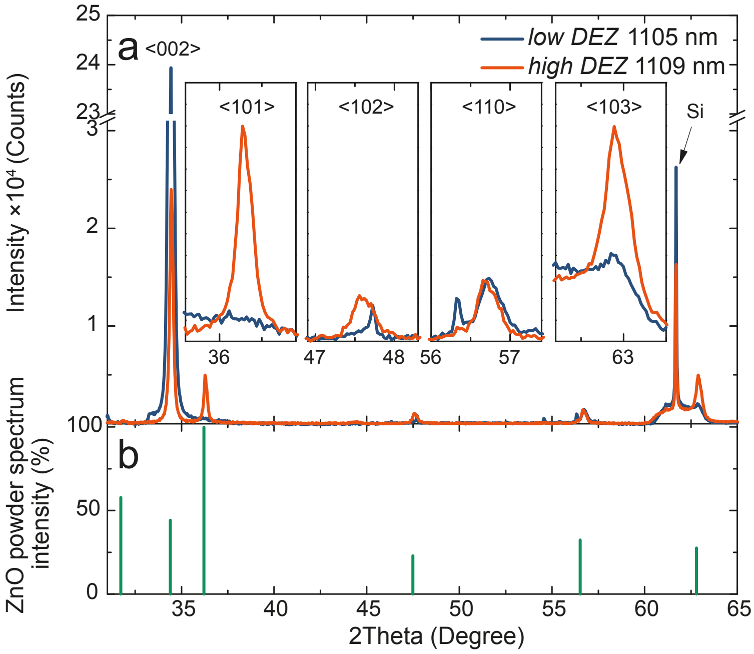

Figure 3.9. XRD signal intensities in Θ-2Θ scan of ZnO:Al films. Development of different texture components with a change of DEZ flow rate at the same film thickness of 1100 nm.

peting orientations developing up to few hundreds of nanometers. The texture development starts at a later stage. Because of the mixed <002> - <103> texture up to 1100 nm film thickness, differences in lateral growth rates of the two orientations will result in void formation throughout the entire top part of the layer. Note that the difference in texture between low and *high DEZ* samples can be recognized from the TEM images: in Figure 3.5b the shape of the top facets is not symmetric, while the one associated to *low DEZ* conditions in Figure 3.5a is symmetric, as it should be when the <002> develops along the sample's normal. Formation and further development of the voids up to 1100 nm forces the electrons to diffuse through a longer percolation path, when traveling in the lateral direction, thus causing additional losses by, e.g., ionized impurities. Therefore, with the onset in void development, the resistivity does not further decrease with thickness.

3.4 Conclusions

Two ZnO:Al thickness series have been investigated in details, one showing a strong resistivity gradient as function of the thickness with a minimum of $3 \cdot 10^{-4}$ $\Omega \cdot$cm at a film thickness of 1100 nm and the other one characterized by a constant resistivity of $4 \cdot 10^{-4}$ $\Omega \cdot$cm from 300 nm film thickness onwards. It is striking, that the film deposited at *high DEZ* conditions shows the same resistivity as 700 nm-thick at the *low DEZ*, but at the thickness of only 300 nm, exhibiting even higher transmittance. The difference in resistivity, which is dependent on the injected diethylzinc flow rate, is interpreted in terms of electrical properties, morphology and initial ZnO:Al growth development. A correlation between the mobility and resistivity trends was observed under both growth conditions: the reduction of resistivity was accompanied by an increase in mobility (up to 33 $\mathrm{cm}^2/\mathrm{V}\cdot\mathrm{s}$) in the whole thickness range of *low DEZ*, the constant resistivity starting from 300 nm at *high DEZ* conditions was related to the constant mobility trend observed in that thickness range. Films deposited at *high DEZ* flow are characterized by a lower deposition rate accompanied by an initial (within first ~100 nm) growth of randomly textured, dense and large grain size ZnO:Al. With the further development of the bulk of the layer, only <002> and <103> orientations dominate the film growth and lead to the formation of voids in material, starting from ~300 nm onwards. On the contrary, voids are already present in the initial stages of growth in the *low DEZ* thickness series, because of the preferred crystallographic orientation <002>. This void-rich initial phase is responsible for the gradient in resistivity and, eventually, mobility. The control on the growth development in terms of crystal orientation selection in the early phases of growth appears fundamental in determining the AZO layer electrical properties.

Bibliography

[1] D. C. Look, B. Claflin, Y. I. Alivov, and S. J. Park, Physica Status Solidi (a) **201**, 2203 (2004).

[2] S. Pearton, Progress in Materials Science **50**, 293 (2005).

[3] C. G. Granqvist, Solar Energy Materials and Solar Cells **91**, 1529 (2007).

[4] R. L. Hoffman, Journal of Applied Physics **95**, 5813 (2004).

[5] E. M. C. Fortunato, P. M. C. Barquinha, A. C. M. B. G. Pimentel, A. M. F. Goncalves, A. J. S. Marques, L. M. N. Pereira, and R. F. P. Martins, Advanced Materials **17**, 590 (2005).

[6] J. Muller, B. Rech, J. Springer, and M. Vanecek, Solar Energy **77**, 917 (2004).

[7] J. Krc, Thin Solid Films **426**, 296 (2003).

[8] T. Minami, Semiconductor Science and Technology **20**, S35 (2005).

[9] U. Betz, M. Kharrazi Olsson, J. Marthy, M. Escolá, and F. Atamny, Surface and Coatings Technology **200**, 5751 (2006).

[10] A. V. Shah, H. Schade, M. Vanecek, J. Meier, E. Vallat-Sauvain, N. Wyrsch, U. Kroll, C. Droz, and J. Bailat, Progress in Photovoltaics: Research and Applications **12**, 113 (2004).

[11] B. Rech, T. Repmann, S. Wieder, M. Ruske, and U. Stephan, Thin Solid Films **502**, 300 (2006).

[12] A. Matsuda, Japanese Journal of Applied Physics **43**, 7909 (2004).

[13] G. Bugnon, A. Feltrin, F. Meillaud, J. Bailat, and C. Ballif, Journal of Applied Physics **105**, 064507 (2009).

[14] M. Ohyama, H. Kozuka, and T. Yoko, Journal of the American Ceramic Society **81**, 1622 (2005).

[15] S. Shinde, P. Shinde, S. Pawar, A. Moholkar, C. Bhosale, and K. Rajpure, Solid State Sciences **10**, 1209 (2008).

[16] T. Minami, T. Miyata, and T. Yamamoto, Journal of Vacuum Science & Technology A: Vacuum, Surfaces, and Films **17**, 1822 (1999).

[17] V. Sittinger, F. Ruske, W. Werner, C. Jacobs, B. Szyszka, and D. J. Christie, Thin Solid Films **516**, 5847 (2008).

[18] O. Kluth, Thin Solid Films **351**, 247 (1999).

[19] H. Agura, A. Suzuki, T. Matsushita, T. Aoki, and M. Okuda, Thin Solid Films **445**, 263 (2003).

[20] H. Tanaka, K. Ihara, T. Miyata, H. Sato, and T. Minami, Journal of Vacuum Science & Technology A: Vacuum, Surfaces, and Films **22**, 1757 (2004).

[21] D. Kim, H. Kang, J.-M. Kim, and H. Kim, Applied Surface Science **257**, 3776 (2011).

[22] D.-J. Lee, H.-M. Kim, J.-Y. Kwon, H. Choi, S.-H. Kim, and K.-B. Kim, Advanced Functional Materials **21**, 448 (2011).

[23] J. Steinhauser, S. Fay, N. Oliveira, E. Vallat-Sauvain, and C. Ballif, Applied Physics Letters **90**, 142107 (2007).

[24] R. Groenen, J. Löffler, P. M. Sommeling, J. L. Linden, E. A. G. Hamers, R. E. I. Schropp, and M. C. M. van de Sanden, Thin Solid Films **392**, 226 (2001).

[25] S. Y. Myong, S. J. Baik, C. H. Lee, W. Y. Cho, and K. S. Lim, Japanese Journal of Applied Physics **36**, L1078 (1997).

[26] A. Illiberi, B. Kniknie, J. van Deelen, H. Steijvers, D. Habets, P. Simons, A. Janssen, and E. Beckers, Solar Energy Materials and Solar Cells **95**, 1955 (2011).

[27] I. Volintiru, M. Creatore, B. J. Kniknie, C. I. M. A. Spee, and M. C. M. van de Sanden, Journal of Applied Physics **102**, 043709 (2007).

[28] W. W. Wenas, A. Yamada, K. Takahashi, M. Yoshino, and M. Konagai, Journal of Applied Physics **70**, 7119 (1991).

[29] S. Faÿ, J. Steinhauser, S. Nicolay, and C. Ballif, Thin Solid Films **518**, 2961 (2010).

[30] C. Agashe, O. Kluth, G. Schöpe, H. Siekmann, J. Hüpkes, and B. Rech, Thin Solid Films **442**, 167 (2003).

[31] I. Volintiru, M. Creatore, and M. C. M. van de Sanden, Journal of Applied Physics **103**, 033704 (2008).

[32] M. C. M. van de Sanden, R. J. Severens, W. M. M. Kessels, R. F. G. Meulenbroeks, and D. C. Schram, Journal of Applied Physics **84**, 2426 (1998).

[33] C. G. van de Walle, Physical Review Letters **85**, 1012 (2000).

[34] J. W. Orton and M. J. Powell, Reports on Progress in Physics **43**, 1263 (1980).

[35] J. Y. W. Seto, Journal of Applied Physics **46**, 5247 (1975).

[36] H. McMurdie, M. Morris, E. Evans, B. Paretzkin, W. Wong-Ng, L. Ettlinger, and C. Hubbard, Powder diffraction **1**, 76 (1986).

Chapter 4

Plasma processes and the role of oxygen during Expanding Thermal Plasma deposition of aluminum-doped ZnO[*]

Abstract

(Plasma-enhanced) chemical vapor deposition processing of transparent conductive oxides, such as ZnO, is often accompanied by the development of a resistivity gradient as function of the film thickness, which can hamper its application as well as affect its production costs. Recently, the development of the resistivity gradient has been investigated with respect to the several growth steps involved in plasma-enhanced (expanding thermal plasma) chemical vapor deposited ZnO layers. The role of the precursor feed composition, i.e. the diethylzinc-to-O_2 flow rate ratio, has been identified as responsible for the gradient in resistivity, since it affects the early stages of growth in terms of nucleation, grain size and crystal orientation, allowing to reach a resistivity value of $4 \cdot 10^{-4}$ $\Omega \cdot$cm for a film thickness of 300 nm. The present contribution investigates the experimental conditions under which the control on the resistivity gradient is achieved, in terms of plasma processes and plasma/surface interaction. In particular, the chemistry channels developed in the downstream region of the expanding thermal plasma, i.e. where diethylzinc and O_2 are injected, are presented as supported by Langmuir Probe and Mass Spectrometry measurements. The results are then correlated with the crystal orientations developed as function of the diethylzinc-to-O_2 ratio and the layer growth rate. It is concluded that the diethylizinc-to-O_2 ratio allows tuning the atomic oxygen flux availability at the surface, therefore influencing the development of specific crystal orientations, which eventually affect the early stages of growth of the ZnO layers and therefore its electrical properties.

---

[*] To be submitted

4.1 Introduction

In the quest for low resistivity, high transmittance and reduced material costs, several deposition techniques, such as spray pyrolysis [1], sol-gel [2], magnetron sputtering [3–5], pulsed laser deposition [6, 7], atomic layer deposition [8, 9] and chemical vapor deposition (CVD) [10] are being investigated for the deposition of ZnO layers. CVD techniques, such as metal-organic chemical vapor deposition (MO-CVD), demonstrated high quality ZnO:Al layers [11, 12]: amongst them, the Expanding Thermal Plasma (ETP), has achieved ZnO:Al layers deposited up to 0.75 nm/s with a resistivity of about $3{\cdot}10^{-4}$ $\Omega{\cdot}$cm for 1100 nm - thick film [13]. However, a significant drawback of CVD processes [14–16] is the development of a gradient in resistivity extended over a thickness range of several hundred nanometers. In the case of ETP-grown ZnO:Al, this effect resulted in a factor 500 reduction in resistivity when the thickness increased from 70 to 1300 nm and this was found to be correlated with the development of a pyramid-like morphology during the growth of the ZnO:Al grains [14]. Ellipsometry studies demonstrated that the high in-grain quality was mainly limited by scattering at the grain boundaries [17]: a pyramid-like growth allowed the development of ZnO:Al layers progressively less affected by scattering at the grain boundaries, as the grain size increased with film thickness, leading to low resistivity layers.

Our recent efforts have been dedicated to the massive reduction of the resistivity gradient and the development of highly conductive thin ZnO:Al layers, exhibiting a resistivity value as low as $4{\cdot}10^{-4}$ $\Omega{\cdot}$cm for a film thickness of 300 nm [13]. The reduction of resistivity gradient has been experimentally controlled by the flow rate of the deposition precursor, i.e. diethylzinc (DEZ).

In short, from the growth point of view, the following was demonstrated: films characterized by a resistivity gradient exhibited a small grain size in the initial layer (30-50 nm for 100 nm film thickness), dominant <002> texture and void inclusion up to ∼500 nm of ZnO:Al film thickness. As a consequence, the resistivity was reduced over 2 orders of magnitude in the range of 50-1100 nm, reaching $3.0{\cdot}10^{-4}$ $\Omega{\cdot}$cm at 1100 nm. In contrast, films with a limited gradient obtained at higher DEZ flow showed already a larger grain size in the initial stages of growth (60-80 nm for 100 nm film thickness) and the coexistence of multiple crystal orientations. From 300 nm onwards a competitive growth of <002> and <103> crystal orientations and void inclusion were observed, limiting the further development of the grain size and leading to the saturation of the resistivity values to $4{\cdot}10^{-4}$

Ω·cm. Next to the control of electrical properties as a function of film thickness, it was also observed that the change in DEZ flow rate led to a decrease in growth rate, namely from ∼0.75 nm/s for the ZnO:Al characterized by the resistivity gradient, down to ∼0.25 nm/s for the ZnO:Al grown under *high DEZ* flow rate conditions.

The above-reported overview of the most recent efforts and results towards excellent quality ZnO:Al layers point out towards not yet unraveled effects of the DEZ flow rate on the developed plasma chemistry and plasma/surface interaction processes. Thus, it is desired to investigate the clear effect of DEZ flow on the ZnO:Al growth in terms of plasma processes, in particular, radical formation and atomic oxygen flux at the film surface as a function of DEZ flow.

The present contribution, therefore, aims identifying and addressing the plasma and plasma/surface interaction processes, which develop under the earlier described deposition conditions for the ZnO:Al films, characterized by a limited and extended resistivity gradient. In this framework, the evolution of the plasma-generated species with the increase in DEZ flow rate is studied by means of Mass Spectrometry, with the purpose of identifying the key parameter during the film growth leading to the earlier described morphological and electrical properties of the ZnO:Al layers.

The chapter is organized as follows: section 4.2 describes the experimental details and the analysis tools. Section 4.3 addresses the reactions involving the deposition precursor DEZ in the presence of an O_2-fed expanding thermal plasma, based on earlier literature studies and mass spectrometry measurements as function of the injected DEZ flow rate. The surface processes during the ZnO:Al growth are then addressed and conclusions are drawn.

4.2 Experimental details

ZnO:Al films were deposited by means of a remote plasma-enhanced chemical vapor deposition process, the ETP [11, 14, 18]. A cascaded arc unit, used as the plasma source, generates a DC discharge between three cathodes and an anode plate (I=50 A) at sub-atmospheric pressure ($0.41\cdot10^5$ Pa) in argon (G_{Ar}=1000 sccm). Due to the pressure difference between the plasma source and the low pressure deposition chamber (170 Pa), the ionized argon expands into the chamber and dissociates the precursors, injected via rings into the plasma jet. At 6.5 cm downstream from the plasma source oxygen was injected (G_{O_2}= 100 sccm);

Table 4.1. Differences between the *high* and *low DEZ* conditions.

Parameter	*high DEZ*	*low DEZ*
DEZ flow rate, g/h	9.0	5.5
Grain size of initial layer (~100 nm), nm	60-80	30-50
Carrier concentration, cm^{-3}	$(7\text{-}9)\cdot 10^{20}$	$(3\text{-}6)\cdot 10^{20}$
Aluminum concentration, at. %	1.4±0.1	0.9±0.1
Stoichiometry Zn/O/H	1/1/0.04	1/1/0.05
Growth flux, at/$cm^2\cdot s$	$(1.9\pm0.2)\cdot 10^{15}$	$(5.5\pm0.6)\cdot 10^{15}$

further downstream at 30 cm from the plasma source evaporated and pre-mixed diethylzinc (DEZ) and trimethylaluminum (TMA) were injected (G_{DEZ}=3.2-9.0 g/h; G_{TMA}=0.2 g/h). The plasma generates growth radicals, which convectively reach the substrate placed at 50 cm from the source and lead to the deposition of ZnO:Al films. Material comparison was performed at two chosen experimental conditions, i.e., at G_{DEZ}=5.5 g/h (for simplicity defined as "*low DEZ*") and G_{DEZ}=9 g/h (defined as "*high DEZ*"), representing films with and without resistivity gradient, respectively.

Characterization of the films was carried out on mono-crystalline silicon substrates of 1x1 inch^2 size with 400 nm thermal oxide. Thickness and sheet resistance were measured with profilometer and four-point probe, respectively. Rutherford Backscattering Spectrometry (RBS) analysis was employed to quantify the elemental concentration of Zn, O and Al elements. Hydrogen content was measured by means of elastic recoil detection analysis (ERD). Both RBS and ERD were performed using 2 MeV He^+ ions produced by a HVE 3.5 MV singletron. Mass-spectrometry (MS) analysis was performed using a Pfeiffer Vacuum Prisma QME 200 quadrupole mass-spectrometer located on the side of the deposition chamber at the substrate level. Background gas was sampled through a 10 µm pinhole, so only stable reaction products could be detected. Since only the DEZ flow rate was changed, the signal intensities of the measured masses were normalized to the one of argon to exclude any pressure effect. In order to determine the depletion of O_2 in the presence of an increasing DEZ flow rate, oxygen-containing ion masses (m/z=16 and 32 amu) have been investigated and the depletion of O_2 has been calculated as $D=(I_{off}-I_{on})/I_{off}$. Here, I_{off} is the signal intensity of the corresponding m/z, when the plasma source is switched off and I_{on} is the signal intensity of the corresponding m/z, when the plasma switched on and the oxygen, DEZ and TMA precursors were injected.

As plasma ionization and dissociation processes are driven in ETP by argon ions (Ar^+) and electrons [19–21], it is essential to determine the Ar^+ flux produced by the plasma source, i.e. the plasma source ionization efficiency. Following the procedure described by van Hest *et al.* [22], the efficiency of the plasma source was determined by Langmuir probe measurements in pure Ar plasma under the same cascaded arc conditions used for the deposition. From the measurements across the plasma jet, at a position of 10 mm from the substrate holder the ion density profile was obtained. According to van Hest *et al.* [22], when no oxygen is added to the plasma, the ion flow is independent from the distance to the arc exit, which indicates that there is no significant recombination between argon ions and electrons in the plasma beam [18]. Therefore, the distance from the plasma source can be chosen arbitrarily. The obtained ion density profile is further used to calculate the flux (ions/cm^2·s) of Ar^+ ions as a function of the distance across the jet. The integration over the exposed surface area provides a total ion flow rate. With the reasonable assumption of a drift velocity of 400 m/s at the measurement level, the plasma source ionization efficiency was calculated to be ∼3 % and considered throughout the manuscript.

In order to identify the plasma processes responsible for the observed changes in terms of the earlier described morphological and electrical properties of the ZnO:Al layers, Table 1.1 summarizes the growth and film properties of the *low DEZ* and *high DEZ* ZnO:Al layers. The large grain size of *high DEZ* ZnO:Al at the initial growth stage is also accompanied by a high carrier concentration, which correlates with the higher aluminum concentration. Despite the significant differences in electrical properties and structure, films are characterized by the same stoichiometry, as derived from RBS measurements. The hydrogen content is quantified to be 1.9 at. % at *high DEZ* conditions and 2.4 at. % at *low DEZ* conditions. Furthermore, both layers are found carbon-free, within the detection limit of 5 at. %. The growth flux was a factor 3 lower at *high DEZ* conditions: $\Phi(\textit{high DEZ})=1.9\cdot10^{15}$ at/cm^2·s, as compared to $\Phi(\textit{low DEZ})=5.5\cdot10^{15}$ at/cm^2·s, despite the factor 1.6 higher DEZ dosing rate. To summarize, a change in DEZ flow rate appears to massively influence the growth and electrical properties of ZnO:Al layer, although without affecting the layer stoichiometry. In the next section, therefore, it is addressed whether the change in DEZ flow rate affects the plasma chemistry channels and eventually the plasma/surface interaction processes.

4.3 Results and Discussion

The gas phase chemistry is here addressed by describing the global reaction route to ZnO synthesis from DEZ and oxygen, and the reactions, which presumably take place in argon-fed expanding thermal plasma. On the basis of these reaction paths the trends of the stable species monitored by means of Mass Spectrometry are interpreted. Finally, the plasma chemistry studies are correlated with the material properties and conclusions are drawn with respect to the ZnO:Al growth development.

A global reaction of DEZ with oxygen leads to the formation of ZnO according to 4.1:

$$Zn\left(C_2H_5\right)_2 + \frac{(14-x)}{2}O_2 \rightarrow ZnO + xCO + (4-x)\,CO_2 + 5H_2O \tag{4.1}$$

Where x is in the range (0-4). By tuning the O_2/ DEZ ratio injected in the plasma, the reaction can shift from CO to CO_2 production, which is detected by means of mass-spectrometry.

Generally, there are electrons, argon atoms, ions and metastables present in an Ar plasma and only Ar^+ ions and electrons play an important role in precursor dissociation processes [19–21, 23]. As it was previously reported for the ETP growth of ZnO:Al, Ar^+ ions dissociate precursor molecules and allow the formation of hydrocarbon species [21], according to equations (4.2) and (4.3). Previous studies carried out on organosilicon precursors such as hexamethyldisiloxane (HMDSO) [23, 24], showed that the charge exchange reaction rate between Ar^+ and HMDSO is at least one order of magnitude higher than the charge exchange reaction rate of Ar^+ with O_2 molecules. Also, reaction rate of Ar^+ with trimethylaluminum was demonstrated to be $(5.9\pm0.5)\cdot10^{-16}$ m^3/s [25], which is in the same order of magnitude as reaction Ar^+ with HMDSO. Therefore, for the present study, it is reasonable to assume that the charge exchange reactions of Ar^+ with DEZ (4.2) and (4.3) are faster, than those with O_2. Therefore, the reaction between Ar^+ and DEZ molecules leads to dissociative ionization of the DEZ molecule:

$$Ar^+ + Zn\left(C_2H_5\right)_2 \rightarrow ZnC_2H_5^+ + C_2H_5 + Ar \tag{4.2}$$

Table 4.2. Flow rates of Ar ions and precursors at low and *high DEZ* conditions

Substance	Flow rate, stand. units	Flow rate, molecules/s
Argon ions (Ar^+)	33 sccm	$1.48{\cdot}10^{19}$
Oxygen (O_2)	100 sccm	$4.48{\cdot}10^{19}$
DEZ (*low DEZ*)	5.5 g/h	$7.45{\cdot}10^{18}$
DEZ (*high DEZ*)	9.0 g/h	$1.22{\cdot}10^{19}$

$$Ar^+ + Zn\left(C_2H_5\right)_2 \rightarrow ZnC_2H_5 + C_2H_5^+ + Ar \tag{4.3}$$

Both reactions (4.2) and (4.3) can take place, since Jiao *et al.* [26] demonstrated branching ratios for these reactions to be equal to 32 % and 28 %, respectively. The other routes to organic and Zn-containing ions are less dominant, each below 10 % [26]. Electron-induced dissociation of the precursor molecules is considered to have a negligible contribution under the given plasma conditions. The dissociation of the first and second Zn-C bond in a DEZ molecule require 2.27 and 0.95 eV, respectively [27]. Since the average electron temperature is below 0.3 eV, the electron density with the energy above 0.95 eV is smaller than the Ar^+ density, and therefore the charge exchange processes dominate. Based on the plasma source efficiency of about 3 %, as derived from Langmuir probe measurements, the Ar^+/DEZ ratio is equal to 2 at *low DEZ* and about 1 at *high DEZ* conditions (see Table 4.2). In conclusion, Ar^+ ions are always in surplus compared to DEZ, as reported in the Table 4.2.

The reactions (4.2) and (4.3) are followed by dissociative recombination of ZnC_2H_5 and C_2H_5 with an electron (for ions), or further dissociative charge exchange with Ar^+ ion (for radicals):

$$ZnC_2H_5^+ + e^- \rightarrow Zn + C_2H_5 \tag{4.4}$$

$$C_2H_5^+ + e^- \rightarrow C_2H_4 + H \tag{4.5}$$

$$ZnC_2H_5 + Ar^+ \rightarrow Zn + C_2H_5^+ + Ar \tag{4.6}$$

$$C_2H_5 + Ar^+ \rightarrow CH_3^+ + CH_2 + Ar \tag{4.7}$$

The produced alkyl radicals and hydrogen atoms allow the development of the hydrocarbon chemistry. The surplus of Ar^+ ions can then contribute to the production of atomic oxygen via charge exchange reactions (1.8) with oxygen, followed by dissociative recombination (4.9) of the produced O_2^+ with electrons:

$$Ar^+ + O_2 \rightarrow Ar + O_2^+ \tag{4.8}$$

$$O_2^+ + e^- \rightarrow O + O^* \tag{4.9}$$

Here, the charge exchange reaction rate is significantly lower ($6{\cdot}10^{-17}$ m^3/s), compared to the rate of dissociative recombination of molecular oxygen ($1{\cdot}10^{-13}$ m^3/s), pointing out that charge exchange reaction (1.8) is a rate-limiting step for atomic oxygen formation. As mentioned above, the charge exchange rate of reaction (1.8) with O_2 is also lower than the one with DEZ (4.2) and (4.3). Oxygen is however expected to affect the hydrocarbon and oxidation chemistry also in its molecular form by reacting with the alkyl radicals produced in (4.4)-(1.7).

The mean-free path of DEZ molecules in the plasma is not affected by increasing the DEZ flow rate at a constant pressure in the deposition reactor, since the volume of the expanding plasma beam increases. Therefore, the probability for reactions between (Ar^+, e^-) and DEZ is expected to stay constant. The injected O_2 flow rate is constant and always larger than the DEZ and (Ar^+, e^-) flow rates (Table 4.2). Under the oxygen-rich conditions, such as *low DEZ*, it can be expected that the surplus of (Ar^+, e^-) can react with O_2, according to reactions (1.8) and (4.9), with a theoretical maximum depletion of O_2 equal to 33 % (ratio between flow rates of Ar^+ ions and molecular oxygen from the Table 4.2) in the absence of DEZ molecules. The measured O_2 depletion is shown in the as a function of DEZ flow rate.

Already for a DEZ flow rate of 3.2 g/h (Figure 4.1) the O_2 depletion is above 50 %, i.e. larger than the theoretical maximum of 33 %, based on the assumption that O_2 depletion occurs only from the interaction with (Ar^+, e^-). Experimentally, the O_2 depletion in Ar/O_2 plasma was measured to be significantly low and equal to 5 % (Figure 4.1), which also includes atomic oxygen recombination losses to O_2 at the walls of the deposition chamber. From this comparison it can be then concluded that O_2 is consumed mostly through combustion of DEZ fragments produced through reactions (4.4)-(1.7) in an Ar/O_2/DEZ plasma and heterogeneous reactions at the surface of the growing layer. For the same oxygen

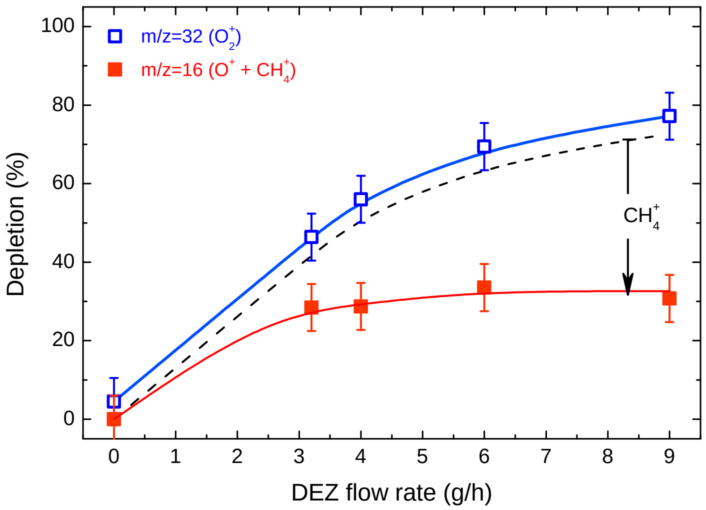

Figure 4.1. Depletion of the m/z= 16 and 32 as a function of DEZ flow rate. Black dashed line: expected depletion profile, if m/z=16 would be related only to O^+, based on the cracking pattern of O_2 in the mass-spectrometer. Reduction of m/z=16 depletion, caused by the increasing contribution of CH_4^+ to the 16 amu signal, is also shown.

flow rate as used in this work and G_{DEZ}=1.7 g/h, the O_2 depletion measured by Groenen *et al.* [21] was equal to 25 %, in agreement with the trend reported in the Figure 4.1. It is worth noticing that this agreement in terms of O_2 depletion occurs even in the presence of different Ar^+ fluxes, i.e. $\sim 3.8 \cdot 10^{19}$ ions/sec in the work of Groenen *et al.* and $1.5 \cdot 10^{19}$ ions/sec in this work. This leads to the general conclusion that the oxygen depletion is controlled by the injected DEZ flow rate, provided that there is a surplus of the Ar^+ ions with respect to DEZ, to promote DEZ dissociation. The latter condition is satisfied in both cases here under investigation.

It can be furthermore concluded that there is always enough O_2 to promote the deposition of carbon-free ZnO layers, since the depletion of O_2 is not quantitative, even at large DEZ flow rates (Figure 4.1). Furthermore, it is also known that ZnO has a lower formation enthalpy (-351 kJ/mol) than Al_2O_3 (-1676 kJ/mol) [28, 29]. Due to the lower atomic oxygen available at *high DEZ* conditions, Al_2O_3 development is less favorite, therefore leading to more Al present in the active form and higher carrier concentration (Table 4.1). Moreover, it is plausible to conclude that the direct reaction of undecomposed DEZ with molecular oxygen is unlikely to occur, otherwise, the O_2 depletion in Figure 4.1 would increase linearly with the injected DEZ flow rate. Therefore, after reactions (4.2) and (4.3) one of the possible reactions would see oxygen taking part in:

$$ZnC_2H_5 + O_2 \rightarrow Zn + CO + CH_4 + OH \tag{4.10}$$

$$C_2H_5 + O_2 \rightarrow CO + CH_4 + OH \tag{4.11}$$

There was no Zn observed in mass-spectra, pointing to the low gas phase concentration of Zn-related products. The depletion of O_2 can be ideally calculated by both signals at masses 16 and 32 amu. Being a result of DEZ decomposition, the contribution of CH_4^+ in m/z=16 is increasing with increase in DEZ flow rate, therefore, the depletion curve of m/z=16 deviates from the one corresponding to the signal at 32 amu (Figure 4.1). The strongest difference is observed for the largest DEZ flow rate here under investigation, i.e. 9 g/h, where contribution of CH_4^+ in m/z=16 is up to 60 %. Such a strong increase in CH_4^+ is in agreement with a production of other hydrocarbons shown in Figure 4.2.

Signal intensities of several oxygen- and hydrocarbons-containing masses are measured and plotted in Figure 4.2 as function of the DEZ flow rate. The analyzed masses could be divided into two sub-groups, i.e. one related to hydrocarbon species and one related to hydrocarbons and/or oxidation products. The first sub-group, namely m/z=27 ($C_2H_3^+$) and 29 ($C_2H_5^+$), is attributed to the fragments of DEZ decomposition and characterized by a linear increase with DEZ flow. The second sub-group shows either a sub-linear increase as in the case of m/z=28 ($C_2H_4^+$ and CO^+) or a plateau for m/z=18 (H_2O) and 44 ($C_3H_8^+$ and CO_2^+) or a strong increase as in the case of m/z=2 (H_2^+). The diversity of the trends in this sub-group can be related to the oxygen involvement in formation of these species, so the balance between hydrocarbon- and oxygen-containing ions can strongly change as a function of DEZ concentration in plasma. A limited increase in the H_2O associated signal (m/z=18 in Figure 4.2) in the investigated range of DEZ flow rate suggests that the produced water is being consumed in reactions with DEZ [30, 31], i.e.:

$$Zn\left(C_2H_5\right)_2 + H_2O \rightarrow ZnC_2H_5OH + C_2H_6 \tag{4.12}$$

In the case of m/z=28, also present in Figure 4.2, it is hard to discern between $C_2H_4^+$ and CO^+ contributions, since formation of both of them is likely, due to the surplus of oxygen introduced into the process and reactions (4.10)-(4.12). As support for C_2H_6 production, an increasing signal from $C_2H_5^+$ (m/z=29) develops as function of the DEZ flow rate. So, there is a strong evidence of hydrocarbons production with increase in DEZ flow and oxygen consumption in reactions with hydrocarbons.

As concluded earlier, the injected oxygen is not fully depleted even under the *high DEZ* conditions and its consumption is controlled by the injected DEZ flow rate. The fact that the growth flux is a factor of 3 lower at *high DEZ* conditions (see Table 4.1) with respect to the *low DEZ* conditions, although all layers are equally stoichiometric and carbon-free, provides strong evidence that the growth rate of the ZnO:Al film is controlled by the atomic oxygen flux arriving at the surface.

Under the plausible assumption that the charge exchange reaction of Ar^+ with DEZ molecules is the dominant reaction occurring in the plasma phase, it is possible to estimate the Ar^+ flux still available for reactions with O_2 molecules. Under the hypothesis that each Ar^+ ion reacts with one DEZ molecule, the excess amount of Ar^+ at *low DEZ* conditions is $\Phi_{Ar+,low}$=7.5·10^{18} ions/s, while at *high DEZ* is only $\Phi_{Ar+,high}$=2.5·10^{18} ions/s. This difference corresponds to the factor 3 difference in terms of growth flux earlier mentioned. It can be therefore argued that the ZnO:Al growth is primarily controlled by the atomic oxygen flux reaching the surface, therefore influencing the ZnO:Al properties in terms of abstraction of carbon-containing moieties and efficient Al doping. At the same time, molecular oxygen is mainly involved in the combustion reactions with DEZ fragments. All these experimental observations point out towards the synthesis of Zn-O bonds occurring at the surface of the growing layer, which is in agreement with the suggestion earlier raised by Groenen *et al.* [21].

Keeping in mind the conclusion just drawn on the role of the atomic oxygen flux at the surface as limiting step to the ZnO crystal growth, it is possible to comment on the role of the plasma processes on the film morphology earlier reported in [13]. There are two processes which can be influenced by the atomic oxygen flux arriving at the growing ZnO surfaces: 1) surface diffusion and 2) surface stability of the different facets of ZnO.

Here, it is essential to highlight that the ZnO hexagonal wurtzite crystal structure lacks inversion symmetry [32, 33]. This means that the opposing polar (0001) and (000-1) facets differ from each other and are Zn- and O-terminated, respec-

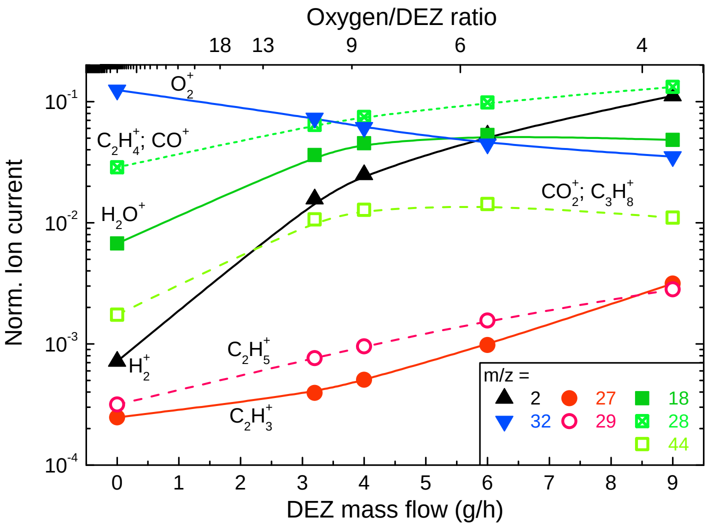

Figure 4.2. Ion current of reaction products (corresponding m/z values are shown in the legend) obtained from mass-spectrometry measurements and normalized to ion current of argon (m/z=40), plotted as a function of DEZ flow rate.

tively. Dong *et al.* [34] demonstrated that Zn- and O- polarity of the ZnO (0001) polar surface affects its optical properties, with oxygen-terminated facets exhibiting twice higher defect emission. Yu and Liu [35] showed that the surface roughness of the Zn-polar and O-polar surfaces are different and dependent on the oxygen concentration on the surface. On a Zn-polar surface, the topmost Zn atoms are connected to O adatoms by a single dangling bond. At high concentrations, this surface is covered by a monolayer of O adatoms, enabling fast 2-dimensional growth. Under similar conditions, the O-polar surface leads to 3-dimensional island growth. Thus, it can be expected that decreasing the atomic oxygen flux at the surface will lead to a limited coverage of the surface with oxygen, thereby reducing the growth rate of these facets. Furthermore, Zn-polar face is instable to atomic hydrogen [36], which is particularly abundant under *high DEZ* conditions (Figure 4.2), also being a factor contributing to the reduced growth rate observed under *high DEZ* condition. As a result of this decrease in growth rate, crystals with other facets pointing upwards (such as (103) facets) are less limited in the competition for the vertical/columnar growth. Thus, by reducing the availability of the atomic oxygen flux, the development of a <002> texture may be suppressed in favor of e.g. the <103> texture, as observed for *high DEZ* conditions.

4.4 Conclusions

Following our previous studies mainly focused on the tunability and control of electrical properties of the plasma-deposited ZnO:Al, in particular, resistivity gradient, the present work investigated the plasma processes developed in an Ar-fed ETP in the presence of O_2/DEZ/TMA mixtures. The plasma processes have been interpreted on the basis of mass spectrometry and a detailed quantification of the reactants present in the downstream region of the ETP, namely, the Ar^+ flow rate (determined by means of Langmuir probe measurements) and the O_2 and DEZ flow rates. The charge exchange reaction of Ar^+ with DEZ molecules appears to be the dominant reaction occurring in the plasma phase, and the excess amount of Ar^+ at *low DEZ* and *high DEZ* conditions, available for O_2 dissociation, correlates with the growth flux towards the surface. It is therefore concluded that the ZnO:Al growth is primarily controlled by the atomic oxygen flux reaching the surface, influencing the ZnO:Al properties in terms of carbon abstraction and efficient Al doping. The decrease in atomic oxygen flux at the surface leads to a limited coverage of the surface with oxygen, thereby reducing the growth rate of the polar facets, i.e. (002). As a result of this decrease in growth rate, crystals with other facets pointing upwards (such as (103) facets) are less limited in the competition for the vertical/columnar growth. Thus, by reducing the availability of the atomic oxygen flux, the development of a <002> texture may be suppressed in favor of e.g. the <103> texture, as observed for *high DEZ* conditions. The effect also opens up a route to increase of ZnO:Al growth rate with a low resistivity gradient and, next to obtaining highly conductive layers at low thickness, to reduce production cost even further.

Acknowledgments The authors would like to thank Dr. H.C.M. Knoops for assistance during experiments and M.J.F. van de Sande for the technical support.

Bibliography

[1] S. Shinde, P. Shinde, S. Pawar, A. Moholkar, C. Bhosale, and K. Rajpure, Solid State Sciences **10**, 1209 (2008).

[2] M. Ohyama, H. Kozuka, and T. Yoko, Journal of the American Ceramic Society **81**, 1622 (2005).

[3] T. Minami, Journal of Vacuum Science & Technology A: Vacuum, Surfaces, and Films **17**, 1765 (1999).

[4] V. Sittinger, F. Ruske, W. Werner, C. Jacobs, B. Szyszka, and D. J. Christie, Thin Solid Films **516**, 5847 (2008).

[5] O. Kluth, Thin Solid Films **351**, 247 (1999).

[6] H. Agura, A. Suzuki, T. Matsushita, T. Aoki, and M. Okuda, Thin Solid Films **445**, 263 (2003).

[7] H. Tanaka, K. Ihara, T. Miyata, H. Sato, and T. Minami, Journal of Vacuum Science & Technology A: Vacuum, Surfaces, and Films **22**, 1757 (2004).

[8] D. Kim, H. Kang, J.-M. Kim, and H. Kim, Applied Surface Science **257**, 3776 (2011).

[9] D.-J. Lee, H.-M. Kim, J.-Y. Kwon, H. Choi, S.-H. Kim, and K.-B. Kim, Advanced Functional Materials **21**, 448 (2011).

[10] J. Steinhauser, S. Fay, N. Oliveira, E. Vallat-Sauvain, and C. Ballif, Applied Physics Letters **90**, 142107 (2007).

[11] R. Groenen, J. Löffler, P. M. Sommeling, J. L. Linden, E. A. G. Hamers, R. E. I. Schropp, and M. C. M. van de Sanden, Thin Solid Films **392**, 226 (2001).

[12] S. Y. Myong, K. Sriprapha, S. Miyajima, M. Konagai, and A. Yamada, Applied Physics Letters **90**, 263509 (2007).

[13] M. V. Ponomarev, M. A. Verheijen, W. Keuning, M. C. M. van de Sanden, and M. Creatore, Journal of Applied Physics **112**, 043708 (2012).

[14] I. Volintiru, M. Creatore, B. J. Kniknie, C. I. M. A. Spee, and M. C. M. van de Sanden, Journal of Applied Physics **102**, 043709 (2007).

[15] W. W. Wenas, A. Yamada, K. Takahashi, M. Yoshino, and M. Konagai, Journal of Applied Physics **70**, 7119 (1991).

[16] S. Faÿ, J. Steinhauser, S. Nicolay, and C. Ballif, Thin Solid Films **518**, 2961 (2010).

[17] I. Volintiru, M. Creatore, and M. C. M. van de Sanden, Journal of Applied Physics **103**, 033704 (2008).

[18] M. C. M. van de Sanden, J. M. de Regt, and D. C. Schram, Physical Review E **47**, 2792 (1993).

[19] M. C. M. van de Sanden, R. J. Severens, W. M. M. Kessels, R. F. G. Meulenbroeks, and D. C. Schram, Journal of Applied Physics **84**, 2426 (1998).

[20] W. M. M. Kessels, R. J. Severens, A. H. M. Smets, B. A. Korevaar, G. J. Adriaenssens, D. C. Schram, and M. C. M. van de Sanden, Journal of Applied Physics **89**, 2404 (2001).

[21] R. Groenen, J. L. Linden, and M. C. M. van de Sanden, Plasma Processes and Polymers **2**, 618 (2005).

[22] M. F. A. M. van Hest, B. Mitu, D. C. Schram, and M. C. M. van de Sanden, Thin Solid Films **449**, 52 (2004).

[23] M. F. A. M. van Hest, J. R. Haartsen, M. H. M. van Weert, D. C. Schram, and M. C. M. van de Sanden, Plasma Sources Science and Technology **12**, 539 (2003).

[24] M. Creatore, Y. Barrell, J. Benedikt, and M. C. M. van de Sanden, Plasma Sources Science and Technology **15**, 421 (2006).

[25] C. Q. Jiao, C. A. DeJoseph, P. Haaland, and A. Garscadden, International Journal of Mass Spectrometry **202**, 345 (2000).

[26] C. Q. Jiao, C. A. DeJoseph, and A. Garscadden, International Journal of Mass Spectrometry **235**, 83 (2004).

[27] R. L. Jackson, Chemical Physics Letters **163**, 315 (1989).

[28] D. R. Lide, editor, *CRC Handbook of Chemistry and Physics*, CRC Press, 90 edition (2010), ISBN 1-4398-5511-0.

[29] S. M. George, Chemical Reviews **110**, 111 (2010).

[30] J. D. Ferguson, A. W. Weimer, and S. M. George, Journal of Vacuum Science & Technology A: Vacuum, Surfaces, and Films **23**, 118 (2005).

[31] E. Janocha and C. Pettenkofer, Applied Surface Science **257**, 10031 (2011).

[32] A. Janotti and C. G. van de Walle, Reports on Progress in Physics **72**, 126501 (2009).

[33] U. Ozgur, Y. I. Alivov, C. Liu, A. Teke, M. A. Reshchikov, S. Dogan, V. Avrutin, S.-J. Cho, and H. Morkoc, Journal of Applied Physics **98**, 041301 (2005).

[34] Y. Dong, Z.-Q. Fang, D. C. Look, G. Cantwell, J. Zhang, J. J. Song, and L. J. Brillson, Applied Physics Letters **93**, 072111 (2008).

[35] Y.-M. Yu and B.-G. Liu, Physical Review B **77**, 1 (2008).

[36] G. Bruno, M. M. Giangregorio, G. Malandrino, P. Capezzuto, I. L. Fragalà, and M. Losurdo, Advanced Materials **21**, 1700 (2009).

Chapter 5

The influence of silver nanoparticles on the growth of aluminum-doped ZnO[*]

Abstract

Aluminum-doped ZnO (ZnO:Al) is presently adopted in several fields of application as transparent conductive oxide and acknowledged as valid alternative to indium doped tin oxide. Recently, we have reported on high quality ZnO:Al layers achieved by means of the expanding thermal plasma technique and exhibiting resistivity values as low as $4{\cdot}10^{-4}$ Ω·cm for a film thickness of 300 nm. The excellent results in terms of conductivity are related to the control on the initial stages of growth of the layer in terms of high density of nuclei, competition of several crystal orientations and large grain size. In this contribution the role of silver nanoparticles (3-5 nm in diameter) prior to the ZnO:Al growth is investigated in terms of their influence on the structure and electrical properties of the ZnO:Al layers. The silver nanoparticles act as epitaxial template, inducing an improvement in the nucleation of ZnO:Al and reduction of void inclusion throughout the film thickness: this leads to a factor two lower resistivity, mainly associated to the improved electron mobility.

---

[*] To be submitted

5.1 Introduction

Aluminum-doped ZnO (ZnO:Al) is presently adopted in several applications [1–5] as transparent conductive oxide (TCO) since it is a valid alternative to the commonly used ITO [6, 7]. Various deposition techniques have already shown high quality ZnO:Al [8–11]. For example, magnetron sputtering-grown ZnO:Al is characterized by a high transmittance combined with good electrical properties, i.e. a resistivity value down to $\sim 3\cdot 10^{-4}$ $\Omega\cdot$cm [11]. The Expanding Thermal Plasma (ETP) growth of ZnO:Al is also a very valid approach to obtain high-quality ZnO:Al layers [12, 13], exhibiting a resistivity of $4\cdot 10^{-4}$ $\Omega\cdot$cm for 300 nm – thick ZnO:Al as recently shown in [14]. The excellent results in terms of ZnO:Al conductivity at such low thickness were achieved by investigating and controlling the initial stages of growth of the layers in terms of nucleation, crystal orientation and grain size. It was concluded that a compact layer with multiple crystal orientations and a large grain size of 60-80 nm is formed within the first 100 nm of growth and further developed up to 300 nm with dominant <002> and <103> crystal planes.

In the present contribution, another route towards the improvement of the electrical properties of ZnO:Al as TCO is chosen, by applying metal nanoparticles (NPs) to favor semi-epitaxial nucleation of ZnO:Al grains. For this purpose silver was selected, since the lattice parameters of its <111> orientation match with the <002> in ZnO, which is the main crystal orientation in our films. Ag NPs of approximately a diameter equal to 3-5 nm were deposited on a glass substrate and followed by a ZnO:Al layer deposition. The presence of NPs noticeably affects the nucleation of ZnO:Al and subsequent growth, as deduced from the extensive analysis employed to study the development of the structure as function of the ZnO:Al film thickness. The Ag NPs enable the structural and optical improvement of ZnO:Al, which leads to a reduction in resistivity in the whole thickness range.

5.2 Experimental details

An Expanding Thermal Plasma deposition (ETP) setup [15, 16] was used in combination with a radio-frequency (RF) magnetron sputtering unit in the same vacuum chamber. The metal NPs were sputtered from 1 inch silver target (Kurt J. Lesker, 99.99 % purity) at the distance of 100 mm to the substrate and an angle

Table 5.1. Summary of experimental settings for sputtering Ag NPs and for subsequent ZnO:Al deposition.

Experiment	Ag sputtering	ZnO:Al
Magnetron input power, W	15	-
Applied voltage, V	185 -190	-
Argon flow, sccm	1000	1000
Arc current, A	50	50
Arc pressure $\cdot 10^5$, Pa	0.41	0.41
Deposition pressure, Pa	14	150
DEZ/TMA flow, g/h	-	3.5/0.2
Oxygen flow, sccm	-	100
Substrate temp., °C	200	200

40° from the substrate normal. This geometry was chosen to bring the sputtering source close to the substrate normal for homogeneous surface coverage, while preventing shadowing the substrates from argon plasma. An RF power of 15 W was coupled to the magnetron unit assembled with a Ag target. The argon plasma generated in the plasma source, placed perpendicular to the substrate, facilitated the sputtering process, in the similar configuration to the earlier described [16]. The plasma source is a cascaded arc where a DC discharge is generated in argon at sub-atmospheric pressure between three cathode tips and an anode plate. This ionized argon expands into the low pressure deposition chamber due to the pressure difference, thus creating a plasma jet. Argon ions emanating from the cascaded arc are involved into the sputtering process of the metallic silver target, which leads to a factor of 4-6 increased deposition rate of metal NPs, compared to the RF sputtering process in the absence of the ignited cascaded arc [16]. The increase in the deposition rate is strongly related to the density and energy of the species bombarding the metal target involved in the sputtering process. Corning 7059 glass of 25x25 mm^2 and 0.7 mm – thick substrates were used during experiments. The experimental parameters for sputtering process are shown in the Table 5.1.

To prevent oxidation of the sputtered Ag NPs, a ZnO:Al layer was deposited without breaking the vacuum using diethylzinc (DEZ) and trimethylaluminum (TMA) as main precursors for zinc and aluminum, respectively. In this case, the argon plasma jet dissociated precursors injected through rings around the jet: oxygen was injected at 6.5 cm downstream from the plasma source; evaporated and pre-mixed diethylzinc (DEZ) and trimethylaluminum (TMA) were injected further downstream at 30 cm from the plasma source. The growth precursors convectively flow towards the substrate placed at 50 cm to deposit the ZnO:Al film. Based on previous findings [13] the deposition parameters were chosen to obtain ZnO:Al with high native texturing and electrical properties suitable to serve as a front contact for thin film solar cells. The experimental parameters, as shown in Table 5.1, were kept constant for all the experiments, while the deposition time was varied to obtain different ZnO:Al layer thickness in the range of 50-950 nm. For each Ag/ZnO:Al thickness, reference samples of ZnO:Al deposited on pristine Corning glass samples were prepared at the same conditions.

The electrical properties of ZnO:Al were measured using a Jandel universal four-point probe with a cylindrical 25 mm probe head. Film thickness measurements were performed on a VEECO Dektak 8 step-profiler. The optical transmittance of ZnO:Al deposited on glass was measured by means of a Shimadzu UV-3600 spectrophotometer with integrating sphere in the wavelength range of 280-2500 nm. Cross-sectional Transmission Electron Microscopy (TEM) FEI Tecnai F30ST operating at 300 kV was used to visualize the ZnO:Al grain development at different stages of the ZnO:Al growth occurring on Ag NPs and on the pristine glass substrate. Moreover, the initial growth of ZnO:Al was investigated by depositing 50 nm – thick films on carbon-coated copper grids (TEM grids) of 5 mm in diameter. Additionally, X-Ray Diffraction (XRD) measurements were performed on a Philips PanAlytical X'pert PRO Material Research Diffractometer to study the grain development of the ZnO:Al thickness series in detail.

5.3 Results and discussion

5.3.1 Structural properties

There were significant changes in the ZnO:Al structure upon growth on Ag NPs, as observed by several measurement techniques. A first indication is given by the change in deposition rate for a 50 nm – thick ZnO:Al layer, equal to 0.94 ± 0.09 nm/s in the case of a deposition on the pristine glass and of 0.74 ± 0.07 nm/s in the case of growth on the Ag NPs. With the further development in ZnO:Al film thickness, the growth rate on Ag NPs increases and approaches the average growth rate of 0.96 ± 0.09 nm/s of the series without Ag NPs, but consistently about 8 % lower. Moreover, the Root-Mean-Square (RMS) surface roughness measured by AFM is higher for the case without Ag NPs (Figure 5.1). The noticeable difference

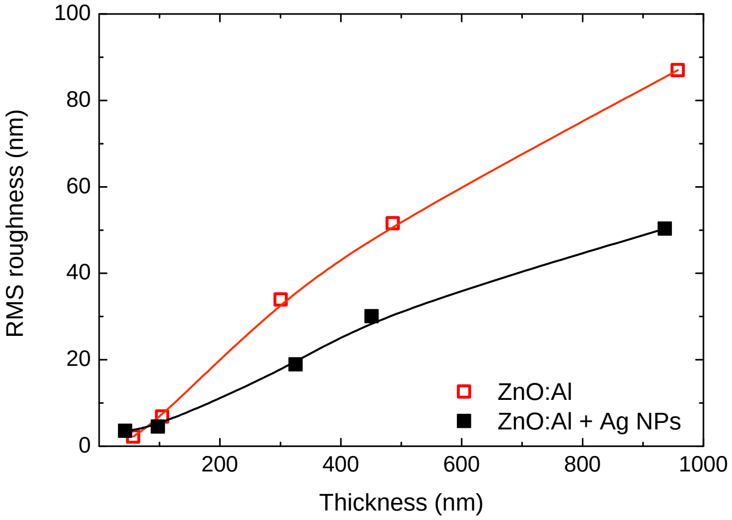

Figure 5.1. RMS roughness obtained from AFM measurements as a function of film thickness.

starts already for 100 nm – thick films (RMS(ZnO:Al)=7 nm, RMS(ZnO:Al+Ag NPs)=5 nm) and becomes progressively more significant. For ∼950 nm – thick ZnO:Al films the RMS roughness reaches 87 nm for the case without NPs and 50 nm for sample with Ag NPs.

The structural difference is also confirmed by the top-view High Angle Annular Dark Field Scanning TEM (HAADF STEM) results. In Figure 5.2 two 50 nm – thick ZnO:Al films are shown: Figure 5.2a displays films grown directly on carbon-coated TEM grid and Figure 5.2b shows the ZnO:Al developed on top of the Ag NPs on the TEM grid. Ag NPs of 3-5nm in diameter are visible as bright dots. It appears that ZnO:Al grown on top of Ag NPs exhibited smaller grains. For the ZnO:Al on TEM grid the grain size is 40-50 nm, while for ZnO:Al on Ag NPs/TEM grid the grains are about 20-30 nm large. Each individual ZnO:Al grain looks as developed on top of several adjacent NPs. Parallel electron diffraction (ED) studies of these two samples as well as from a sample only containing Ag NPs have shown a random orientation distribution for both ZnO:Al and Ag crystals. This demonstrates that at 50 nm film thickness there is no preferred orientation in Ag NPs and there is no clear development of a dominant orientation in ZnO:Al yet.

Furthermore, the development of ZnO grains was investigated in cross-sectional

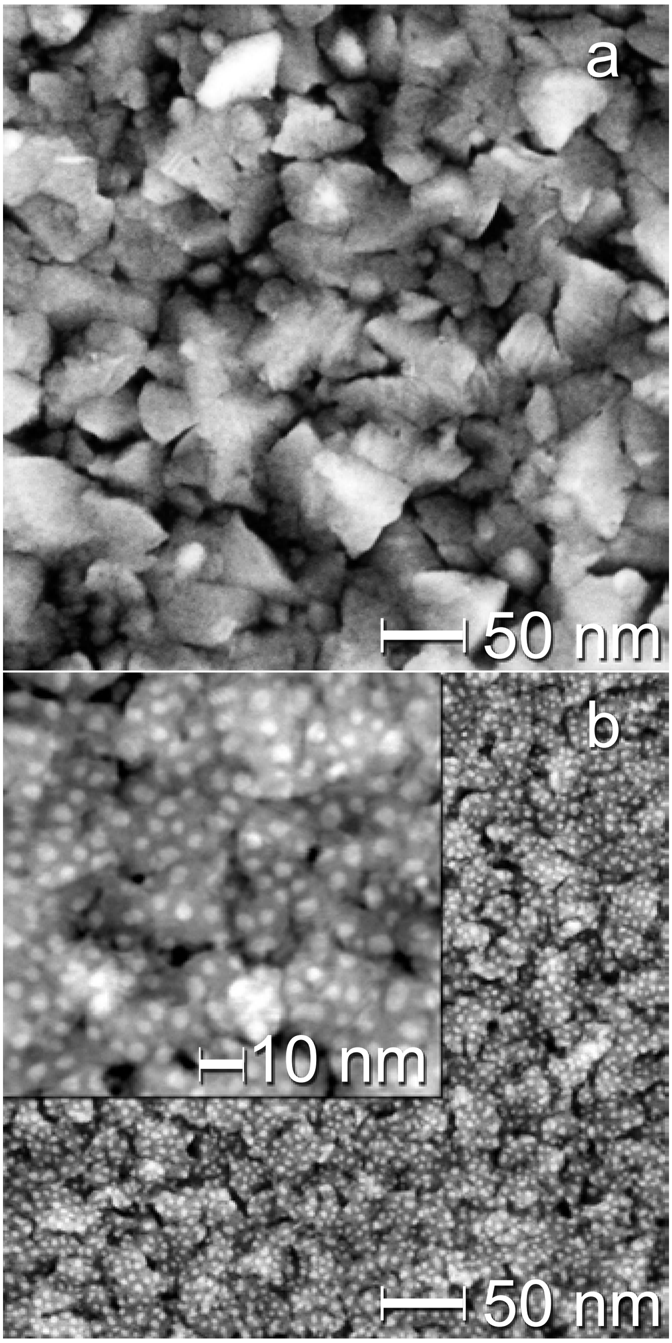

Figure 5.2. HAADF TEM images (magnification ×2.7·10^5 for both large images and ×1.1·10^6 for the inset in the right image), top – ZnO:Al on the TEM grid, bottom – ZnO:Al on Ag NPs deposited on TEM grid (visible as bright spots).

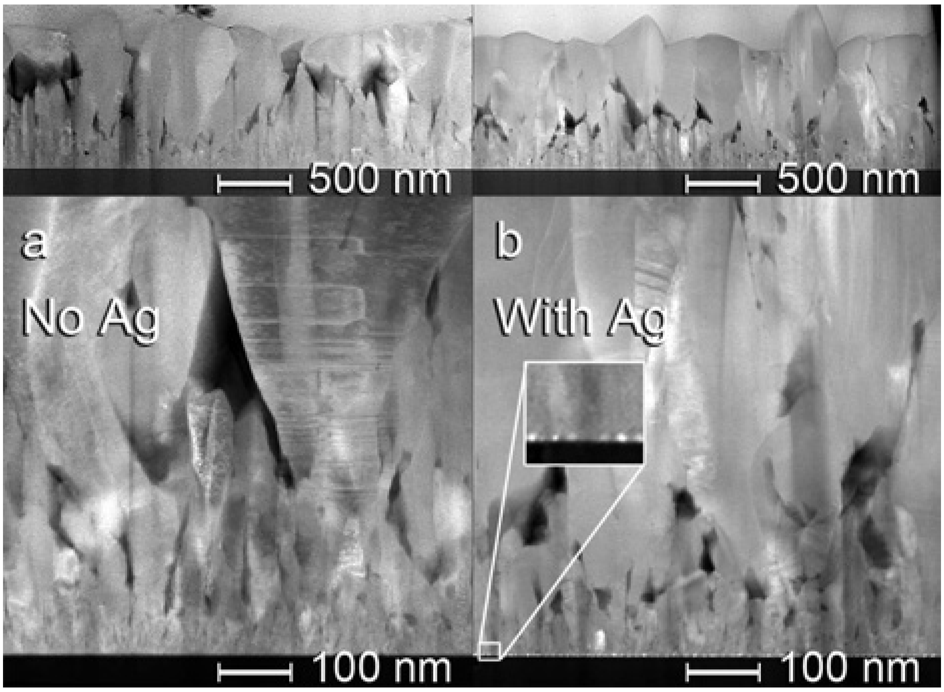

Figure 5.3. Cross-sectional HAADF TEM images left – ZnO:Al on bare glass, right – ZnO:Al on Ag NPs.

view and shown in HAADF STEM images in Figure 5.3. From this analysis based on 950 nm – thick ZnO:Al layers, it is observed that both films exhibit a so-called pyramid-like growth development, similarly to what earlier reported in literature [13], with a lateral grain size increasing with film thickness. The reference ZnO:Al grown without NPs exhibits voids starting from ∼100 nm up to about 600 nm film thickness (Figure 5.3a). With the further growth a dense structure develops. In contrast, the ZnO:Al deposited on Ag NPs is characterized by voids present in a limited thickness range of 100-400 nm and a compact, voids-free structure is developed further with larger film thickness. Thereby, the Ag NPs enabled a different growth mode causing formation of smaller crystallites at the nucleation stage (Figure 5.2), which developed into material with less pronounced voids and a more compact top layer. However, the difference in the final grain size of 950 nm – thick films is not as significant (Figure 5.3).

Additionally, the evidence of the different ZnO:Al growth development on top of NPs was also concluded from XRD measurements. While there was no difference observed from the 2Θ measurement of the 50 nm – thick layers, for

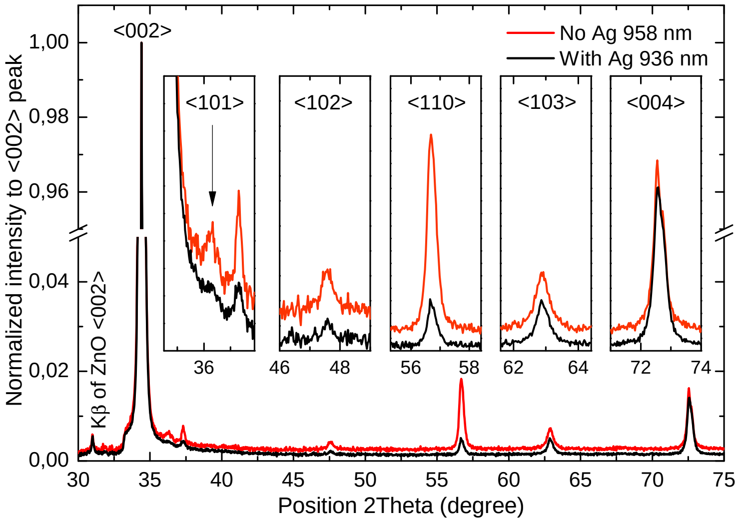

Figure 5.4. XRD signal intensities in 2Θ scan of ZnO:Al films. Suppression of several texture components with the addition of Ag nanoparticles at the same ZnO:Al film thickness.

the thicker ZnO:Al films the effect of Ag NPs was immediate. As it can be seen from Figure 5.4, the dominant XRD texture pattern is <002> (2Θ=34.4). Ag NPs suppressed the growth development of <101> (2Θ=36.3 degree) and <110> (2Θ=56.7 degree) orientations, while promoting the <002> orientation. The <110> orientation is perpendicular to <002> orientation and, thus, represents a limit to the <002> development. The XRD texture measurements of this <110> orientation (not shown here) confirmed the observation of significantly reduced <110> texture displayed in Figure 5.4. The texture measurement at <002> position demonstrated a narrower distribution along c-axis with the higher peak intensity for ZnO:Al on Ag: 2028 counts, compared to 1304 counts for ZnO:Al on glass at the same XRD measurement settings and a similar film thickness of 950 nm (Figure 5.5). For the case of <103> orientation (2Θ=62.8 degree) there was no difference in texture observed between the two conditions. The observations from XRD measurements imply that the Ag NPs promoted the growth of a more textured structure in the <002> direction.

The origin of the differences in the number of counts observed for <002> texture can be related to the presence of Ag NPs. It is known that there is a lattice match between ZnO <002> and Ag <111> [17, 18], likely promoting the epitaxial growth of ZnO <002> on the <111> surface of Ag. For example, ZnO nanorods

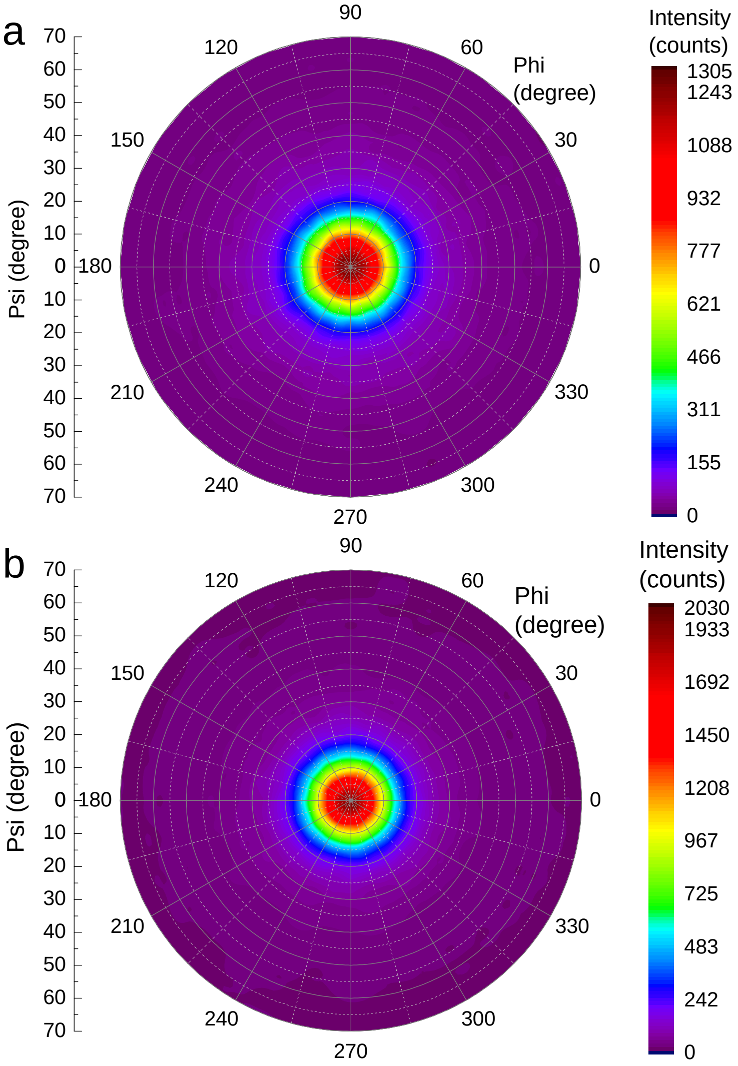

Figure 5.5. Texture measurement at <002> position for ZnO:Al of 950 nm thickness: a-reference ZnO:Al; b-ZnO:Al on Ag NPs.

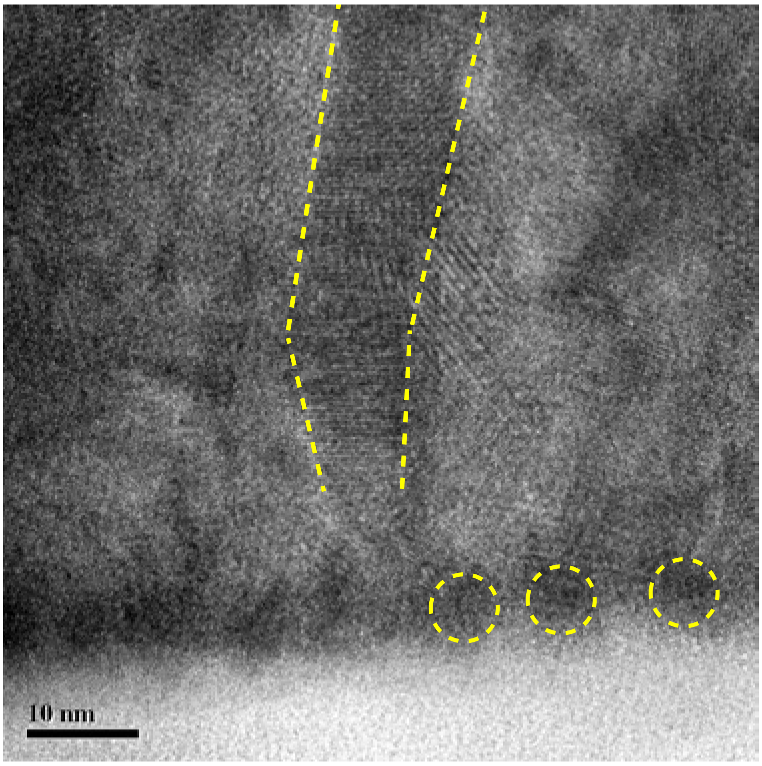

Figure 5.6. HAADF HRTEM image of ZnO:Al on deposited on Ag NPs, in the cross-sectional view. Grain with a lattice spacing ~5.2 Å is outlined by the two dashed lines and Ag NPs are outlined with circles.

can be grown in the <001> direction on the <111> facets of Ag NPs from aqueous solution [17]. Therefore, the array of Ag NPs on the surface can act as a series of nucleation sites for the early stages of ZnO growth. As mentioned above, electron diffraction studies of the layer of Ag NPs did not show a preferential orientation of the NPs. Thus, the enhancement of <002> texture in the ZnO:Al layer by the Ag NPs cannot be attributed to one single texture introduced by the Ag. Instead, the selective epitaxial growth of ZnO on Ag must be the cause for texture development in ZnO:Al. As epitaxial growth is only possible on <111> Ag facets, NPs having their <111> orientation in-plane will induce the lateral growth of ZnO:Al grains, while NPs having their <111> orientation out-of-plane will induce the vertical growth of ZnO:Al. The lateral development of ZnO:Al crystals has limited free space, up to the neighboring grains, causing rapid annihilation of their growth. The continuous film is created and the contribution of non-<002> vertical growth directions gets effectively reduced during further film growth.

This model is confirmed by high resolution TEM studies of the nucleation layer (one example is shown in the Figure 5.6): in the first 20 nm of the film thickness the number of ZnO:Al grains and lateral size are in the same order of magnitude as the Ag NPs, showing a strong reduction in the number of grains and increase in grain size directly above that layer (Figure 5.2 and Figure 5.3). In the first 20 nm of the film thickness lateral grain size is about the size of Ag NPs. Further increase in film thickness is characterized by the strong increase in the lateral grain dimensions and, therefore, reduced number of grains. As an example, cross-section of the film showing a grain with the lattice spacing corresponding to <002> orientation is demonstrated in Figure 5.6. In the case of the reference ZnO:Al, a clear onset of the grains in TEM cross-section images appears at larger thickness, ∼40 nm. This delayed nucleation caused smaller lateral grain dimensions, and so lower surface roughness, if compared to the same film thickness of ZnO:Al grown on Ag NPs, as shown in Figure 5.1.

5.3.2 Electrical properties

Similarly to the results previously reported for the same deposition method [13], a clear gradient in resistivity with the thickness of deposited ZnO:Al films is also observed for the sample series growth on Ag NPs, shown in Figure 5.7. The presence of the gradient is inevitably related to the structure: the grain size is increasing both vertically and laterally with increase in film thickness. Therefore, electron mobility is increasing, which enables reduction in resistivity for the thicker films. It is important to emphasize, that resistivity plotted in Figure 5.7 is an integrated value over the film thickness. Therefore, the resistivity of the top layer is influenced by the underlying more resistive layers and can be determined from the resistivity trend as a function of thickness. This approach has been demonstrated by Volintiru *et al.* [13], who determined the scaling factor for top resistivity from the slope of the linear fit in the double logarithmic plot of the measured resistivity and thickness. That gives resistivity of the top layer more than factor of 3 lower, as compared to the integrated value [13]. A similar to that value, scaling factor of 3.1±0.2, is obtained for the both curves in the Figure 5.7. So the top layer resistivity at, i.e., 950 nm for the ZnO:Al on Ag NPs is $3.4 \cdot 10^{-4}$ $\Omega \cdot$cm. Corrected resistivity values for both reference ZnO:Al and ZnO:Al on Ag NPs are also plotted in Figure 5.7 (open symbols).

It is important to note, that the effect of the Ag NPs present below the ZnO:Al

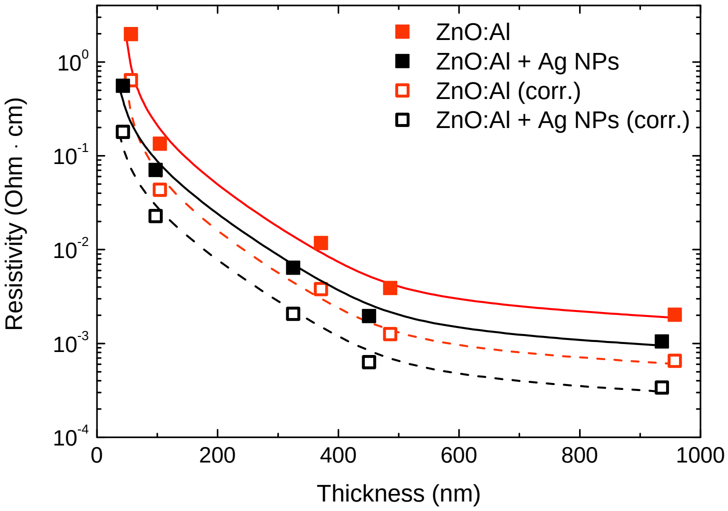

Figure 5.7. Dependence of ZnO:Al resistivity from thickness, with and without silver NPs present on the substrate.

layer resulted in a factor of 2 improvement in the electrical conductivity of ZnO:Al in the whole thickness range (Figure 5.7). This improvement could be explained by: i) the contribution of the metal NPs to the conductivity, acting as small electrical shunts; ii) the structural changes induced by the Ag NPs, which caused different growth of ZnO:Al crystals.

The first factor can be excluded, as here motivated. The reduction of the grain boundary surface with thickness leads to a reduced resistivity [13, 19]. Thus, the resistivity of ZnO:Al, measured in its lateral direction, decreases with increase in the film thickness, developing a gradient. If the Ag NPs would contribute to the measured conductivity, their influence would be the largest in the case of thin ZnO:Al layers, as these are more resistive. The metal NPs could act as electrical shunts within resistive media, thereby reducing resistivity for the current propagation in lateral direction [20]. Due to the gradient in resistivity with increase in film thickness, the effect of the electric shunts within the resistive media of the bottom layer, would be gradually less present, with an increase in thickness. However, the occurrence of the factor of 2 reduced resistivity is observed in the whole thickness range, up to 950 nm (Figure 5.7).

Another aspect suggesting the same conclusion is that if the NPs would act as shunts in the bottom layer, the scaling factor determined following the procedure of Volintiru *et al.* [13] would be lower than for the reference ZnO:Al series due to the different slope of resistivity in a double logarithmic plot. Thus, the possibility of Ag NPs contribution to the resistivity can be excluded and the effect of NPs on the resistivity is attributed only to the changes in ZnO:Al growth development. The thickness-dependent doping can be also excluded as responsible for the resistivity trend, because the carrier concentration measured for different thicknesses was $(3.5\pm0.7)\cdot10^{20}$ cm^{-3} for both sets of samples. In XPS depth profiles the Al relative content was found constant throughout the whole film thickness at the level of 0.7±0.2 at. % for both series, which supports the measured equal carrier concentration level, under the plausible hypothesis of the same doping efficiency.

However, charge carrier mobility was generally found higher for the samples with NPs. Mobility obtained from the optical measurement, similar to the earlier described by Volintiru *et al.* [19], reached 27±5 $\mathrm{cm}^2/\mathrm{V}\cdot\mathrm{s}$ for the sample on Ag NPs, in comparison with 13±3 $\mathrm{cm}^2/\mathrm{V}\cdot\mathrm{s}$ for reference ZnO:Al, both at 950 nm. Optical mobility in this thickness range corresponds closely to the Hall mobility, since the latter is less influenced by the gradient feature. This factor of 2 improved mobility in the ZnO:Al grown on NPs and constant carrier concentration together are in agreement with the reduced factor of 2 resistivity and the structural changes discussed earlier in the text. The pyramid-like grain development on NPs allowed for the onset of a compact layer by means of larger grains earlier developed when compared to the reference ZnO:Al series. If voids are suppressed, the transport path for the charge carriers is shorter and the associated losses are significantly reduced resulting in higher mobility values, provided a good passivation of the grain boundary surface. Since the scaling factor is the same (3.1±0.2) for the both reference and ZnO:Al on Ag NPs, it is concluded that the grain development is equal, but the improved resistivity can be attributed to the earlier nucleation of ZnO:Al grains on Ag NPs.

5.3.3 Optical properties

The optical properties of ZnO:Al grown on Ag NPs were also improved, even taking into account the absorption of light by NPs. As can be observed in Figure 5.8a, Ag NPs deposited on glass substrates exhibit an absorption peak at 450 nm, indicating plasmonic absorption [21, 22]. With increase in magnetron power, or, in other words, particle size and Ag surface fraction [16], the absorption peak increases and shifts towards higher wavelength. At the maximum power of 50

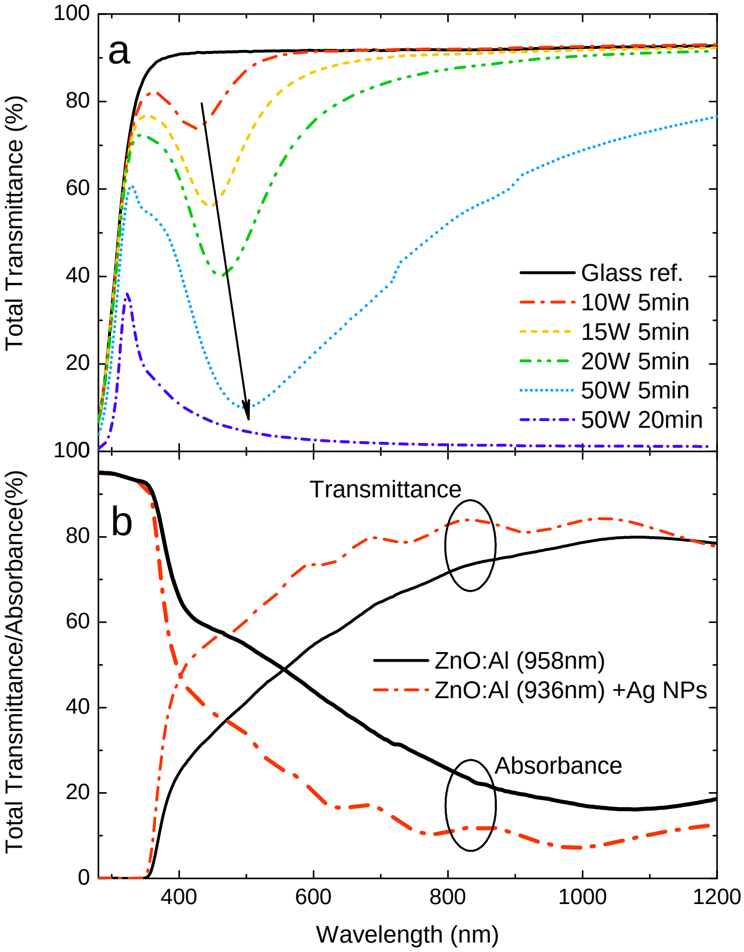

Figure 5.8. Total transmittance of: a – Ag NPs sputtered on glass at different magnetron power and time; b – thick ZnO:Al layers deposited on bare glass and on glass covered with Ag NPs.

W and sputtering time of 20 minutes there was a thick continuous Ag layer deposited, that absorbed most of the incident light (Figure 5.8a). A high absorption in the TCO window layer is an undesirable effect for solar cell applications and the absorption must be minimized to obtain high solar cell efficiency. Therefore, the deposition conditions for Ag NPs were chosen as 15 W for the magnetron power, as earlier reported in Table 5.1, and 5 minutes for sputtering time. At those conditions, as can be seen from the Figure 5.8a, the layer exhibited a transmittance equal to 75 % at the wavelength of $\sim$450 nm.

In Figure 5.8b the influence of Ag NPs on the total transmission of the 950 nm – thick ZnO:Al films is shown. Keeping in mind the light absorption by NPs at $\sim$450 nm wavelength, it is surprising that the total transmittance of the ZnO:Al film grown on Ag NPs is higher than the reference ZnO:Al deposited on bare glass, in the whole wavelength range from 350 to 1200 nm. This increased optical transmittance may be related to the reduced effect of light trapping within ZnO:Al layer due to reduced voids content, as observed by TEM measurements. The absorbance calculated from the measured transmittance and reflectance is lower in the case of Ag NPs. To summarize, the layer of Ag NPs on the substrate surface appeared to be acting as a template for ZnO:Al nucleation. It provided an early onset of the dominant <002> orientation and further growth into a layer with compact and large grains. At the same time, voids propagation throughout the film thickness was limited, compared to the reference films. These structural changes were reflected in a factor of 2 lower resistivity, independent of the film thickness, and in an improved optical transmittance.

5.4 Conclusions

Small, $\sim$3-5 nm in diameter, Ag NPs were employed to serve as an epitaxial template for improved nucleation of ZnO:Al grains, growth development and electrical properties. Due to the lattice matching between Ag <111> and ZnO:Al <002>, the contribution of this ZnO:Al texture component was significantly enhanced, while <101> and <110> components were reduced. Also, the onset of nucleation was observed at the lower thickness of $\sim$20 nm, as compared to the reference ZnO:Al at $\sim$40 nm. Therefore, the subsequent growth was substantially improved by Ag NPs, resulting in reduced voids inclusion throughout the film thickness and higher optical transmittance. Associated reduction of resistivity as a factor of 2 was observed in the whole thickness range and attributed to a factor of 2 improved electron mobility. Therefore, introduction of the Ag NPs on the substrate surface is a valid approach to improve nucleation, subsequent growth and electrical properties of ZnO:Al.

Acknowledgments The authors would like to thank Dr. H.T. Beyene for the fruitful discussions, R.H.J. Vervuurt and B.W.H. van de Loo for the help with samples preparation and analysis. M.J.F. van de Sande is gratefully acknowledged for the extensive technical assistance.

Bibliography

[1] S. Pearton, Progress in Materials Science **50**, 293 (2005).

[2] D. C. Look, B. Claflin, Y. I. Alivov, and S. J. Park, Physica Status Solidi (a) **201**, 2203 (2004).

[3] R. L. Hoffman, Journal of Applied Physics **95**, 5813 (2004).

[4] E. M. C. Fortunato, P. M. C. Barquinha, A. C. M. B. G. Pimentel, A. M. F. Goncalves, A. J. S. Marques, L. M. N. Pereira, and R. F. P. Martins, Advanced Materials **17**, 590 (2005).

[5] J. Muller, B. Rech, J. Springer, and M. Vanecek, Solar Energy **77**, 917 (2004).

[6] T. Minami, Semiconductor Science and Technology **20**, S35 (2005).

[7] U. Betz, M. Kharrazi Olsson, J. Marthy, M. Escolá, and F. Atamny, Surface and Coatings Technology **200**, 5751 (2006).

[8] V. Sittinger, F. Ruske, W. Werner, C. Jacobs, B. Szyszka, and D. J. Christie, Thin Solid Films **516**, 5847 (2008).

[9] H. Tanaka, K. Ihara, T. Miyata, H. Sato, and T. Minami, Journal of Vacuum Science & Technology A: Vacuum, Surfaces, and Films **22**, 1757 (2004).

[10] M. Ohyama, H. Kozuka, and T. Yoko, Journal of the American Ceramic Society **81**, 1622 (2005).

[11] C. Agashe, O. Kluth, G. Schöpe, H. Siekmann, J. Hüpkes, and B. Rech, Thin Solid Films **442**, 167 (2003).

[12] R. Groenen, J. Löffler, P. M. Sommeling, J. L. Linden, E. A. G. Hamers, R. E. I. Schropp, and M. C. M. van de Sanden, Thin Solid Films **392**, 226 (2001).

[13] I. Volintiru, M. Creatore, B. J. Kniknie, C. I. M. A. Spee, and M. C. M. van de Sanden, Journal of Applied Physics **102**, 043709 (2007).

[14] M. V. Ponomarev, M. A. Verheijen, W. Keuning, M. C. M. van de Sanden, and M. Creatore, Journal of Applied Physics **112**, 043708 (2012).

[15] M. C. M. van de Sanden, J. M. de Regt, and D. C. Schram, Physical Review E **47**, 2792 (1993).

[16] H. T. Beyene, F. D. Tichelaar, P. Peeters, I. Kolev, M. C. M. van de Sanden, and M. Creatore, Plasma Processes and Polymers **7**, 657 (2010).

[17] F.-R. Fan, Y. Ding, D.-Y. Liu, Z.-Q. Tian, and Z. L. Wang, Journal of the American Chemical Society **131**, 12036 (2009).

[18] J. Floro, J. Michael, L. Brewer, and J. Hsu, Journal of Materials Research **25**, 1352 (2011).

[19] I. Volintiru, M. Creatore, and M. C. M. van de Sanden, Journal of Applied Physics **103**, 033704 (2008).

[20] H. Han, N. D. Theodore, and T. L. Alford, Journal of Applied Physics **103**, 013708 (2008).

[21] D. D. Evanoff and G. Chumanov, Chemphyschem : A European Journal of Chemical Physics and Physical Chemistry **6**, 1221 (2005).

[22] M. Schmid, R. Klenk, M. C. Lux-Steiner, M. Topic, and J. Krc, Nanotechnology **22**, 025204 (2011).

Summary

Aluminum-doped Zinc Oxide (ZnO:Al) is a polycrystalline semiconductor material, widely used in optoelectronic applications. Due to the wide band gap (3.4 eV) and high electrical conductivity, ZnO:Al combines a high optical transparency in the visible region with an efficient transport of electric charges. These represent valid motivations, besides non-toxicity, to apply ZnO:Al as transparent conductive layer in the rapidly developing sustainable applications, such as thin film solar cells. The commercial feasibility of the application renders mandatory the achievement of a minimum in electrical resistivity with high optical transmittance at low production costs, i.e. thin, conductive ZnO:Al layers.

Nowadays, magnetron sputtering is one of the most commonly used deposition techniques. However, the low deposition rate hampers the wide industrialization of this technique for commercial production. Moreover, a characteristic columnar growth and a limited development in the lateral dimensions of ZnO:Al grains with increase in film thickness force to deposit thicker layers (> 1 µm) to achieve a large lateral grain size and a low film resistivity.

In this work, the Expanding Thermal Plasma (ETP) deposition technique was employed to study the growth development of ZnO:Al films. The ETP has the potential for high deposition rates, as already shown in the case of amorphous silicon films. Characteristic for ETP-grown ZnO:Al is a gradually reducing resistivity of the growing layer, so-called resistivity gradient, due to the increasing grain size and mobility of the electrons. The X-Ray diffraction study at different stages of ZnO:Al growth revealed a random nucleation, proceeded by a competitive growth of various crystallographic orientations, which finally evolve in the dominant <002> orientation. That random nucleation and competitive growth are the results of negligible ion bombardment during ETP growth of ZnO:Al. Small grains develop at low film thickness and are, therefore, characterized by charge carrier trapping phenomena occurring at the grain boundaries. As the grain further develops in lateral size as function of the film thickness, the scattering at the grain boundaries becomes progressively less dominant with respect to other mechanisms (e.g. scattering at ionized impurities) and lower resistivity values are only achieved for large film thickness.

If the grain boundary trapping centers are passivated, electrical performance

of the ZnO:Al can be dramatically improved. That has been achieved by capping the ZnO:Al films with hydrogen-rich amorphous silicon (a-Si:H) layers followed by a high temperature treatment. This process mimics the experimental procedure of crystallization of a-Si:H to poly-Si layers during the manufacturing of poly-Si based solar cells. With the support of Time-of-Flight Secondary Ion Mass Spectrometry it is shown that, upon thermal treatment, the hydrogen present in the capping layer diffuses towards ZnO:Al, passivating its grain boundaries. Thus, the resistivity of the grain boundary-rich areas is strongly reduced (by a factor 45 for 130 nm-thick layers), eliminating the resistivity gradient of the as-deposited films.

Another approach for reduction of the resistivity gradient is to modify the growth of ZnO:Al crystals. This was achieved by exploring experimental conditions leading to a compact nucleation layer with a large grain size and multiple crystal orientations. This resulted in a significantly reduced resistivity gradient down to ∼300 nm thickness. Moreover, the resistivity achieved at this thickness, was equal to $3.9 \cdot 10^{-4}$ Ω·cm obtained for 700 nm-thick reference film, in the presence of the gradient. However, further growth is characterized by the competitive development of only two crystal orientations, <002> and <103>, and formation of large voids between grains, as shown by Transmission Electron Microscopy. In comparison, voids are already present from the nucleation stage of the films characterized by the gradient. The distribution of voids throughout the film thickness appears to be a key parameter in controlling the electrical properties of the bulk layer: a void-rich initial phase is responsible for the gradient in resistivity, but if developed at the later stage (>300 nm), it hinders the gradient formation. The control on the growth development in terms of selection specific crystal orientations in the early phases of growth appears fundamental in determining electrical properties of the CVD ZnO:Al. It is also closely related to understanding of the processes in the depositing plasma, and the question arise: "what mechanisms drive the growth of ZnO:Al?"

To address this question Mass-Spectrometry was employed to provide an insight in the investigation of the plasma processes accompanying the growth of the high quality ZnO:Al films, both with and without resistivity gradient. Under the experimental conditions leading to a massive decrease in the resistivity gradient, a significantly reduced growth flux was measured, accompanied by the substantial production of hydrocarbon species observed during the deposition process. The abundance of the zinc precursor, i.e. the diethylzinc-to-O_2 flow rate ratio, has been identified as responsible for the gradient in resistivity. In particular, the chemistry channels developed in the proximity of the substrate surface are investigated and correlated with structural and electrical characteristics of the deposited ZnO:Al films. It is found that the diethylizinc-to-O_2 ratio allows tuning the atomic oxygen flux availability at the surface of the growing film, which affects nucleation of the ZnO:Al layers, the development of specific crystal orientations, grain size and, eventually, electrical properties.

A modified nucleation stage of the ZnO:Al grains can also be achieved without changing the deposition conditions, but affecting the substrate conditions, which appears to have a noticeable impact on the development of the structure and the final resistivity of the deposited film. Dedicated experiments show that small (3-5 nm in diameter) silver nanoparticles deposited prior ZnO:Al growth can affect the ZnO:Al growth. Since the lattice parameters of the silver <111> orientation match with the <002> in ZnO, which is the main crystal orientation in the deposited ZnO:Al films, an earlier onset of <002> orientation observed. The silver NPs act as an epitaxial template, also causing reduction of void inclusion throughout the film thickness. Although the gradient in resistivity is still present, the overall resistivity reduced of a factor of 2 in the whole thickness range up to 1000 nm, mainly due to the improved electron mobility and was accompanied by increased transmittance of the ZnO:Al layer.

Acknowledgments

Importance of this section for me is as high as of the other chapters in this thesis. I wish to thank all those who helped me throughout the long journey of completion my PhD dissertation. Without their support I could not have succeeded to do all experimental work, analysis and writhing for this thesis. I gratefully acknowledge each of them, no matter how large was the grain size of their contribution.

I'd like to give special thanks to my supervisor, prof. **Richard van de Sanden**, whose enthusiasm and talent to give impetus to strive for new highs were so valuable, especially in the moments of frustration. I would also like to thank my daily supervisor dr. **Adriana Creatore**, for the great support and the time spent discussing results and correcting my writing over and over, up to the perfect level. I thank prof. **Erwin Kessels** for providing me opportunity to complete this thesis.

I am very much obliged to the very special person – our PMP technician **Ries van de Sande**, for both technical and emotional support. Thank you, Ries, for all the effort, all the time dedicated and willingness to keep my experimental setup ZOPHIA in the good working state, despite of all kinds of failures it had. Without you it would be impossible for me to arrive to this thesis. Thank you for the great sense of humor and songs that kept my work spirit high.

Since the setup was an extremely good source of all kind of troubles, it often required technical expertise and knowledge of several people. In that regard, I would like to thank **Janneke** for being always of a great help no matter how big were the problems and also for providing a welcoming atmosphere in the office. In addition, I acknowledge the technical skills of **Joris** and the expertise of **Herman** in supporting me. It is also worth mentioning **Gerbert Fiedler**, who was solving all kinds of electronics-related and software issues and **Frans Aarts**, area sales manager at Bronkhorst Nederland B.V., for providing good customer support of CEM systems.

Thanks to my project colleagues prof. **Miro Zeman** and dr. **Arno Smets** from Delft University of Technology for sharing knowledge, fruitful discussions and being hospitable hosts every time I visited them.

Next, I give my special thanks to the two people with whom I worked "shoulder to shoulder" in analyzing my ZnO:Al samples and the outcome of the measure-

ments. **Wytze**, thank you for the countless XRD measurements you've done for me, explanations and answers. It was a lucky coincidence to have **Marcel** started at our PMP group as a TEM expert and I truly appreciate all his effort in performing really important measurements, providing crystallography lessons and discussions that lead to development of most of the chapters in this book. Wytze and Marcel, besides of all the work you've carried out, it was personally a pleasure to work with you, thank you. My big acknowledgement is addressed to Haile for all the work we have done on metal nanoparticles and it is a pity that it is not present in this thesis.

Throughout the years of my PhD there were several people who were sharing office with me for a year or two and then leaving. But, there was one person, who was always there, that is my dear roomie and a good buddy. **Aafke**, I thank you for all the support during those years, for the great help with work-related issues, for translations of my mails from Dutch into English, for facilitating my integration and understanding of the Dutch culture. I wish to thank for the nice office atmosphere my other officemates: **Paul**, also being example of good in-depth researcher; always overloaded with work **Magda**, shy and quiet **Anu** and very friendly **Ming**.

I thank all my PMP colleagues who helped me to overcome cultural shock and home sickness at the beginning. To start with, my first roommate **Kashish**, who arrived to The Netherlands at the same time and was experiencing the same thing. The only chance to talk in my native language, inexhaustible source of wisdom was **Sergei**, who still remains a good friend. I acknowledge my neighbors and colleagues **Teodor** and **Jie** for the great time in Boxtel and especially for the basketball games. I thank **Pavel** for practicing Russian with me, **Cristina** for always being nice and kind, **Gianfranco** for his sense of humor and **Nick** for the useful tips and orientation within Eindhoven.

I wish to thank our ellipsometry guru **Jan-Willem** for all the time and effort dedicated to my difficult ZnO:Al samples and also for the friendly company. I thank **Harm** for the help with the ellipsometry, writing and for the fruitful discussions; **Terje** for introducing me to the worlds of Apple and astronomy; **Erik** for establishing nice social traditions and regulations at PMP. I also acknowledge **Noemi** for being friendly and cheerful in the good times, caring and supportive in the bad times. My thanks to **Anitha** and **Antony** for demonstrating Indian culture and hospitality, to **Stephan** for the German ones and also for the healthy competition in photography. Of course, together with the people I already mentioned, I cannot forget contribution of **Jan-Pieter**, **Stephen**, **Diana**, **Tatiana** and **Adrie** for taking care of "PMP spirit" and its level in time.

I wish to thank my AFM fellows **Vincent** and **Bart** for the effort to understand the operation of the instrument and making the user manual to provide gained knowledge to the broad audience of new AFM users.

Thanks to **Rein Rumphorst** for the Dutch lessons and jokes every morning, dr. **Richard Engeln** for keeping his finger on the pulse of PMP spirit and **Bernadette** for kindness and for starting tradition of Christmas punch. I gratefully acknowledge PMP group secretaries, **Lianne** and **Jeanne**, for all the help with the paperwork during my PhD time.

There was a number of people at TNO who I wish to thank: **Paul** who started to work with me on ZOPHIA setup and has always been willing to help in all kinds of issues; **Andrea** for trying to snoop results of my measurements; **Frank** for the help with precursors and CEM systems in the lab; **Joop** for managing administration questions. Also, thanks to prof. **Fred Roozeboom** who helped me a lot in orientation and search for a new job.

I thank my students: **Robin**, **Tim**, **Huajun (Jim)**, **Sander**, **Rene** and **Bas**, for the fun time together and for challenging my supervisor skills. The work we did together evolved eventually into the chapters of this thesis. In this respect I specially thank Robin and Tim for making mistake during experiment, which enabled me to create "closed vessels series" and served as a good base for the thesis.

Thanks to **Russian-speaking community** in Eindhoven for the nice time together and for supporting me and my family. I thank my **mother** and **grandmother** for the opportunity to make first steps on the way that brought me to this book. This thesis could not be completed without absolutely invaluable contribution of my wife **Anna**, who was constantly supporting me up to the very end and giving all the help she could to make it happen, also by designing the cover of this book.

Mikhail V. Ponomarev

Eindhoven, October 2012.

Curriculum vitae

Personalia

Family name	Ponomarev
First name	Mikhail Victorovich
Date of birth	15 May 1983
Place of birth	Shumikha, Kurganskaya oblast, USSR

Education and Work experience

1991 - 1999	Comprehensive School #4, Shumikha, Kurganskaya oblast, Russia
1999 - 2000	Specialized Scientific-Educational Center of Novosibirsk State University, Novosibirsk, Russia.
2000 - 2004	Bachelor of Science Degree in Physics. Bachelor project between Physics Faculty of Novosibirsk State University and Laboratory of Molecular Kinetics, Institute of Thermophysics SB RAS, Novosibirsk, Russia.
2004-2006	Master of Science Degree in Physics. Master thesis project between Physics Faculty of Novosibirsk State University and Laboratory of Molecular Kinetics, Institute of Thermophysics SB RAS, Novosibirsk, Russia.
2006-2007	Research assistant at Laboratory of Molecular Kinetics, Institute of Thermophysics SB RAS, Novosibirsk, Russia.
	External traineeship in the group "Plasma & Materials Processing", Department of Applied Physics, Eindhoven University of Technology, Eindhoven, The Netherlands.
2007 - 2012	PhD student in the group "Plasma & Materials Processing", Department of Applied Physics, Eindhoven University of Technology, Eindhoven, The Netherlands.
2012-present	Technical Support Engineer TSG NPI, FEI Company